Production of Strange Particles in Ultra-Relativistic Proton-Tungsten Collisions at 200 GeV/c

J. Paul Davies

Thesis submitted for the degree of
Doctor of Philosophy

School of Physics and Space Research,
Faculty of Science,
University of Birmingham.

November 1995.

Synopsis

The production of strangeness is a vital tool in the study of hot, dense hadronic matter. Indeed, the primary aim of the WA85 experiment is the study of strange and multistrange baryon and anti-baryon production, which are expected to be enhanced if an exotic state known as the Quark Gluon Plasma is formed in heavy ion collisions.

The WA85 experiment collided sulphur ions and protons on a tungsten target at 200 GeV/c per nucleon. Particles were detected in the kinematic window of central rapidity and $p_T \geq 0.6$ GeV/c. The results in this thesis are based on the data recorded during the 1990 proton-tungsten run. This run was used as a control in the sense that the conditions formed will not provide a suitable environment for the formation of the plasma phase of matter.

The relative production yields and transverse mass spectra for Λ, $\overline{\Lambda}$, $\Xi^-$and $\overline{\Xi^-}$ decays are presented and compared with the results obtained from the 1990 sulphur-tungsten run. The particle to anti-particle ratios are compatible when comparing the proton-tungsten to the sulphur-tungsten data. However, there is an increase in the ratio of multi(anti)strange to (anti)strange baryons of about 30% when going from proton-tungsten to sulphur-tungsten interactions. The difference in these ratios corresponds to about a two standard deviation effect. The inverse slopes obtained from the transverse mass distributions from the proton-tungsten data lie in the range of 200 MeV to 210 MeV, lower than those found in the sulphur-tungsten data which are compatible with 230 MeV.

The production of negative particles has also been studied, and if interpreted as π^-s, yield an inverse slope of 196 MeV $\pm$ 2 MeV, when plotted over the entire range of transverse mass. The results show that there is an increase in the inverse slope above an m_T of about 1.5 GeV/c.

Acknowledgements

I should like to thank Professors George Morrison and John Dowell for giving me the opportunity to undertake a Ph.D. in the School of Physics and Space Research at Birmingham University. I would like to appreciate the financial support given to me by PPARC and hope that it went at the expense of weapon research.

I would like to thank my tutor, Professor John Kinson, for his help during my Ph.D. and for writing references, amongst other things. Thanks also must be extended to Drs Orlando Villalobos Baille [1] (again for references) and David Evans, whom with Professor John Kinson, read the many, rather chaotic, versions of my thesis and discovered quite what a fool I am. Generally I would like to thank the above three 'Omegas' for their collective attempts to help me remain sane when staying at CERN. Although through politics and general thought I am instructed to 'hate' Dr David Evans, in my heart I cannot do so! I would also like to thank Roman Lietava for his help in explaining many rather obscure ideas to me and probably the third most amazing man in the world 'Dr Frank Votruba' for being so *individual*. Cheers to Dr N. Carney for being an all round 'crazy guy' and particularly for giving myself and K. Norman stomach muscle strain on a day in the summer of 1994 that I shall never forget. In addition, for help with computing problems and general questions which may well have persuaded some madman to give me a

[1] also cheers for allowing me to barge ino your office, seemingly on any occasion.

job, thanks to Dr. Laurie Lowe. Thank you also to Alan Watson for terribly enjoyable maths tutorials (they're better students now i'm sure!).

Now to the fun part....

I would like to appreciate everyone I have met through particle physics ..... and in a way I have. Firstly, I must thank Andy Bayes for generally putting up with my slow wit and temper for far too long (about 12 years), I hope the thing with Sharon stays cool [2]. Also hello to all those people in his year of study.... Jim Clayton for being a true drinker (not that I approve in any fashion), Stephen Clewer for all the hatred the world ever needed, Stuart Robertson - you beat me by a long way, but at least I got some time off before starting the BEAST thing! Ok chronological order continues (kindof) - thanks to the 'Master' (the DOD) for being who he is and hopefully continuing in such a vein, age permitting - never before have I met such a monster of incredibleness! Also thanks to Richard Barnes who I only knew a bit, but seemed damn fine. The year of true frivolous behaviour certainly seemed to come from those foolish present 3^{rd} years - Vicky '*not allowed to say it*' Hudgson, Dave 'man the riggers' Rigby for many undescribable acts which to many humans would render them crippled (he's a romantic at heart .. say hi to M.J.), Keith 'slippers' Norman [3] ... a man of consummate passion for the ways of middle age (only joking ... sorry) again you kept me sane, and Tim 'the Nicholls' Nicholls - stay WELSH and chunky. A special word must be given to Neil - man of chemicals - Talbot for being most definitely who he is - you were a good club partner for a year or so and I can't think of a much better praise! Cheers to Mark 'Mickey' Pearce for all the PAW tips and those eyebrows, and my present house mates (the smokey brothers - Paul Newman and Chris Nolan - love you both) for clogging my lungs and keeping me up far to late! Thanks to Ian Brawn - keep the hair green. To

[2] don't worry I won't be following you up to Madchester.

[3] don't you dare do anything naughty in that jug I bought you.

the second years, thanks to James Bloomer for metal riffs and letting me stay that week at CERN, Mark (the future of the ions) Venables, Andrew 'Beinvenue' Bellend (how's the groin), Kirsty Hewlitt (+ Mike) - I won't forget that night at Crunch in a hurry, and Steve Oglesby, the man who changes personality at the sight of alcohol. Thanks to the new Omega first year Bryan ... who already seems to fit the bill in the traditions of Omega students [4].

Thank to all those i've met at CERN and related places *plus* I actually liked .... Dave Kant, James King, Warren Mathews, Ollie Cook, Rob Akers Jim 'Rude' Edwards, Stuart Clowes and Clive Lewis, to mention but a few. Also Tanwir Ahmed for pretending to be violent and Dave Rees for looking sharp. Thank you very much to Alison Wright for letting me doss the night before the Interview! Much thanks to Lee West and presumably Rachael West too ... eat on!

Thank you to my old household (the prammers - sorry Guy and Lisa) and related Moseley types you helped me grow young again (uurrgg) .... I hope Cassey Cassum has you in his prayers. A special gratitude to Rosie for loving like a good woman can. Cheers to a man I don't think i'll ever see again Irish D., you were a true inspiration and I mean that without any sicklyness! Top applause for my very good friends Dave Lidzey and Bex .... you were always a bit weird, but I loved you loads.

Cheers to those lot I met in San Fransisco after the Monterey Conference .... you broke me free from Physics for a bit.

Thank you very much to my mum and dad .... you really are excellent 'modern type' parents.

Probably [5] the biggest thanks goes to Rebecca Jones (lump in throat time) she performed the needy task of filling me with lust and being there all the

[4] not that I appreciate traditions in any shape or form.

[5] i'll never hear the end of this.

time - I love you *rudely*.

I'll miss you all!

And finally thanks to ME for being clever enough to finish this thing as quickly as poss!

J. Paul Davies, 6th November 1995, Birmingham.

'It is a foul and dreich night. Filthy clouds hang ovehead; waiting to spew their dark load on the shuffling citizens below, for the umpteenth time since the break of dawn. The bus station concourse is like a Social Security office turned inside out and doused with oil. A lot of young people living on big dreams and small bugets stand somberly in line at the London rank. The only cheaper way down is by thumb.'

- Irvine Welsh, *Trainspotting*, 1993.

'The contradiction so puzzling to the ordinary way of thinking comes from the fact that we have to use language to communicate our inner experience which in its very nature transends linguistics.'

D. T. Suzuki.

'The problems of language here are really serious. We wish to speak in some way about the structure of atoms .... But we cannot speak about atoms in ordinary language.'

W. Heisenberg.

Contents

List of Figures

List of Tables

Chapter 1

The Quark Gluon Plasma and Heavy Ion Physics

1.1 Introduction

During the last decade an extensive program has been undertaken whose aim is the study of matter under extreme conditions of temperature and density, reflecting those realised about 10^{-5} seconds after the Big Bang [1]. The most exciting prospect of such a challenge is the possible observation of a transition from normal hadronic matter to an exotic state known as the *Quark Gluon Plasma* (QGP) [2, 3, 4].

Two of the world's high energy accelerators, the SPS and AGS, situated in the laboratories of CERN and BNL respectively, are now able to generate ultra-relativistic heavy ion beams. This development in the utilization of these accelerators has provided the opportunity to study the dynamics of hot, hadronic matter. CERN has accelerated oxygen, sulphur and most recently the truly heavy ion of lead, with BNL concentrating on silicon and, in 1993, gold. A maximum beam energy of 200 GeV per nucleon has been obtained at CERN.

In this chapter the following questions will be addressed :

- *What is a Quark Gluon Plasma*?
- *How is it formed in the laboratory*?
  and
- *How is it possible to probe for the existence of a QGP and study its properties*?

The motivation for such a search stems from the prediction of the QGP by Quantum Chromodynamics (QCD) [5], and as such it forms a vital test of this fundamental theory of strong interactions. To this end a brief overview of QCD is now presented.

1.2 The Quark Gluon Plasma Phase

1.2.1 Quarks and Colour

The theory of QCD attempts to describe quantitatively the interquark(gluon) forces which bind hadronic matter. There are three types of colour (strong) charge which, in the convention of QCD, are called red(R), green(G) and blue(B). These form the basis of the 'colour' multiplet of SU(3). 'Colour' is just a name for an internal degree of freedom and is analogous to the more familiar electric charge, of which there is just one type. Any object which interacts through the strong force is composed of 'coloured' partons. In addition to colour, quarks exist in a variety of just six flavours, another internal quantum number, which when combined with the spin of the quark contributes towards the total wavefunction of the hadron of which it is a member. Table 1.1 [1] illustrates the different flavours and masses of the

[1] the observation at Fermilab of the top quark corresponds to a 4.8σ effect [6]. If interpreted as the top the mass given is found.

Table 1.1: Quark Characteristics.

Quark Flavour	Q/| e |	Bound (dynamical) Quark Mass	Partially Chirally Restored (current) Quark Mass
u="up"	$+\frac{2}{3}$	$m_u \sim m_d \sim 350$ MeV/c^2	$m_u \sim m_d \sim 6$ MeV/c^2
d="down"	$-\frac{1}{3}$		
s="strange"	$-\frac{1}{3}$	$m_s \sim 550$ MeV/c^2	$m_s \sim 150$ MeV/c^2
c="charmed"	$+\frac{2}{3}$	$m_c \sim 1.8$ GeV/c^2	$m_c \sim 1.4$ GeV/c^2
b="bottom"	$-\frac{1}{3}$	$m_b \sim 5.3$ GeV/c^2	$m_b \sim 4.8$ GeV/c^2
t="top"	$+\frac{2}{3}$	Not Observed	$m_t \sim 174$ GeV/c^2

quarks.

The standard quark model defines hadrons in two forms - baryonic and mesonic. All combinations of quarks and antiquarks other than the following are excluded

$$\mathrm{qqq}, \overline{\mathrm{qqq}} - \text{baryonic matter}$$

$$\mathrm{q\overline{q}} - \text{mesonic matter}$$

where q and $\overline{\mathrm{q}}$ represent the quark and antiquark partons. Baryons are characterized by half integral spin ($\frac{1}{2}\hbar, \frac{3}{2}\hbar$), which means that they are classified as a type of particle called a fermion which has an overall antisymmetric wavefunction. Baryons and mesons lie in groups or multiplets. These are defined by the internal properties of the hadron which arises from the manner in which the quark content arranges itself. For example, the proton (uud) and neutron (ddu) form a two fold multiplet defined by their flavour. The u and d quarks are very similar in mass and are seen as substates of the 'same' particle. They are only distinguished by the difference in their interaction

with the electromagnetic force, a result of their different electric charges. The concept of isospin space was introduced to formalize the difference between the proton and neutron [7]. A direction in isospin space defines the charge of the particle and a transformation in isospin space can change a proton into a neutron (and vice versa).

The system is invariant to such a transformation as far as the strong force is concerned *i.e.* the total isospin is conserved; this is an example of a symmetry. Approximate higher symmetries were discovered in the 1960's, which led to the formation of various multiplets. These were later interpreted in terms of the quark model. The baryon decuplet is shown in figure 1.1. The members of the isospin multiplets differ in mass by only a few MeV, but the mass difference for each increment of strangeness is roughly the same. This pattern led to the prediction of the Ω^-, discovered in 1964 [8]. The requirement that baryons, such as the Ω^- which contain three quarks of the same flavour and all aligned with the same spin, has an overall antisymmetric wavefunction, was solved by the introduction of colour. A transformation in colour space will change the polarity of the wavefunction, so now the form of the wavefunction is antisymmetric.

1.2.2 QCD and Deconfinement

Coloured objects - quarks and gluons [2] - are not observed as physical states according to the standard quark model. This is known as confinement, probably the most striking feature of QCD. Only 'white' objects with no net colour are observed in nature, for example the combination RGB forms the colourless state of a baryon or $B\overline{B}$ for a meson. This is a fundamental difference between QCD and QED, a reflection of the non-abelian nature of the Lagrangian which defines the strong interaction. A colourless 'bag' of

[2] the gluon is the mediator of the strong force analogous to the photon in QED.

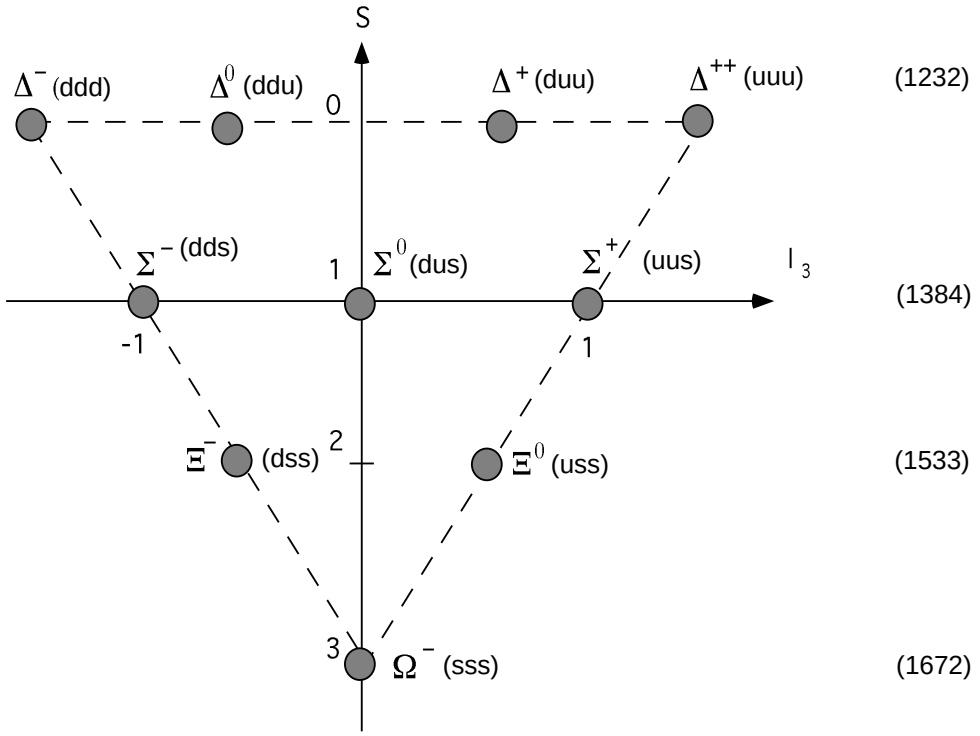

Figure 1.1: The observed baryon decuplet of states with spin-parity $\frac{3^+}{2}$. The mean mass of each isospin multiplet in MeV/c^2 is given in brackets.

isolated quarks is formed by the QCD vacuum expelling the colour field of the partons placed in it. However, when two quarks are pulled apart the lines of colour force are squeezed into a flux tube known as a string, illustrated in figure 1.2 [9]. The energy within these strings grows linearly with its length; the colour potential has the form [9]

$$V_s \sim -\frac{\alpha_s}{\mathrm{r}} + \sigma \mathrm{r} \tag{1.1}$$

where α_s is the strong coupling constant, σ the string tension and r the distance between quark and anti-quark. The linear term which dominates at the order of 1 fm implies an infinite amount of energy is required to free a single quark. At small distances between the two quarks the first term defines the potential and single gluonic exchanges dominate. The strong coupling constant α_s tends to zero as r approaches zero is such a manner so as to reduce the potential with decreasing distance.

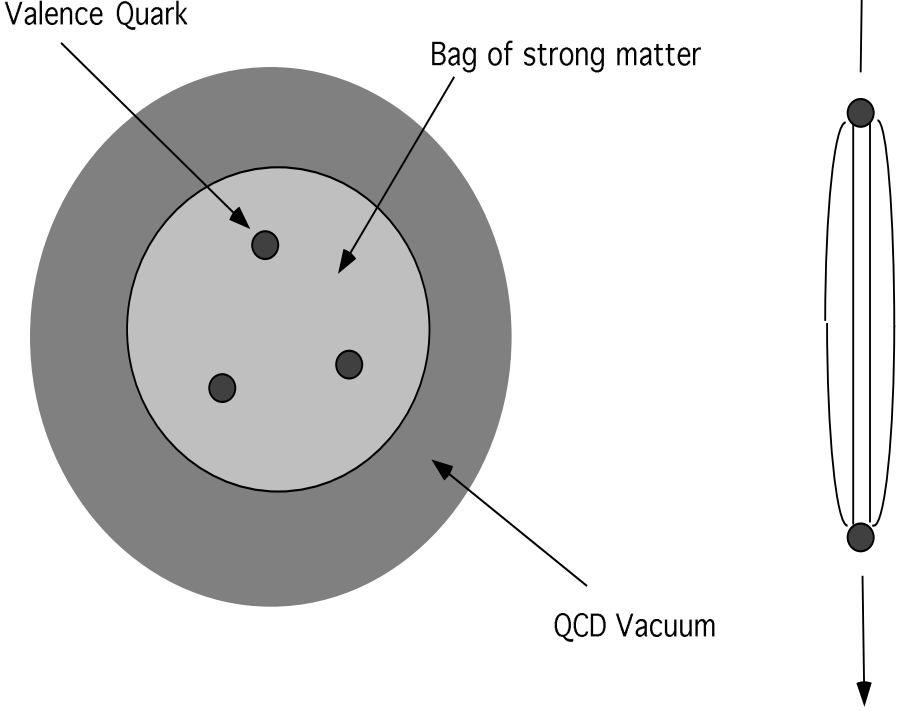

Figure 1.2: (a) A bag formed by the QCD vacuum expelling the colour field; and (b) lines of colour force between a separating quark - antiquark pair.

Running Coupling Constant and Asymptotic Freedom :

In quantum field theory partons are not seen as individual pointlike objects, but surrounded by a cloud of continually emitted and absorbed coupled partons. For example, in the QED scheme an electron will emit and absorb photons which can decay to electron-positron pairs. The arrangement of these pairs of opposite charge will hide the 'bare' charge of the electron and lead to the concept of a running coupling constant. Indeed α_{em}, the electromagnetic coupling constant is dependent upon the momentum transfer in the interaction of the electron with a probe, see figure 1.3 (a). A similar process occurs in QCD, but unlike the photon the gluon carries the charge of the force it mediates, colour, and can couple to itself resulting in multigluonic couplings. This is illustrated in figure 1.3 (b), where a quark emits gluons which can either decay to quark-antiquark pairs or form gluon loops. The effect is to anti-screen the 'bare' quark *i.e.* the colour charge spreads out so that a colour probe will measure a higher effective colour. Only in the case where the probe and quark form a hard interaction so that the probe is able

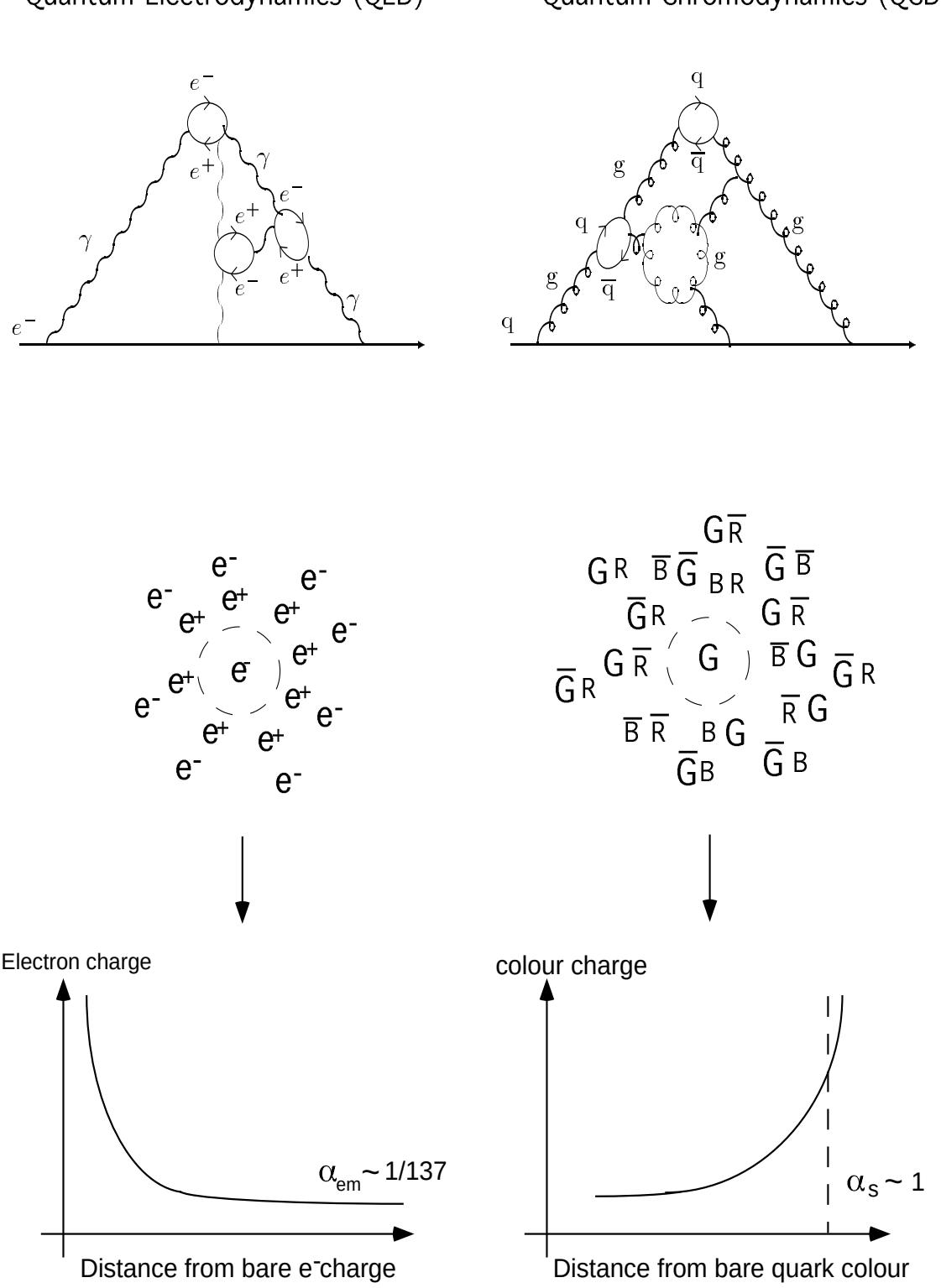

Figure 1.3: Screening of (a) the electric charge by a cloud of virtual electron-positron pairs; and (b) the colour charge by coloured gluon loops and quark-antiquark pairs; the green (G) quark is surrounded by other green, red (R) and blue (B) colour charges. The effect upon the interaction coupling constant is shown.

to approach closer to the quark and penetrate the surrounding screen does the colour force between the two start to reduce. In extreme cases this can lead to a temporary state of non-interaction between the two where they behave as free particles - this is known as *asymptotic freedom.*

1.2.3 Characteristics of the QGP

The effects of colour screening are far reaching. It has been proposed [2] that as a consequence of this phenomenon under very high temperatures and/or densities nuclear matter could undergo a phase transition and 'melt' into an asymptotically free gas of quarks and gluons - the state referred to as a *Quark Gluon Plasma.*

The expression (1.1) for the potential between two quarks does not take account of the presence of the medium in which coloured charges may exist. In a thermodynamic environment of interacting quarks and gluons at a temperature T the quark binding becomes modified by colour screening. It can be parameterized in the following manner [10, 11]

$$V_s(\mathrm{T},\mathrm{r}) \sim \left(\frac{\sigma(\mathrm{T})}{1/\mathrm{r_D(T)}}(1-\exp(-\ (1/\mathrm{r_D(T)})\mathrm{r}))\right) - \frac{\alpha_\mathrm{s}}{\mathrm{r}}\exp(-(1/\mathrm{r_D(T)})\mathrm{r}) \quad (1.2)$$

where r_D(T) is the screening (Debye) radius. It has been shown that as T increases σ(T) approaches zero [12]. Above a critical temperature σ(T) becomes equal to zero and expression (1.2) becomes

$$V_s(\mathrm{T},\mathrm{r}) \ \sim \ -\frac{\alpha_s}{\mathrm{r}}\exp(-(1/\mathrm{r_D(T)})\mathrm{r}).$$

When r_D(T) is less than the binding radius of a particular hadron the confining force will no longer hold the quarks together and so the state will dissolve. If r is very small some level of quark interaction *via* single gluonic exchanges may still exist, but on a scale much smaller than the binding radii of hadrons.

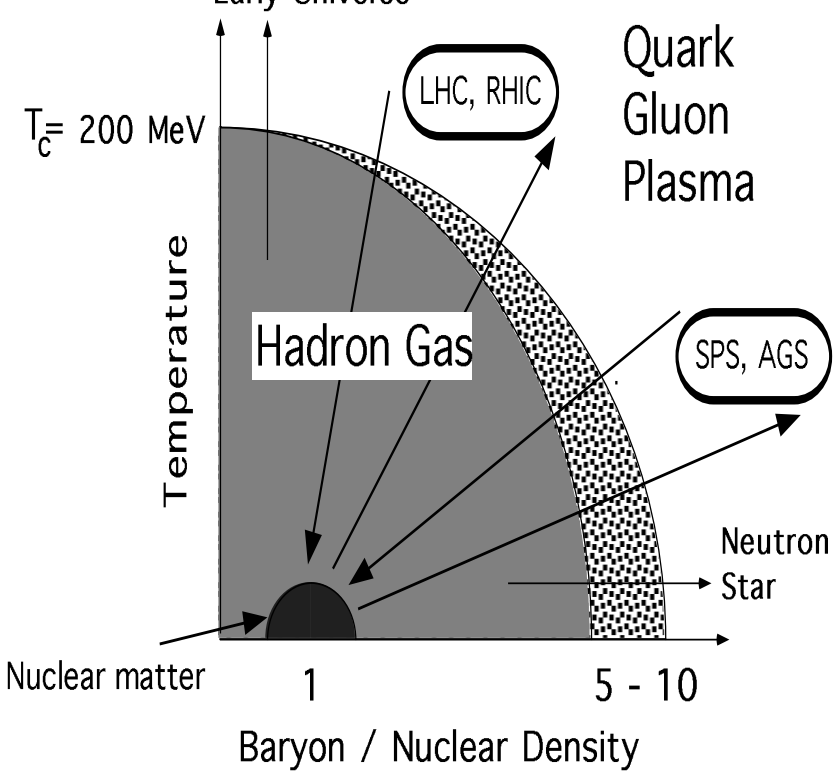

Figure 1.4: Temperature-density phase diagram illustrating the transition from hadronic to Quark Gluon Plasma matter; the various routes across the boundary are shown.

Hot, dense hadronic matter constitutes a large, extended region of particles. A combination of quantum and statistical mechanics are used to analyse such systems, which leads to the introduction of global variables such as temperature. It has been possible to produce equations of state for strongly interacting matter under such conditions within the framework of the MIT bag model [13, 14, 15, 16]. This exercise considers the heating or compression beyond natural limits, set by such global parameters as hadronic density and the temperature of hadronic matter. Indeed, the maximum temperature allowed on the phase boundary was initially predicted to be approximately 150 MeV by the Hagedorn hadronic gas model [17] three decades ago. This is a simplified picture because of the nature of the relationship between these and other parameters such as α_s. The equation of state provides a measure of the density and temperature at the junction between the hadronic and plasma phases of matter. This is illustrated in figure 1.4, which shows the

critical transition temperature is expected to be about 200 MeV. The critical density is estimated to lie in the range 2 to 3 GeV/fm^3, whereas the density of nuclear matter is about $\frac{1}{2}$ GeV/fm^3 [18]. It has been suggested [1] that the matter in the Universe could have existed in the form of a plasma about 10^{-5} seconds after the Big Bang. In addition, the centres of neutron stars have been postulated to be dense enough [3] for them to support a QGP phase [19].

A further attempt to determine whether a phase transition has transpired and under which conditions has been addressed by lattice QCD calculations. Indeed, to cope with the complex conditions inherent to the plasma these calculations may provide the only viable method, because perturbative methods fail in this kinematic region. Questions such as the order of the phase transition can be investigated using these techniques [20]. An example of lattice QCD calculations is given in figure 1.5 where the behaviour of the energy density and pressure for QCD matter with light quarks of two flavours, up and down, has been investigated [18]. At the critical transition temperature, T_c, the energy density undergoes a rapid phase transition from low values, which corresponds to a hadron gas, to much higher values, corresponding to a quark gluon plasma.

1.3 Why Heavy Ions ?

The discussion so far has made no mention of the practicalities related to the formation of hot, dense nuclear matter in the laboratory. Nuclear-nuclear (NN) collisions are thought to provide the most suitable environment in terms of energy density and temperature to allow for a change of state from the ground phase of matter.

There are various advantages to using high energy heavy ion collisions

[3] the density of the core of a neutron star is about ten times that of the nucleus.

Figure 1.5: Energy density ε and pressure P for QCD matter with quarks of two flavours, as a function of the temperature T.

over those of hadron-hadron (hh) interactions, such as proton-antiproton collisions, when trying to create the conditions which could allow a phase transition to occur. Experimentalists are trying to create a large extended region of long-lived matter, whereby the centre-of-mass energy is converted into the thermal energy of the state. The numerous interactions which occur in heavy ion collisions mean that the *Stopping* - fraction of the beam energy dissipated in the collision [4] - is greater than in the more 'transparent' hh interactions. Indeed, the Stopping at the SPS collider energies for NN reactions was found to be about 60% - 70% [21] and even higher for the AGS accelerator (≥ 90 %) [22]. The proportion of thermalised matter, therefore, is higher than in lighter nucleon collisions. In addition, the size of the region of high energy density rises with the increasing atomic weight of the projectile nucleus.

The SPS is expected to approach the QGP phase at slightly higher temperatures and lower baryonic densities than at the AGS, which is a reflection

[4] see Appendix A for further discussion.

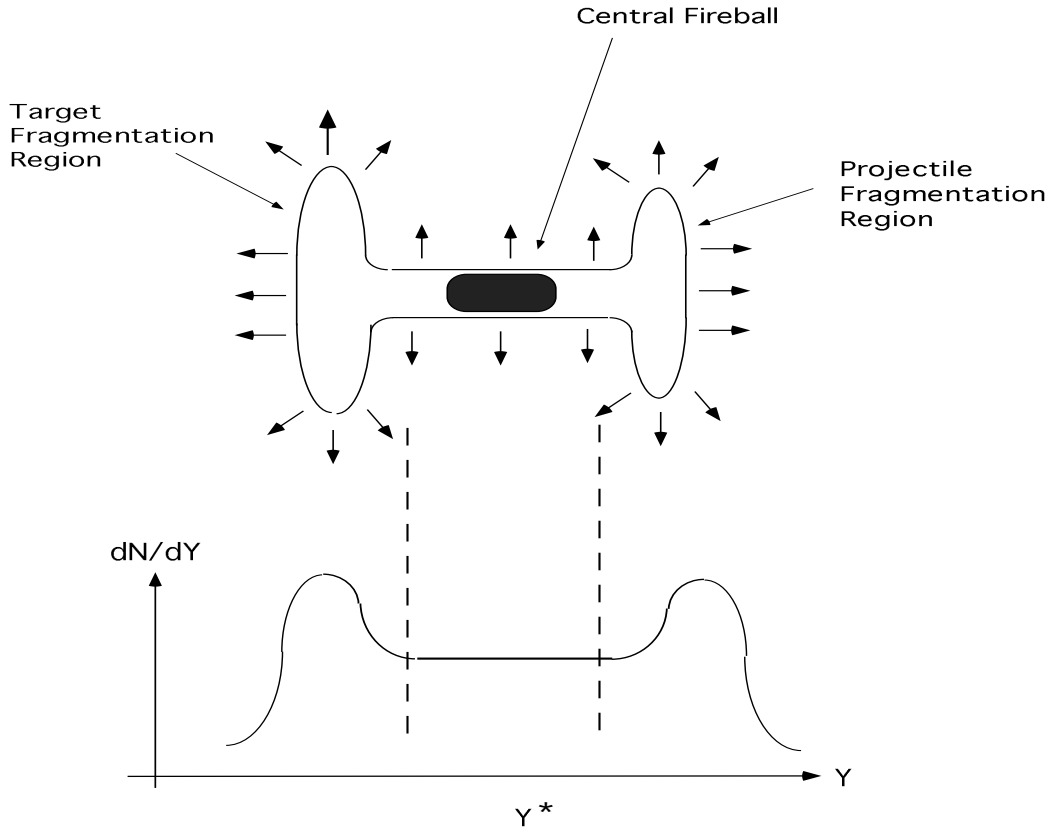

Figure 1.6: Schematic view of a centre-of-mass ultra-relativistic heavy ion collision; the bottom figure shows the rapidity density distribution of baryons. The projectile and target fragments separate leaving the flat baryon-rich plateau.

of the higher energies and lower stopping involved in the SPS NN collisions.

1.3.1 The Dynamics of Ultra-Relativistic Heavy Ion Collisions

The variable rapidity, y, is defined as

$$y = \frac{1}{2} \ln \frac{E + p_L}{E - p_L}$$

where E and p_L are the energy and longitudinal momentum of the particle respectively. Figure 1.6 provides an idealized schematic representation of an ultra-relativistic heavy ion interaction in the centre of mass frame, with the correlation of the different regions of the collision to y^*. Between the forward (projectile) and backward (target) fragments an area of flat rapidity is expected centred on $y^* = 0$, which corresponds to $y_{lab} \sim 2.8$, the rapidity

Figure 1.7: Proton rapidity densities for (a) increasingly larger reactive volumes at AGS energies and (b) for peripheral and central S-S collisions at SPS energies.

in the laboratory frame, for a S-W collision at SPS energies. The central plateau is the region where the 'hot fireball' will be formed. The fireball is where the greatest energy densities are expected to be formed. Figure 1.7 (a) shows how the proton rapidity densities gradually evolve with increasing ion size and centrality [23] and in figure 1.7 (b) the proton rapidity density is shown for NA35 central and peripheral S-S collisions at 200 GeV/c [24] [5] [6].

1.4 QGP Signatures

A scenario for the evolution of a QGP formed by the collision of two ultra-relativistic heavy ions is illustrated in the space-time diagram of figure 1.8. The fireball is expected [25] to last a few 10^{-23} seconds ($\sim$ 5-10 fm/c).

[5] peripheral collisions are those where ions interact at large impact parameter, so most of the nucleons are spectators, see section 2.1 for further details.

[6] it is noted that the higher stopping at the lower AGS energies is reflected in higher baryon densities at mid-rapidity relative to those at the beam or projectile fragmentation rapidities than is found using the SPS.

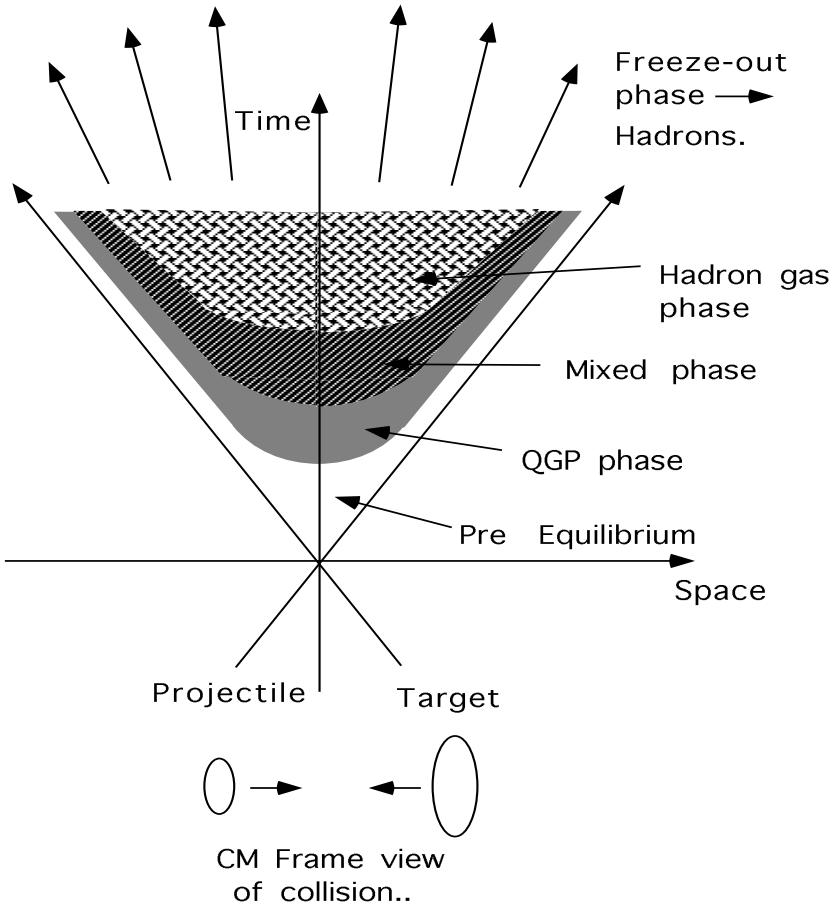

Figure 1.8: Space-time diagram of the longitudinal evolution of a relativistic NN collision.

The temperature will drop due to thermodynamical expansion and particle radiation, mainly pions, from the QGP surface. When the density and temperature have fallen sufficiently hadronization of the transitory QGP state will occur. However, the energy density will be such that further hadronic interactions will occur, having the effect of clouding useful signatures of the former phase's existence. Indeed, the observed yields of particles reflect the properties of the system at freeze-out. So to decipher QGP signatures from the initially hot fireball after hadronisation is no easy matter.

This has led to the requirement that certain criteria be fulfilled if a signal is to be useful to experimentalists.

Either

1. Particle types must not couple to the strong interaction,

or

2. Particle species must have quantum numbers which are invariant under strong interactions.

Several popular signatures will now be considered.

1.4.1 Thermal Photons and Dileptons

Thermal photons and dileptons are the only signals emitted by the QGP that reach the detectors directly. Direct photons are produced in the following interactions

$$q\overline{q} \rightarrow \gamma g$$

and

$$gq \rightarrow \gamma q,$$

whereas the production of leptonic pairs goes *via* the Drell-Yan mechanism, where quark-antiquark annihilation leads to the production of e^+e^- and $\mu^+\mu^-$ pairs. The small cross section for electromagnetic interactions allows the photons and dileptons produced in the plasma to escape. The background for direct photons is dominated by $\pi^0 \rightarrow 2\gamma$ and $\eta \rightarrow 2\gamma, 3\pi^0$ and for dilepton production the decay of πs and kaons to produce a l^+l^- combinatorial background. The rates for both these processes increase as the square of the particle multiplicity, which is a significant problem for heavy ion conditions. This background proved a stumbling block for such signals until recently. The WA80 collaboration saw an excess of γ radiation in central events, where QGP formation is expected, with respect to peripheral data of the order of two standard deviations for $p_T \leq 2$ GeV (see figure 1.9) [26]. At this time the result can only be explained by QGP scenarios. The CERES collaboration [27] however, have not observed such an excess in the collision of S-Au at 200 GeV/c. Both NA38 (see figure 1.10) and NA34 have seen handsome excesses in dilepton production in S$-$W and S$-$U collisions over what would be expected from a straightforward extrapolation of p$-$W data

Figure 1.9: γ/π^0 as a function of p_T for central and peripheral S(200 GeV)Au data. The inclusive photon points are represented by the dots, where the histograms are the photons from all background (hadronic) sources.

[28, 29]. Their excesses though show no evidence of a centrality dependence.

1.4.2 J/Ψ and Ψ′ Suppression

The production of resonant $c\overline{c}$ pairs, such as the vector mesons J/Ψ and Ψ′, is greatly affected by their environment. In 1986, Matsui and Satz predicted a 'suppression' of the J/Ψ yield produced in the unique conditions of a QGP due to Debye colour screening [10]. At the high densities expected for the plasma the colour screen radius will be smaller than the radius of a bound $c\overline{c}$ pair [7] and hence such a bound state cannot be formed in the plasma. The the c quarks will, therefore, preferentially pair with $\overline{u}$ or $\overline{d}$ quarks leading to D mesons rather than join its charge conjugate partner. This mechanism becomes less important above a p_T of a few GeV/c where 'fast' $c\overline{c}$ pairs would have left the plasma zone before the J/Ψ state is dissolved [30]. NA38 have observed a suppression in J/Ψ yields (see figure 1.11 (a)) in O−U and S−U

[7] the J/Ψ radius is ~ 0.3 fm.

Figure 1.10: The observed increase in dimuon production seen by the HELIOS (NA34) collaboration when data is taken with S(200 GeV)W data over that from p(200 GeV)W data.

collisions [28]. The p_T dependence of the suppression is also seen. Unfortunately, the data are also consistent with hadronic re-interaction scenarios, such as $J/\Psi + \pi \rightarrow D\overline{D}X$, which can lead to a depletion of the J/Ψ yield if the medium is dense enough [31]. This motivates a consideration of Ψ' suppression which is believed to be even greater than that of the J/Ψ in a QGP framework, due to its larger radius [32]. Clear evidence for this has been found by NA38 (see figure 1.11 (b)) where the fall off is seen to increase with energy density as predicted.

1.4.3 Entropy

The large increase in the degrees of freedom, particularly for the liberated gluons, allowed by a QGP phase should distinguish it from the hadronic case due to the expected increase in the specific entropy, S. The ratio S/B, where B is the baryon number of the system has been determined by assuming a 3-flavoured QGP (u, d and s quarks plus gluons) [33]. The ratio in a QGP phase was calculated to be at least twice that found in hadronic gas

Figure 1.11: (a) J/Ψ suppression as seen by NA38; R is defined as the J/Ψ to continuum ratio; and (b) Ψ' suppression relative to J/Ψ as the energy density, ε, increases. The box represents the mean value for p−A interactions.

formation under the conditions found by experiments in heavy ion collisions. Experimentally, measurements of the multiplicities of charged particle yields provide a measurement of S. The EMU05 collaboration has measured D_Q, the charge asymmetry to be 0.088 ± 0.007 [34]. D_Q is defined by

$$D_Q = \frac{N^+ - N^-}{N^+ + N^-} \tag{1.3}$$

where N^+ and N^- are the multiplicities for positive and negative particles respectively. The numerator of expression (1.3) is essentially B if it is assumed that the number of positive pions equals that of the negative pions. The denominator of (1.3) reflects the entropy, S, of the system, if N^+ is assumed to be the number of π^-s and protons and N^- the number of π^-s and antiprotons. This result cannot be reproduced by hadronic models and entropy considerations are viewed as being important towards the success of QGP detection.

1.4.4 Strangelets

High energy collisions such as Pb−Pb will offer the possibility of creating strange quark matter (SQM) [35], a state of matter stable relative to nuclear matter, or metastable on the time-scale of weak interactions. This is made possible by a third of the Fermi-sea containing strange quarks lowering the overall energy of the system made of just up and down quarks. However, this reduction in energy must at least compensate for that of the strange quark mass relative to the light quark masses. Such states of matter may be formed under the conditions of very low temperatures and a rich baryonic QGP, which may be the case for the core of a neutron star (refer to figure 1.4). A process known as 'strangeness distillation' could result in the production of strangelets if a QGP is formed [36]. Experiments [37] have attempted to measure the residues of bulk strange matter, strangelets, *via* signals such as $Z/A \leq 0.3$, where Z is the charge of the strangelet and A its atomic number, which is low compared to normal nuclear matter.

1.4.5 Strangeness Enhancement

Enhanced production of strangeness, specifically multistrange antibaryons, was suggested more than 10 years ago [4] as a signature for the QGP. It arises by way of enhanced strange quark yields and a large strangeness density in the QGP phase when compared with that of a hadron gas (HG), as a result of the production time-scales involved in the two scenarios. These two cases will be discussed in greater detail.

Chemical Equilibrium :

The development of a thermal model to interpret data on particle abundances relies upon certain global parameters which characterize the system. The trend towards chemical equilibration of a certain particle species, *i.e.* the progressive saturation of a particular quark flavour, is of particular interest

in determining the yields of strangeness in a QGP or HG. The chemical potential μ is the energy required to add another quark of a particular flavour to the plasma at a temperature of zero (or hadron to a HG); this parameter is highly dependent upon the quark densities residing in the plasma at that time. The chemical potential of light (u and d) quarks is defined as μ_q and for light antiquarks $-\mu_q$, because they may annihilate with quarks of the same flavour already present in the plasma. The net density of strange quarks will be zero in the plasma, because all strangeness production comes from $s\overline{s}$ pair production, so $\mu_s \sim 0$ (strangeness neutrality). This is not necessarily true for a HG, where strangeness production is accompanied by light quarks in the form of mesons and baryons.

The QGP phase :

Initially in the QGP phase gluons are produced in abundance and thermally equilibrate on a timescale of about 0.5 fm/c [34, 38]. Indeed, the gluonic densities are expected to rise with T^3, where T is the mean plasma temperature [39]. So, for an extended plasma region of about 4-5 fm in radius several hundred gluons will be produced. The yields of gluons will lead to high levels of quark-antiquark pair production

$$gg \rightarrow q\overline{q}.$$

Light quark and antiquark production will saturate its phase space and lead to chemical equilibration after about 2-3 fm/c - meaning that the production of light quarks is equalled by their annihilation back to gluon pairs or even other quark species if the energy requirements are satisfied. Strange quark production is somewhat inhibited by the factor $e^{m_s/T}$, as the strange mass of $m_s \sim 150$ MeV is higher than that of the lighter quark masses at about 6 MeV. These masses are the expected 'bare' quark masses residing in a free gas of partons - a result of the partial restoration of chiral symmetry, see table 1.1 [40]. However, since the expected temperature of the plasma is about

200 MeV it should still be quite easy to produce $s\overline{s}$ pairs. The production of strange quarks has been predicted to saturate at approximately 3-5 fm/c [34, 38]. The light quark yields will be suppressed by Pauli blocking; the large baryochemical potential $\mu_B (= 3\mu_q)$, resulting from the high u and d quark densities inherent to an ion collision, will inhibit the production of light quarks and antiquarks by a factor $e^{\mu_B/3T}$. This tends to increase the yield of especially $\overline{\mathrm{s}}$ production relative to $\overline{\mathrm{u}}$ and $\overline{\mathrm{d}}$.

The HG phase :

The production of strangeness in confined matter is complicated by many contributing cross sections of the nature $h_1 + h_2 \rightarrow h_3 + h_4$. For example, reactions such as

$$\begin{aligned} pp &\rightarrow pK^+\Lambda, \\ pp &\rightarrow pK^+K^-p \\ \text{and} & \\ pp &\rightarrow pp\Lambda\overline{\Lambda} \end{aligned}$$

produce strangeness in the primary collision *i.e. via* the interaction of the constituents of the projectile and target. Secondary rescattering interactions such as

$$\begin{aligned} \pi^-p &\rightarrow \Lambda K^0 \\ \text{and} & \\ \pi^-\pi^+ &\rightarrow K^+K^- \end{aligned}$$

are also responsible for the production of strangeness. Both these processes will either alter the strangeness of a hadronized QGP or be responsible for the entire strangeness production if no plasma is formed. However, the minimum required centre-of-mass momentum for the production of Λs is 522 MeV/c and for $\overline{\Lambda}$s is 1.83 GeV/c. Hence, the saturation of strangeness, particularly in baryonic form and especially in antibaryonic form, will be much slower

[34]. Indeed, the approach to strangeness saturation for a QGP has been estimated at 2-3 $\times 10^{-23}$ seconds which is about the expected lifetime of the fireball and $10 - 100$ times faster than in a HG [41].

To summarize, due to the high threshold energies required to produce strangeness in hadronic interactions with respect to the QGP case, the yields of strange baryons and especially multistrange (anti)baryons should serve as an important signal for the formation of a QGP [42]. It is for this reason that the relative abundances of $\overline{\Xi^-}$s to $\overline{\Lambda}$s , for example, could be sensitive to a phase transition in the system and such evidence to date will be reviewed in chapter 6.

1.5 Hadron-Nucleus Ultra-Relativistic Collisions

Any experiment wishing to study the relative production yield of strange particles in heavy ion collisions must also consider the same production in the cleaner environment of hadron-nucleus (hN) collisions, which is firmly fixed in the field of hadronic physics. Strangeness enhancement in sulphur-tungsten interactions with respect to the normal hadronic production of strangeness in proton induced interactions can be estimated by comparing the two systems in the same kinematic window. Hence such control experiments should provide the link between hh and NN interactions. Various experiments [43, 44, 45, 46] have undertaken hN minimum bias experiments and report a strangeness enhancement. The strange baryon production rate observed is a factor of two above that expected from a superposition of hh collisions. There are various explanations for such an effect which will be reviewed in chapter 6.

1.6 Summary

The observation and characteristics of such a 'new' phase of matter as the QGP has undoubted consequences upon the theory of strong interactions, QCD, and could well lead to a further understanding of the behaviour of the Universe in its very early evolution. Indeed, there has been speculation over whether the phase transition could have been responsible for the current inhomogeneities *i.e.* matter clumped together in galaxies [47, 48]. Various signatures which could point to an observation of QGP have been published using the data from Brookhaven and CERN. The newer breed of fixed target 'very heavy' ion collisions and the new stage of colliders such as the LHC at CERN and RHIC at Brookhaven should add to this wealth of evidence.

The basis of this thesis is concerned with the p−W experiment carried out by WA85 in 1990 and the associated production of strange particles, such as V^0s and cascades. This control data, as discussed in the previous section, is essential to the understanding of the dynamics of nuclear matter and will be used as a comparison with the WA85 S−W published data in chapter 6.

Chapter 2

The WA85 experiment : Proton – Tungsten Apparatus and Trigger.

2.1 Introduction

The WA85 [49] experiment was designed to explore the nature of the central fireball region created in an ultra-relativistic S−W interaction and to search for the possible phase transition to a new state of matter - the Quark Gluon Plasma; strangeness enhancement is used as the signature. To this end, WA94 and WA97 [50, 51] have worked in complement with WA85. These two newer breed of experiments have undertaken various runs using different targets and in the case of WA97 different incident ions. To be able fully to appreciate the extent to which strangeness is enhanced in an ion collision the production of strangeness achieved in the cleaner environment of hadron−nucleus (hN) interactions must also be investigated. In this case, the fireball region is far smaller which leads us to believe that the exotic QGP

state will not be formed and so such data serves as a control. This chapter is mainly concerned with the details of the experimental setup and trigger for the 1990 run, where 200 GeV/c protons were collided with a tungsten target.

Requirements for Event Selection:

In order to study strange baryonic enhancement WA85 concentrates on the detection and reconstruction of the following decays

$$\Lambda \rightarrow p + \pi^-$$

$$\Xi^- \rightarrow \Lambda + \pi^-$$

$$\Omega^- \rightarrow \Lambda + K^-$$

and their corresponding antiparticle decays. So it is vital to measure V^0 decays such as Λs and $\overline{\Lambda}$s .

The experiment was designed to detect only particles produced in a narrow kinematic window of *'medium to high transverse momentum* (p_T)', and *'central rapidity'*. Strange hadrons are studied if they have $p_T \geq 1.0$ GeV/c. These types of particles are of most interest, because they are directly correlated to the 'hottest' and densest regions of the collision [52]. The tracking detectors were made sensitive to tracks from the target whose transverse momentum was greater than 0.6 GeV/c. The region of highest energy density in the collision is where the centre of mass rapidity is zero, $y_{lab} \sim 2.8$ for the WA85 scheme. This is the area of greatest interest where the fireball will be formed. For this reason WA85 restricted itself to consider only target tracks in the rapidity interval $2.0 \leq y_{lab} \leq 3.2$.

The Heavy Ion Environment:

The kinematic region covered by WA85 eliminates much of the low momentum background produced in S−W collisions, which would greatly hinder

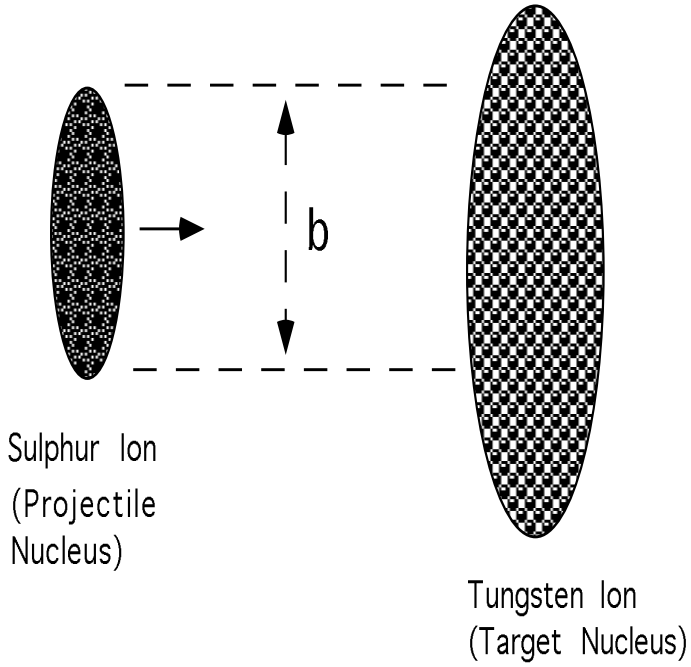

Figure 2.1: Schematic illustration of a head−on NN collision, where b is the diameter of the sulphur projectile.

the identification of strange particle decays. It is found that the reconstruction efficiency of tracks and especially decays is strongly influenced by the multiplicity of tracks in the event. In central ion collisions large numbers of charged tracks are produced per event, around 600 per central S−W interaction. In addition, it was the intention of WA85 to concentrate data taking in the region of greatest interest, so providing sufficient statistics to be able to compare hyperons of differing strangeness content in the kinematic window discussed. The one drawback is the loss of global information on such parameters as rapidity.

The events collected from the S−W run were of a 'head−on' (central) nature, as illustrated in figure 2.1. The trigger requirement for central event selection in the S−W run was satisfied by a cut in the forward energy using a hadron calorimeter 25 m downstream of the target and selecting events above a certain multiplicity using information from silicon microstrips which sampled the track multiplicities centered on mid−rapidity.

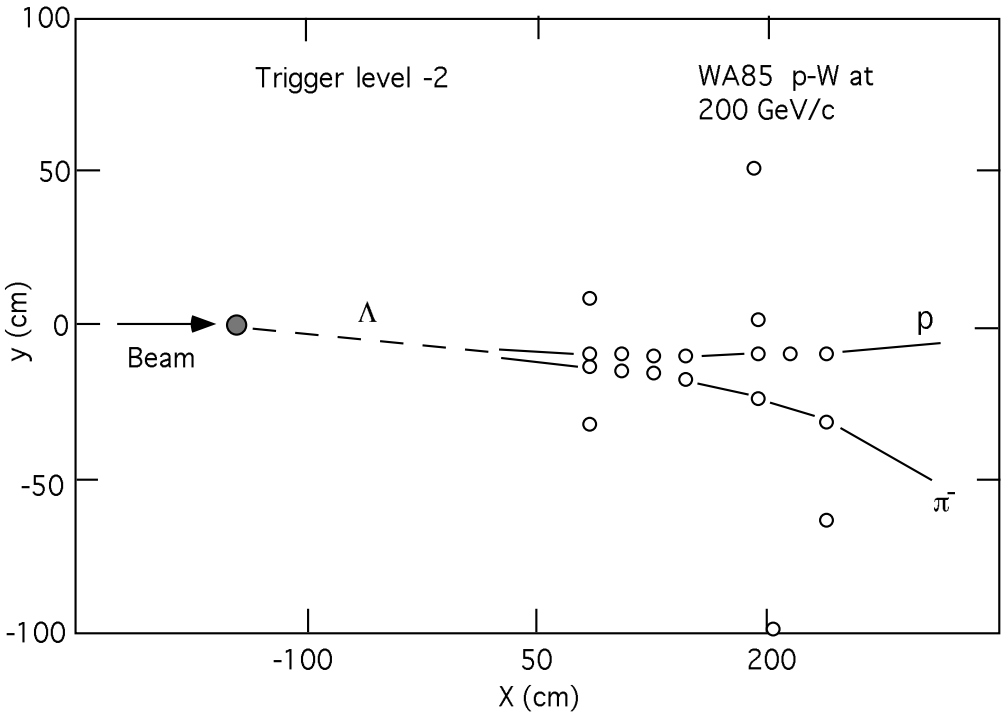

Figure 2.2: A typical Λ candidate reconstructed using the 7 Omega MWPCs in a WA85 p-W 1990 event.

In the proton run the same kinematic window is covered as for the sulphur run. Given different tracking detectors to those used in the S−W run the multiplicities characteristic of p−W reactions [1] could have allowed a larger phase space coverage. However, the main intention of the run was a direct comparison with the sulphur data. The trigger concentrated on collecting a high statistics yield of hyperons in proton induced events which in previous WA85 p−W runs had proven a stumbling block. A typical Λ candidate which has been reconstructed from a proton-tungsten event is given in figure 2.2.

2.2 The WA85 Experiment

2.2.1 The WA85 Runs

The WA85 experiment took data between the years of 1987 to 1990. During this period the experiment collected data from two sulphur runs and three

[1] the average multiplicity associated with a p−W collision is approximately 15 charged tracks per event.

proton runs; for the S−W data in 1987 10^7 triggers were recorded and in 1990 a further 6×10^7 were taken. The improvement of the proton trigger compared with the 1988 and 1989 versions helped to enhance V^0 detection in the 1990 proton exposure, where 8×10^7 triggered events were written to tape.

2.2.2 Beam

To provide a beam of 200 GeV/c protons (equivalent to the 200 GeV/c per nucleon sulphur ion beam) a 400 mm beryllium target was positioned in the H1 beam line where the 450 GeV/c proton beam is extracted from the SPS. A beam of 200 $\pm$ 0.5 GeV/c protons was selected using a combination of collimators and bending magnets. The beam was steered and focussed onto the tungsten target *via* dipole and quadrupole magnets respectively. The proton beam contains a small amount of contamination at this energy, mainly from pions which contribute about one in three of the particles arriving at the target. These were vetoed using two Čerenkov differential counters, see section 2.4.3.

2.2.3 The Omega Spectrometer

The WA85 experiment used the Omega Spectrometer (Omega) which is a multi−user 'facility' situated in the West Area at CERN [53]. The experimental layout is shown in figure 2.3. Omega essentially consists of a superconducting magnet whose two Helmholtz coils produce a close to uniform field of 1.8 tesla. The target and the majority of the detectors for track identification and triggering are placed inside the approximately 6×6 m^2 area of Omega. The detector layout used in the experiment was symmetric with respect to charge so that particles and antiparticles have the same acceptance. In addition, the data were taken with both field polarities. This

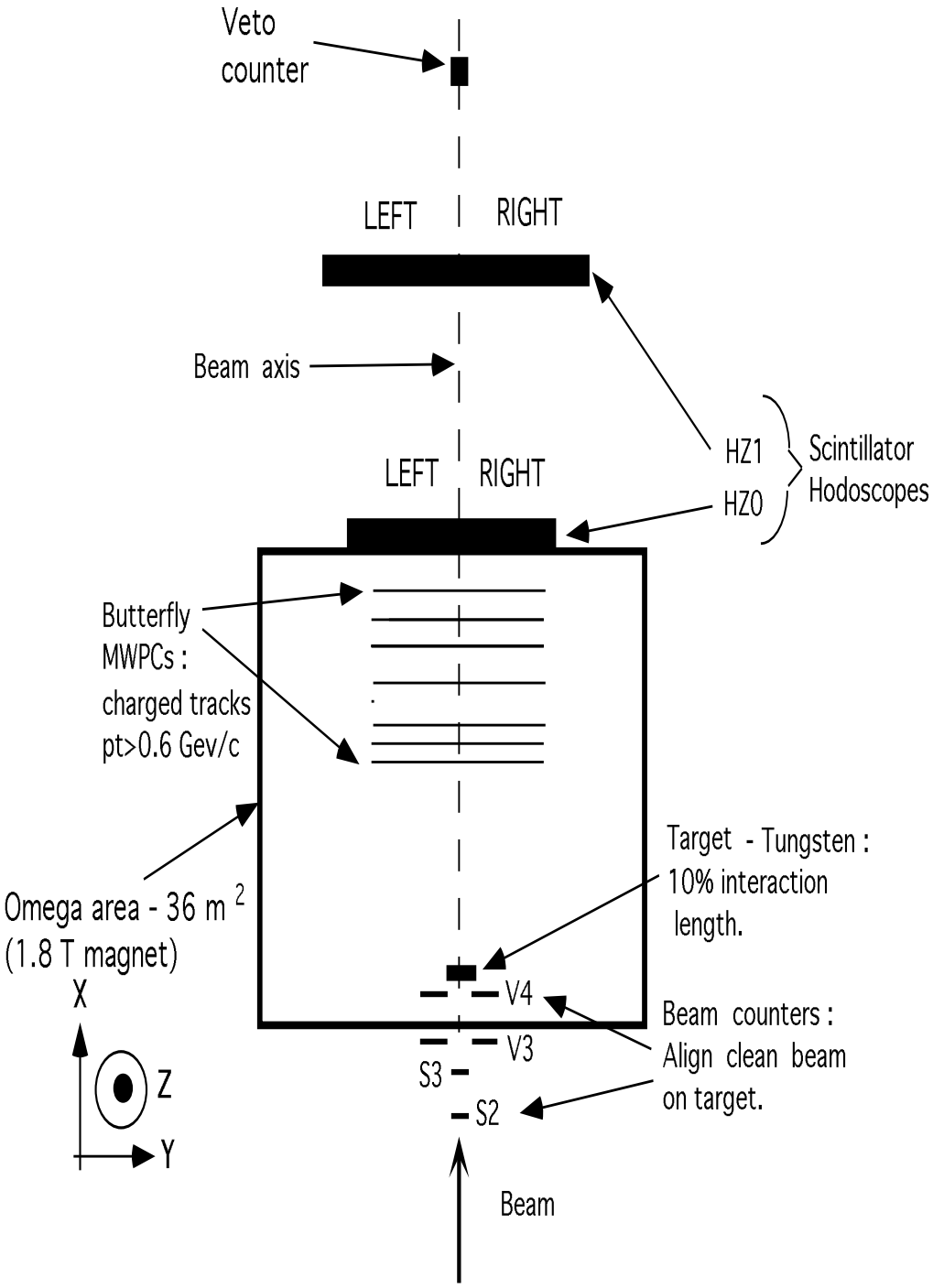

Figure 2.3: The WA85 experimental layout for the 1990 proton run.

helped as a valuable aid in the fine alignment of the wire chambers, so reducing systematic errors. This thesis uses a system of coordinates defined in terms of the Omega spectrometer. In this system the beam hits the target at $y = 0$ cm, $z = -0.5$ cm, travelling along the $x-$axis. The main component of the magnetic field is directed along the $z-$axis. Zero x is defined at the centre of Omega.

2.2.4 Target

The target was positioned at $x = -140.1$ cm. For the 1990 proton run the target thickness was of 8 mm, which corresponds to a 10% interaction length. When using the tungsten target for the sulphur run more care was taken to reduce multiple interactions. This can result from the partial break$-$up of the ion on primary collision with the target and lead to subsequent secondary fragment induced collisions which fake central interactions. Also, γ conversions inside the target are increased with the atomic number of the projectile ion adding to an already noisy environment. Therefore a target of 0.5 mm thickness (1.2% interaction length) was used; in the proton case this problem is negligible.

2.3 The Detectors used in the 1990 Proton Run

The Omega set up for the proton run was quite simple consisting of seven multiwire proportional chambers (MWPCs) - the 'A chambers' - and two scintillator hodoscopes (HZ0/HZ1). Approximately 54 m upstream of the spectrometer and aligned within the beam were two threshold ČErenkov Differential counters with Achromatic Ring focus (CEDARs). The purpose of these was to veto beam particles that were not protons. In addition,

Figure 2.4: View of section through an Omega A chamber: The three wire planes are shown with the cathode planes separating them by 16 mm.

various scintillator beam counters were used for trigger purposes in the run, see section 2.4.1.

2.3.1 Butterfly A Chambers

Seven MWPCs were used as the tracking detectors in all the WA85 runs; they provided the basis for track reconstruction and momentum fitting. The first four of these chambers were incorporated into the 1990 proton trigger, see section 2.4.4. A cross section of one of the A chambers is shown in figure 2.4. The A chambers consist of three wire planes known as U,Y and V. The Y plane wires are vertical and as the name suggests is responsible for measuring the y position of tracks. The Y plane is the central one of the three planes. The wires of the U and V planes are respectively inclined at $+10.14^o$ and -10.14^o to the vertical. The 752 anode wires in each plane are spaced at 2 mm intervals. The gas used was an argon, iso$-$butane and ethanol mixture and the cathode planes, made of 12 μm mylar foil coated with conductive

graphite paint, are separated by 16 mm with the wire planes placed between. When a track passes through a wire plane a 'cluster' is produced. A 'cluster' or 'hit' is a number of adjacent wires which fire in any particular plane. The seven chambers were positioned at x = 90, 109, 128, 147, 190, 215 and 240 cm.

As discussed WA85 concentrates on a specific kinematic region. This is seen in the distinctive feature of the wire chambers, their so called 'butterfly' geometry. This design sensitized the chambers to select tracks of $p_T \geq 0.6$ GeV/c. To illustrate the geometrical technique used by WA85 the following example is studied. With the magnetic field off, the locus of tracks originating from the target, at some reference plane orthogonal to the beam axis, will sweep out a circle of radius, R, which is given by

$$R = x \cdot \frac{p_T}{p_L}$$

where p_L is the longitudinal momentum of the track. So taking tracks with a fixed p_T, those whose p_L is smaller trace out larger circles. With the magnetic field switched on, the tracks with lower p_L are swept out further from the beam axis. If for a given p_T all values of p_L are considered, the envelope of these circles will form two V shaped regions in the reference plane and thus define the butterfly region as illustrated in figure 2.5.

So tracks from the target with a p_T less than p_{Tmin} cannot enter the shaded region. On average, 30% of the target tracks with $p_T \geq 0.6$ GeV/c are accepted by the active region of the chambers. Only the upper hemisphere was used in the experiment.

The A chambers are rendered insensitive in the relevant regions by removing graphite paint on the cathode planes, so electrically isolating the 'butterfly' areas. The active region of the cathode planes is held at a potential of 4.8 kV, whilst the insensitive area is held at a potential just below that at 4.3 kV to reduce sparking due to leakage from the higher potential zone

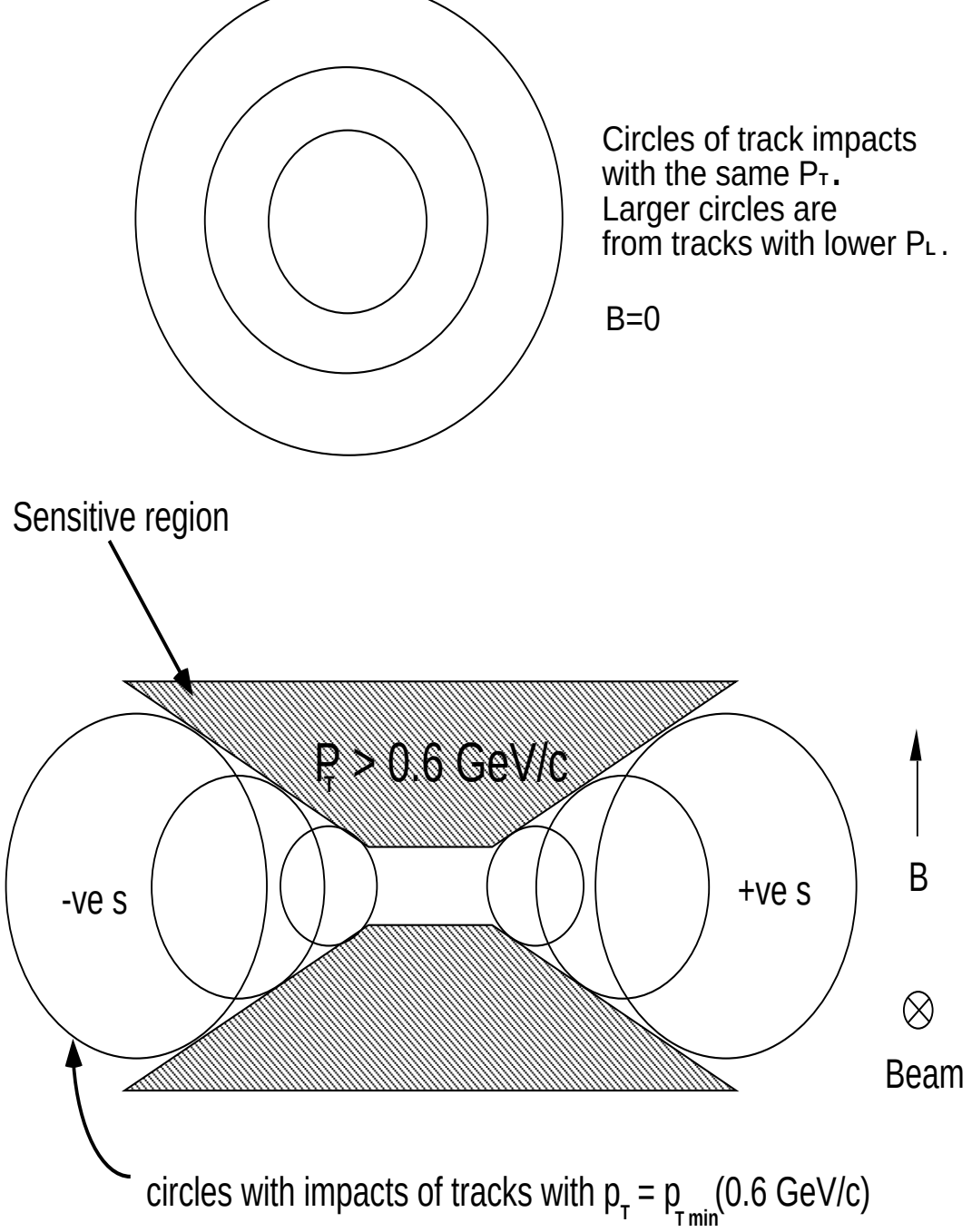

Figure 2.5: The V shaped regions defining the butterfly geometry. The impacts of tracks with $p_T = p_{T\,min}$ are shown.

[54]. The shape and size of the sensitive region varies from chamber to chamber, ensuring that the geometrical acceptance is similar for each MWPC. The average number of tracks per event is ten in S−W collisions and, depending upon the trigger conditions, about one track in every five events for the proton interactions at the level 1 stage of the trigger, see section 2.4.3. Hence, the data are more manageable, quicker to record and process.

2.3.2 The Hodoscopes

The two scintillator hodoscopes HZ0 and HZ1, were used for trigger purposes in the proton run. Both were situated at the edge of the Omega field region, downstream of the target, with HZ0 at an x position of 277 cm just beyond A7 and HZ1 at 480 cm. Each consists of fifteen horizontal slabs, of which the top five were active, so that they subtend the same solid angle at the target as the MWPCs. The slabs were split into two logical halves in the horizontal plane, right and left, for use in the trigger, see section 2.4.3.

2.4 The 1990 Proton Trigger

The basis for the 1990 proton trigger is described in the following section. A good quality trigger is priceless to any high energy experiment. Its use is to ignore all events whose character is sufficiently different from those which form the main interest to the experiment. The trigger defines these characteristics using detector information. The proton trigger for the 1990 run is shown in figure 2.6 and represented in the flow diagram of figure 2.7.

The aim of the 1990 proton trigger was to enhance the detection of V^0 events without wasting time collecting huge amounts of 'useless' data. The trigger was developed from earlier versions in previous WA85 proton runs, which will also be considered.

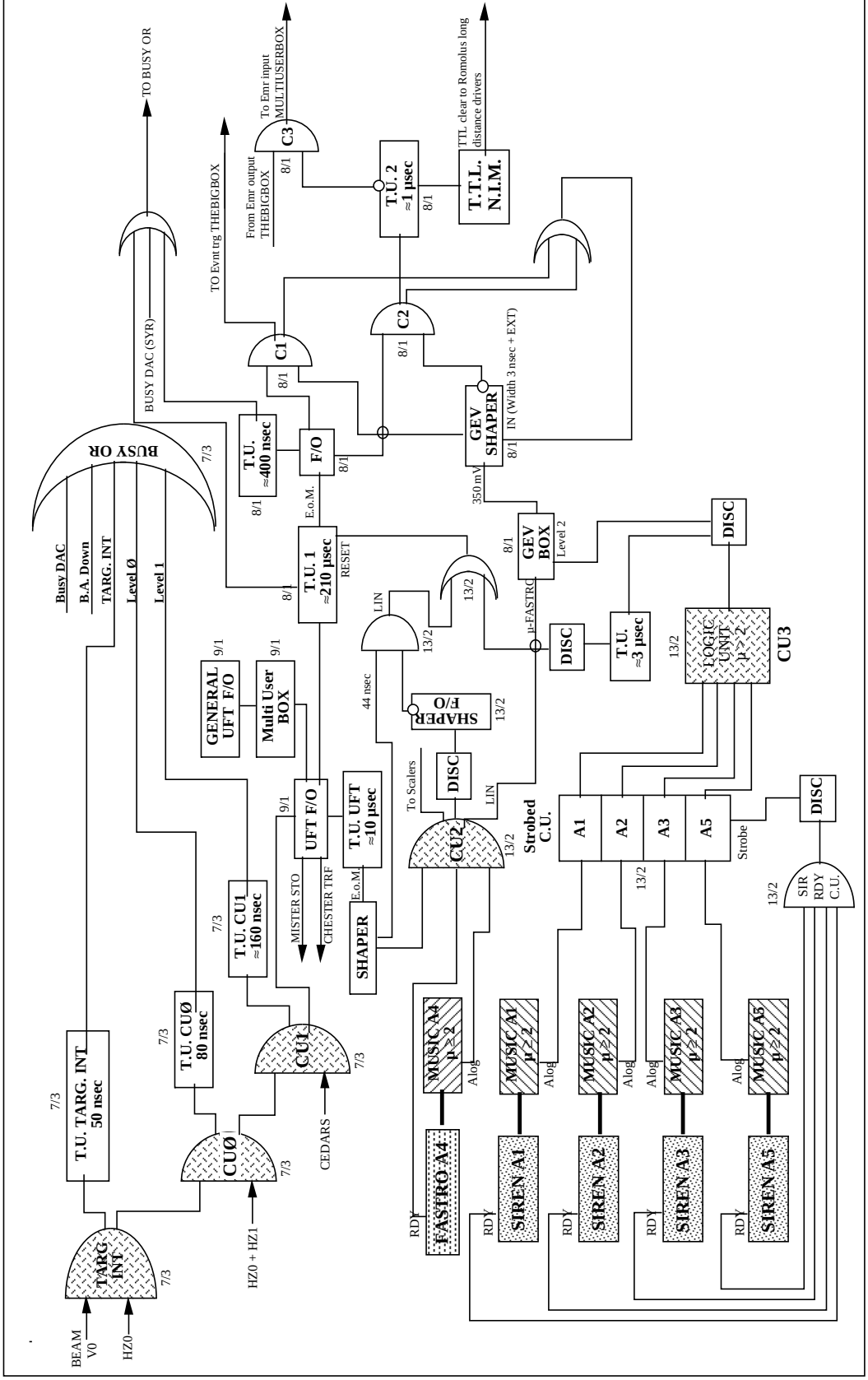

Figure 2.3: WA85 proton trigger.

Figure 2.6: Trigger diagram for the 1990 p−W run.

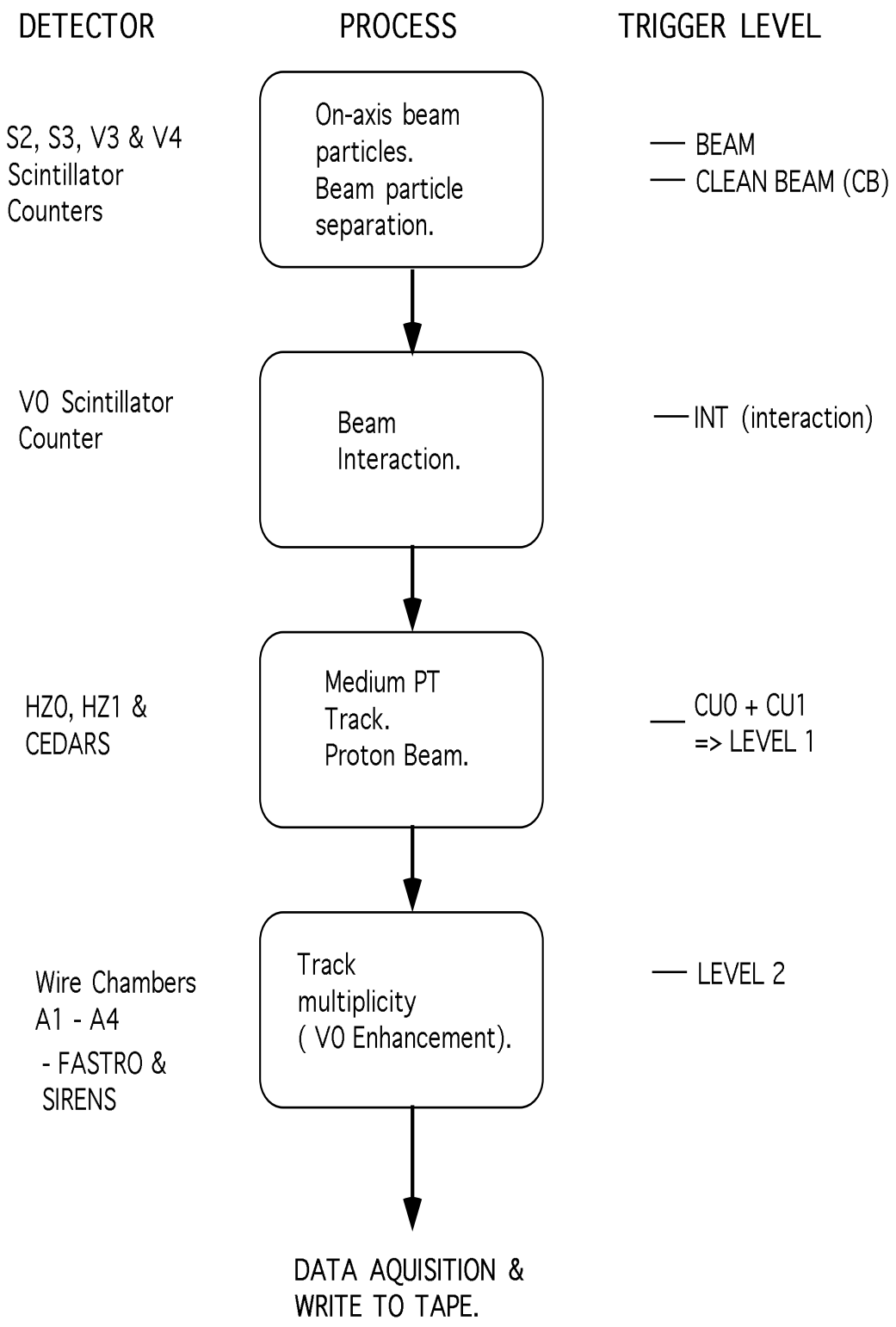

Figure 2.7: 'Flow' diagram illustrating the essential elements of the proton trigger.

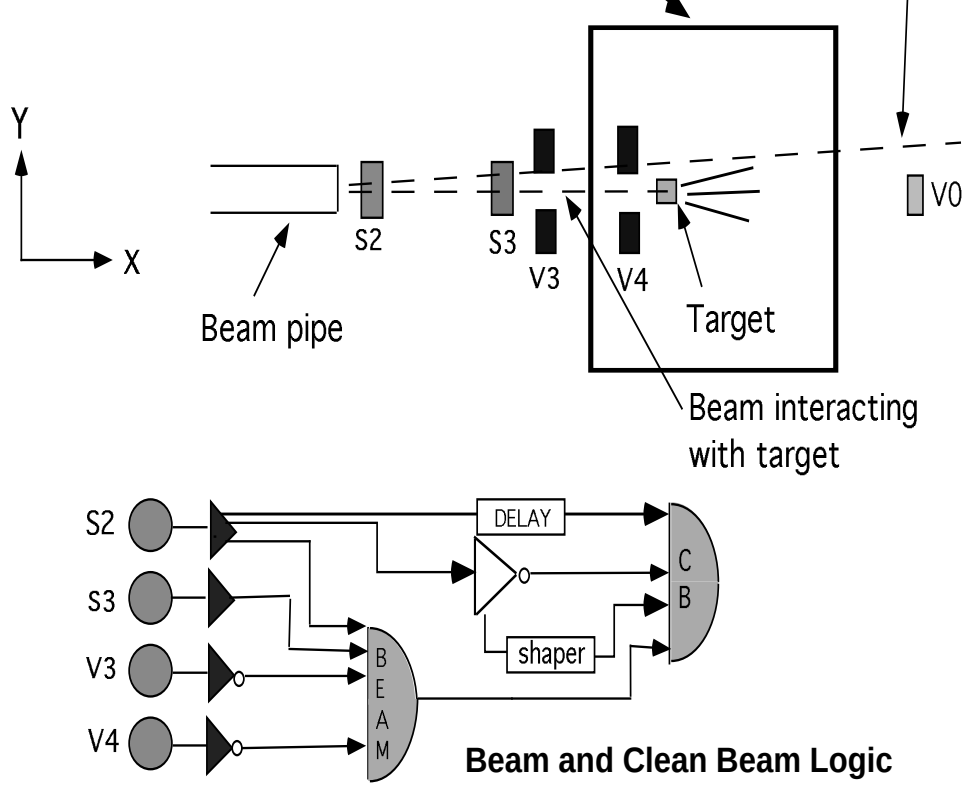

Figure 2.8: Schematic diagram of the relative positions of the scintillator beam counters used for good beam definition; the beam logic is illustrated below.

2.4.1 The WA85 1990 Proton Trigger

The Beam Counters: The beam counters were used at the lowest levels of the trigger. Their purpose is to provide a clean beam aligned on the target. Five scintillator counters were required, **S2, S3, V3, V4** and **V0**, the arrangement of their setup is shown in figure 2.8 as well as the arrangement of the beam logic. **S2** and **S3** were aligned within the beam and positioned upstream of the target. **V3** and **V4** are square counters with a central hole whose diameter is of the order of a few centimetres, sufficient to allow for passage of the beam and its halo. Again these veto counters were placed upstream of the target and detect off−axis beam particles. The **V0** veto counter was positioned downstream of the target on the beam axis and its purpose was to ensure an interaction at the target.

2.4.2 Trigger Logic

Beam : This level of trigger requires a signal from **S2** and a signal from **S3** which is in coincidence with that from **S2**. The coincidence reduces the possibility of triggering on noise in **S2**. Beam also requires no signal in **V3** or **V4** .

$$\mathbf{BEAM = S2 \cdot S3 \cdot \overline{V3} \cdot \overline{V4}}$$

Clean Beam : This trigger level asks for no further signals in **S2**. It is important to discount triggers which can be the result of two separate interactions, such as when two protons are too close together in time. Part of the signal from counter **S2** is passed to an updating discriminator. The effect is such that a second **S2** signal arriving at a time Δt after the arrival of the first signal will lengthen the output time of the updating discriminator signal $\overline{S2_p}$ by Δt. This signal will then be in an anticoincidence with the other three input signals to the clean beam coincidence unit, so vetoing the event. The delay, Δt, was set at 20 ns.

$$\mathbf{CB = BEAM \cdot S2_{p'} \cdot \overline{S2_p} \cdot S2}$$

This *past future protection* logic is illustrated in figure 2.9.

Interaction Trigger : INT requires the coincidence of a beam trigger and the absence of a signal in **V0** with a minimum requirement of one 'hit' in any of the active slabs of HZ0.

2.4.3 Level 1

After an interaction and clean beam have been established correlated 'hits' in the two hodoscopes are needed along with the CEDARs to provide the **Level 1** stage of the trigger.

At least one 'hit' in both RIGHT or LEFT halves of HZ0 and HZ1 is asked for. The main component of the magnetic field is in the vertical direction, so

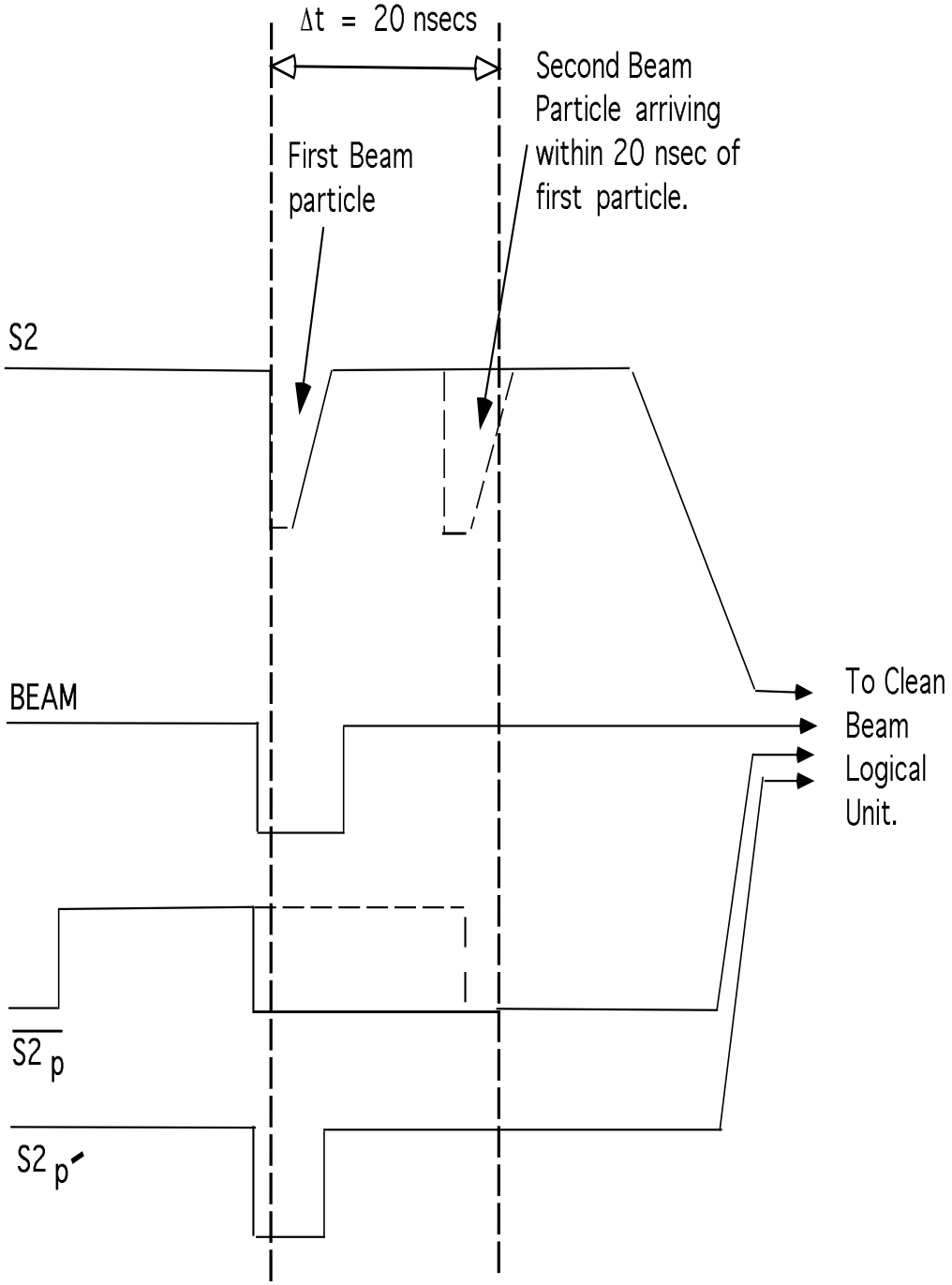

Figure 2.9: The input and output signals to the *past–future protection* 'clean beam' coincidence unit.

positive and negative tracks will tend to be swept to different halves of the hodoscopes. Therefore this condition enhances the likelihood that events will contain at least one track of medium to high p_T so reducing the probability of triggering on electronic noise. The hodoscope condition enters the trigger at coincidence unit zero (CU0). Level 1 is satisfied at coincidence unit one (CU1), where the CEDARs provide a signal if the beam particle is identified as a proton.

2.4.4 Level 2

The full level 2 trigger was designed to enhance events with V^0s for the proton run [55]. The wire chamber A4 was fitted with a FAST Read−Out, known as **FASTRO** which allows quick event rejection, saving approximately 200 μs per event for those events which are rejected. A minimum multiplicity of 2 clusters in the Y plane of A4 is required; this fulfills the FASTRO stage of the level 2 trigger.

FASTRO uses modules covering 8 wires each over the entire wire range of the Y plane of A4. It provides information upon the multiplicity of clusters in each of these modules. If this requirement is fulfilled then only events with a further two clusters in the Y planes of two out of the first three chambers are accepted. This cluster information is asked for by the slower SIREN read−outs on the Y planes of A1, A2 and A3. This biased the experiment towards a higher yield of two or more tracks per event, so that the production rates for V^0s and cascades was enhanced. The requirements of the level 1 and level 2 stages of the trigger are noted in figure 2.10. This final trigger level provided about 1000 triggers/burst from $\sim 2 \times 10^6$ incident protons.

Unfortunately during data taking approximately a third of the wires required for triggering on clusters in the fourth chamber were disabled from the trigger and hence there was a loss of data at the level 2 constraint of the

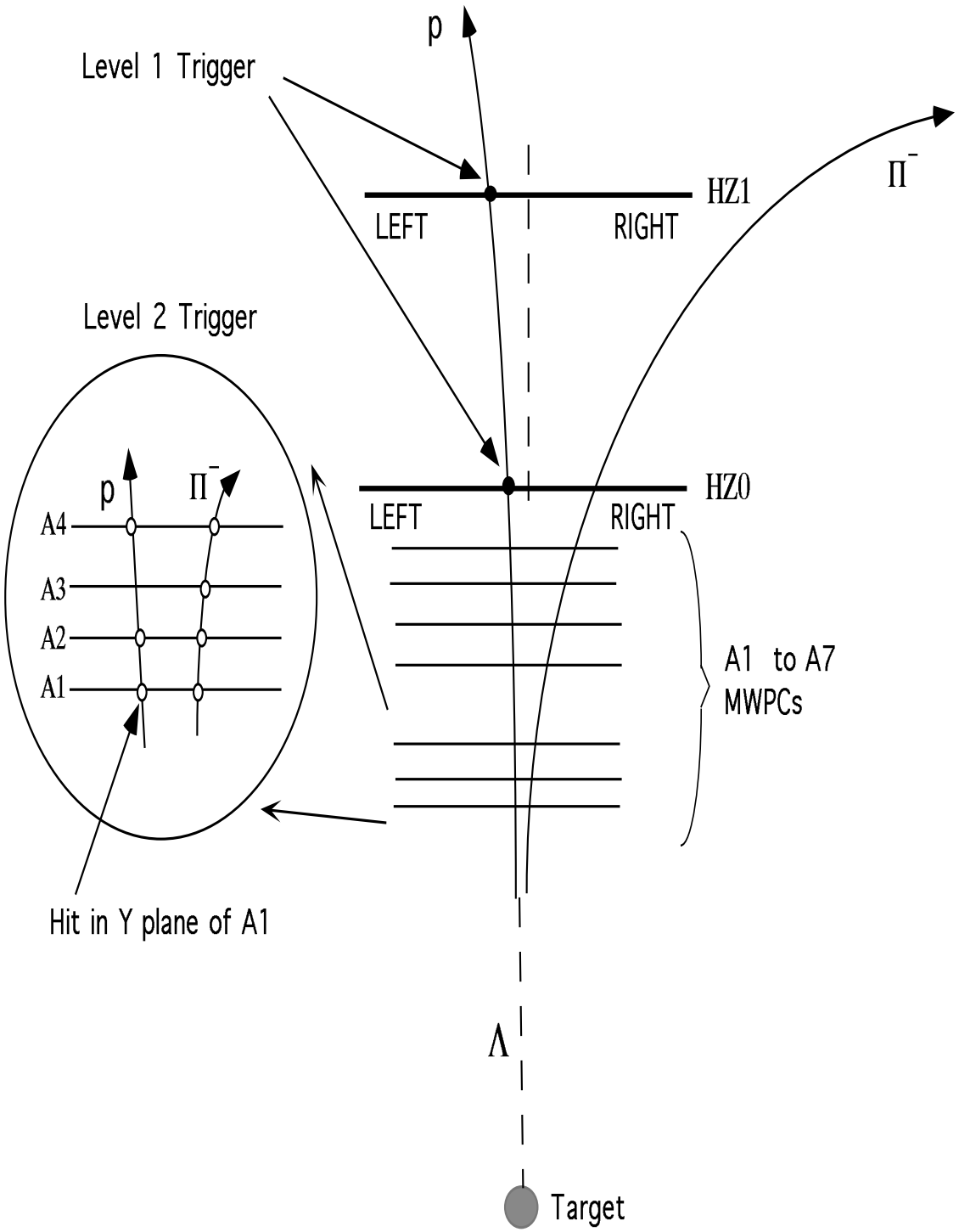

Figure 2.10: Schematic illustration of the level 1 and level 2 triggers requirements being satisfied by Λ decay tracks passing through the MWPCs and two hodoscopes.

trigger. A study concerned with the region of the Y plane wires on the A4 chamber that were not included in the level 2 trigger is now presented.

2.5 FASTRO disabled wires

There were 94 modules (cards) used to cover the range of 752 wires in the Y plane of A4. Of these 94 modules 33 were disabled which meant that as far as the trigger was concerned any information on the wires covered by these modules was lost, even though the wires themselves were read out as normal. The disabled modules covered the regions of wires given by

$$\textbf{Wires} \rightarrow \textbf{0 - 215},$$

$$\textbf{Wires} \rightarrow \textbf{704 - 752}.$$

A study to corroborate these regions was carried out.

The ratio of level 2 over level 1 wire distributions across plane Y of A4 was considered. The result of which is given in figure 2.11. Clearly the discontinuity seen over wire numbers 215 to 216 is a result of the disabled modules biasing against events in the region of wires, 0 - 215. However, there is not such an obvious discontinuity in the latter region, 704 - 752. The statistics in this area were found to be lower and so a further investigation was undertaken using only level 2 data. Events with the minimum triggering requirement of only 2 clusters on the Y plane of A4 were considered. These events were asked to lie in the range 216 to 752, the end of the wire plane. The result is displayed in figure 2.12 (a). The discontinuity noted at wire 704 is due to the fact that none of the events with the minimum trigger requirement had clusters in this region, confirming the expected disabled area in the high range of wire numbers. Similarly the test was carried out for the region of wires 0 to 703. This second result is shown in figure 2.12 (b). An estimate

Figure 2.11: Wire distribution ratio on the Y plane of A4 of level 2 triggers over level 1 triggers; the steep fall in the ratio in the outer regions of the wire plane is noted, especially at wire 215 to 216.

Figure 2.12: Level 2 wire distributions across the Y plane of chamber A4 (a) for events with 2 clusters on the Y plane of A4 within the wire regions ranging from 216 to 752 ; and (b) for events with 2 clusters on the Y plane of A4 within the wire regions ranging from 0 to 703.

of the consequence of this inefficiency in the highest level of the trigger upon different particle yields and kinematic spectra will be considered in section 6.3.

During the run data were taken using various settings of the trigger level. The bulk of the data was level 2 (6×10^7 triggers) used for the main hyperon analysis, the other 2×10^7 events were taken using only the level 1 trigger in order to compare strange decays with single track events, such as π^-s and to determine chamber efficiencies, see section 4.1. In addition, some interaction triggers were taken to enable hodoscope efficiencies to be calculated, as described in section 4.2.

2.6 The 1988 WA85 Proton Run

The 1990 p−W run was in many ways a development from the earlier 1988 proton run that WA85 undertook. Both trigger arrangements required the same trigger up to the interaction level and used the CEDARS to define a proton beam particle. However, in the preliminary run the level 1 stage of the trigger was substantially altered. At least one hit was asked for in HZ1 and at least one correlated hit in the active slabs of HZ0 and HZ1 (*i.e.* corresponding slab numbers are hit); this was known as the MBNIM trigger. However, this biased the trigger towards accepting tracks from the target and not necessarily tracks from V^0 decays which do not point to the target. The low statistics yield of V^0s and cascades prompted the introduction of the new level 1 and level 2 triggers for further proton exposures.

The enhancement of Λs and Ξ^-s from the 1988 to 1990 data was found to be 8.8 ± 0.2 and 9 ± 2 respectively, see sections 3.1.3 and 3.2.2.

2.7 DAQ and Offline processing

The data taken in the run which satisfy the highest trigger levels were written to tape in EPIO 16 bit word format [56]. The EPIO format was written specifically for scientific applications with the distinct advantage of its machine independence. These raw cartridges contain all the electronics information, such as the MWPC and hodoscope hits, along with a header which provides details of the event record such as the length of the electronics block, event and run numbers. The electronics data is stored in a tree structure called the ROMULUS block. A specific 'address' will, for example, allow information on the wires which fired in a specified chamber plane to be extracted.

These raw data tapes are then dealt with by offline processing which uses a modified version of the TRIDENT program [57]. TRIDENT's job is to reconstruct tracks in events using the wire hit information. Initially the hits from the U, Y and V planes of each chamber are used independently to build up tracks in the MWPCs. The tracks from the different planes are then combined to produce a 3-D spatial fit. A space point is defined as at least two adjacent cluster hits in the Y plane and one other plane of a particular chamber. If a space point is found then the track candidate is deemed to have caused a hit in this chamber.

Both field polarities of the run were used by TRIDENT to try to determine the exact positions of the wire planes. The shifts expected in the chamber positions are of the order of a few microns and are included for track reconstruction and momentum fitting.

Chapter 3

Reconstruction of V^0 and Cascade Decays

The central concern for WA85 has been the reconstruction of events with complex topologies such as V^0 and cascade decays. This chapter concentrates on the reconstruction of V^0s, namely Λs , $\overline{\Lambda}$s and K^0s , and cascades such as Ξ^-s . The main aim of the WA85 experiment was to study decays of this type in the difficult conditions of ultra-relativistic ion collisions. The detection of such decays in the environment of p-W interactions is less hampered by background. The data discussed in the proceeding pages will, for the main, be taken from level 2 events; the same cuts are applied to the level 1 set of V^0 and cascade data. The selection criteria that the above mentioned decays must fulfill will be discussed. In addition, the cuts performed on the negative non-strange particles taken from level 1 events will be reviewed.

3.1 V^0 Reconstruction and Identification

The Λ hyperon is studied *via* its decay $\Lambda \rightarrow \mathrm{p} + \pi^-$ ($\overline{\Lambda} \rightarrow \bar{p} + \pi^+$) and K^0 *via* its two pion decay channel, $K^0 \rightarrow \pi^+ + \pi^-$. The signature for a V^0 decay is, therefore, one of oppositely charged tracks that intercept at a point

well removed from the target. A schematic diagram of a possible V^0 decay is shown in figure 3.1.

Using data which has been processed by TRIDENT a program known as STRIPV0 searches for V^0 candidates. STRIPV0 rejects events which cannot possibly be V^0 candidates on the basis of the following set of loose cuts.

- STRIPV0 looks for a combination of two tracks of the opposite charge which have a distance of closest approach of less than 2 cm.

- The vertex position is the midpoint of the line joining the two tracks at their closest approach. The x coordinate of this vertex is required to lie in the range $-15 < x < 90$ cm. The lower limit is chosen because at this point the acceptance is found to substantially reduce, see section 3.1.1, and the contamination from background is higher. In addition, as the V^0 vertex position approaches the target its value is detemined with less accuracy due to extrapolation errors. The upper limit is the position of the first A chamber.

- The transverse momentum of the decay tracks with respect to the line of flight of the V^0 is defined as q_T, and this must be less than 0.4 GeV/c. Real V^0 decay tracks have a q_T of at most 0.2 GeV/c, so this helps reduce combinatorial background.

As can be seen in figure 3.2 the effective mass M($p\pi^-$) and M($\overline{p}\pi^+$) of the V^0 candidates already show a clear peak at the Λ mass of 1.116 GeV [58], with these preliminary cuts.

The events which pass STRIPV0's criteria are written to DST. They are then processed by a further program whose purpose is to perform tighter, final cuts, defining whether a 'good' Λ , $\overline{\Lambda}$ or K^0 has been detected. The cuts used to perform successful reconstructions are described in section 3.1.1 and summarized in section 3.1.2. A sample of Monte Carlo generated Λs were used as an aid to the study.

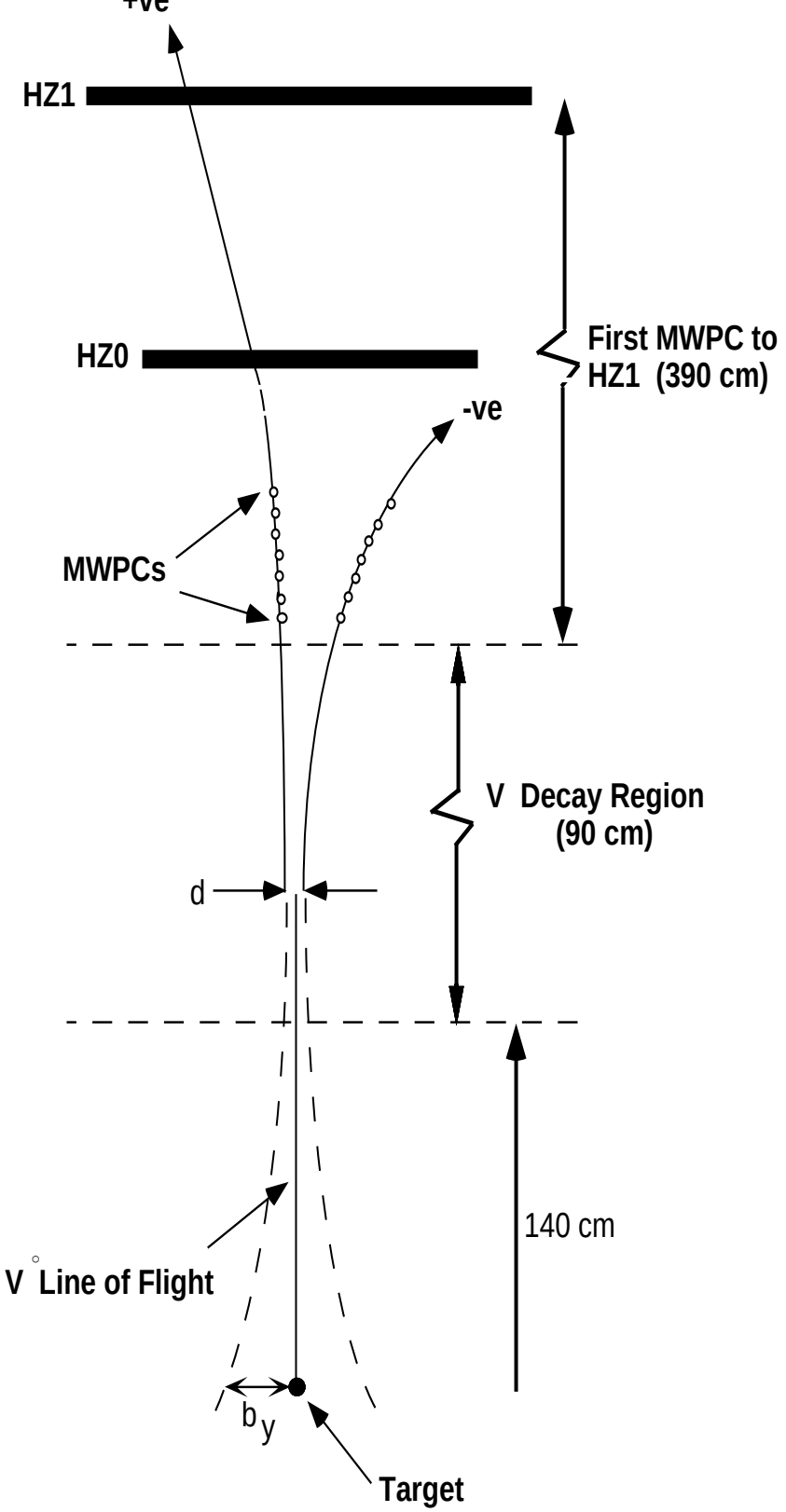

Figure 3.1: Schematic illustration of a V^0 decay; the geometric parameters of such a decay are shown.

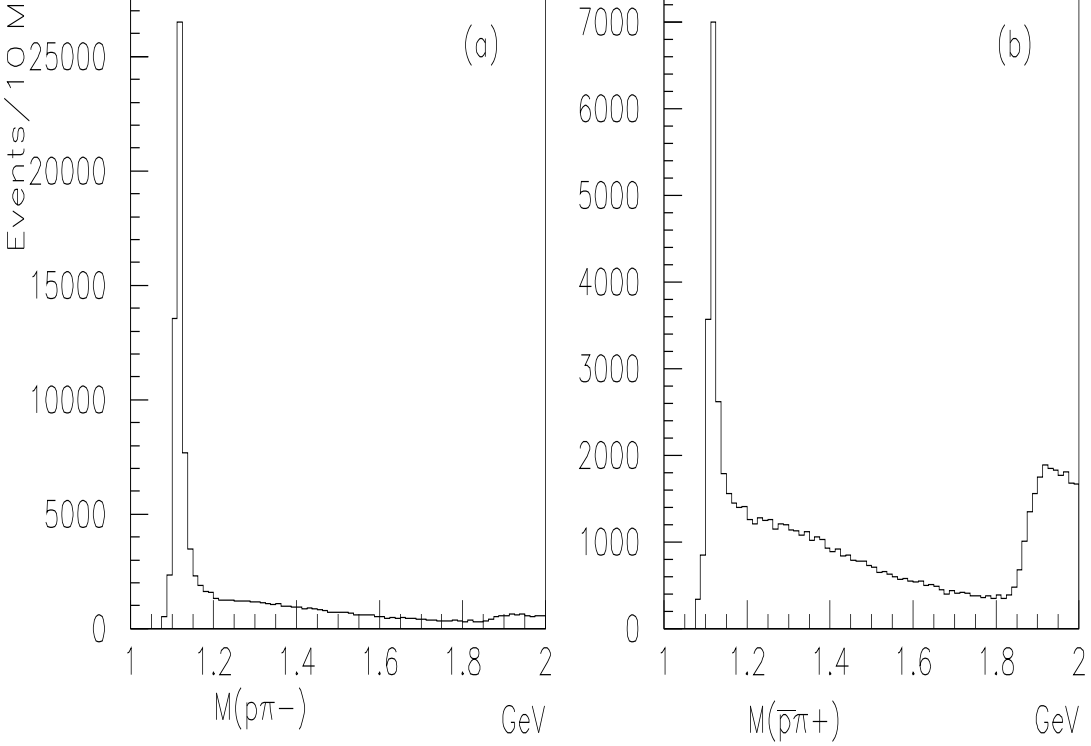

Figure 3.2: STRIPV0 Effective mass of V^0 when fitted to (a) M(pπ^-); and (b) M($\bar{p}\pi^+$).

3.1.1 Final Reconstruction Criteria for Λs and K^0s

Firstly, it is required that each decay track should have at least four space points in the seven A chambers; this ensures that the tracks are well defined in terms of momentum. In addition, both decay tracks are required to trace through all seven MWPCs with a 1 cm edge gap around the interior of each chamber, which helps reduce systematics, see section 4.1.3. In addition, at least one decay track must trace through corresponding halves, RIGHT-RIGHT or LEFT-LEFT, of both hodoscopes as requested by the trigger. This condition standardizes the acceptance region of the apparatus and only reduces the data set by 3% for Λs and by 5% for K^0s .

The acceptance of any particle considered for reconstruction is essentially determined by the geometry of the MWPCs. Figure 3.3 (a) shows the x-position distribution of the decay vertex for a set of Monte Carlo Λs after the above cuts have been applied. It demonstrates the reduction in acceptance with increased distance upstream from the first A chamber. A cut on the vertex position which accepts Λs in the range of $0 < x < 90$ cm will further

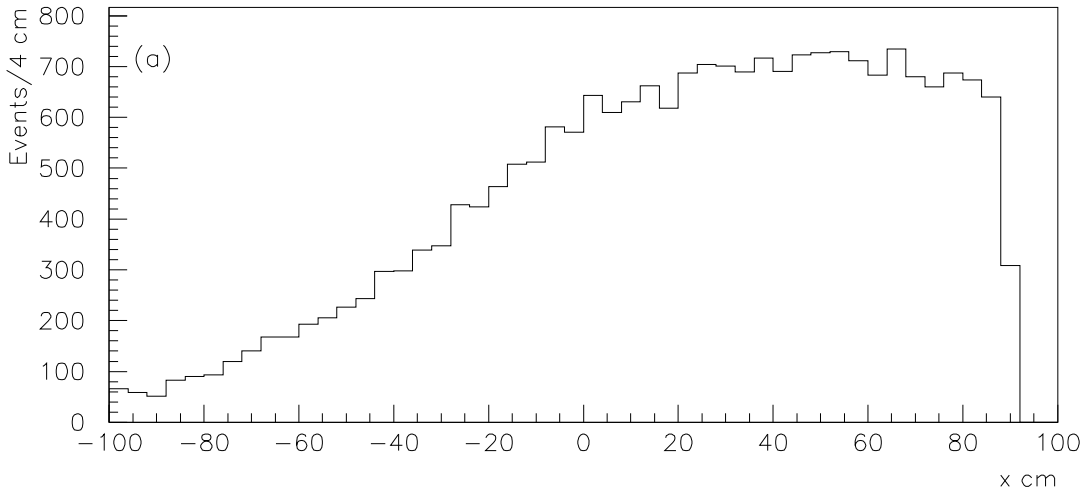

Figure 3.3: Distribution of vertex in x for (a) Monte Carlo Λs after initial geometrical cuts have been applied; and (b) real V^0 s projected upon an effective mass fit of M(pπ^-).

reduce the background produced by paths of oppositely charged tracks from the target, crossing and producing fake Λ candidates. Figure 3.3 (b) shows the distribution of the vertex of the real V^0 candidates against the effective mass, M($p\pi^-$). The loss of candidates is not negligible in the region below 0 cm in x, but this cut increases the good V^0 to background ratio. The vertex treatment for the K^0 candidates is slightly more complex and will be dealt with later in this section. The acceptance limits the minimum momentum of the V^0 candidates that are considered. In figure 3.4 the total momentum for the V^0 particles, after cuts 1-6 (see section 3.1.2) have been applied is shown. In this case the momentum cut of 6.5 GeV/c was not applied, which is the usual procedure when considering the effect of cuts on a particular

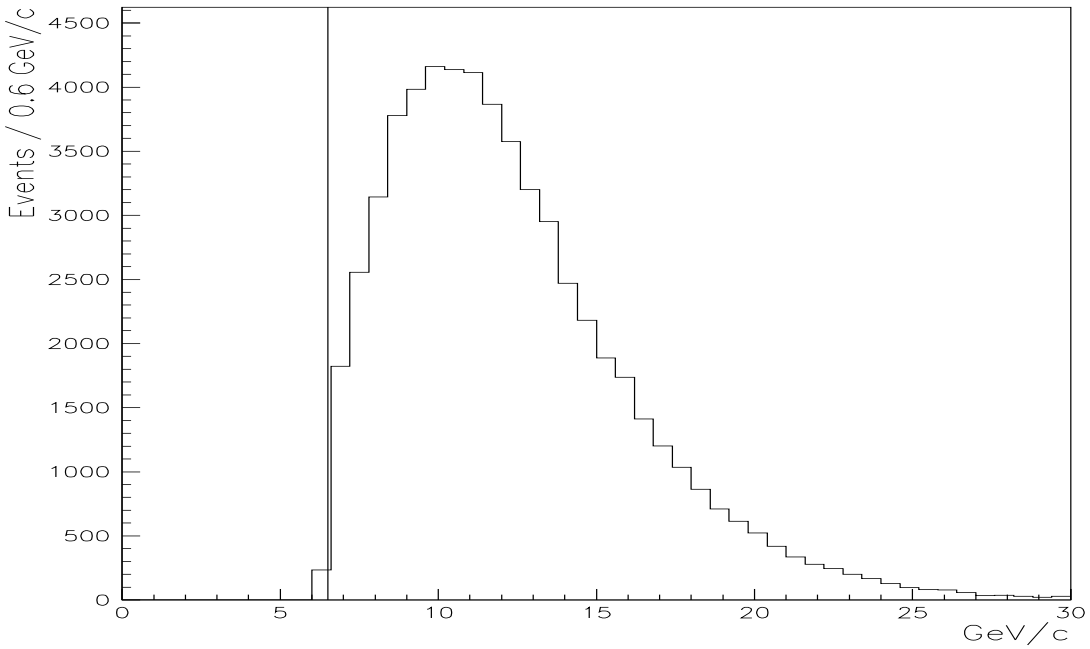

Figure 3.4: Momentum of V^0 after cuts; the cut of momentum $\geq$ 6.5 GeV/c is shown.

parameter.

Figure 3.5 shows the distribution of *CLOSE*, half the distance of closest approach of the two tracks of opposite charge. *CLOSE* is required to be less than 0.5 cm. Nearly all the candidates remain within the accepted region after cuts 1 - 7 and 8 or 13 have been made. V^0s produced at the target will point back to the target position. Figure 3.6 shows the distribution of the *ANGLE* between the sum of the three-momenta of the V^0 decay tracks and line of flight of the V^0 from the centre of the target. Again it is noticeable that most candidates are accepted after the *ANGLE* cut of less than 0.75^o is made, when the cuts of 1 - 7 and 8 or 13 are applied.

Impact parameter, y_{V^0}

As already mentioned, most of the V^0 background is due to tracks which originate from the target. The paths of real V^0 decay tracks will, in general, cross each other twice in the bend plane of the magnetic field. One of the crossings will be the real decay vertex and the other will be due to the tracks crossing again some distance upstream or downstream from the former vertex. It is found that the maximum distance between these crossing points

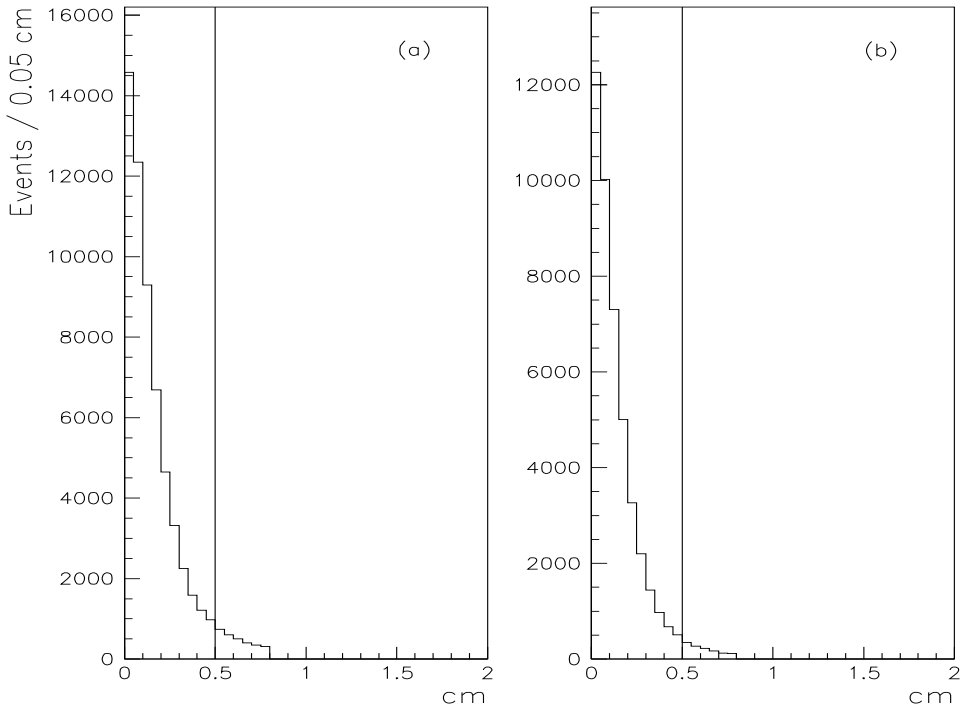

Figure 3.5: Distribution of $CLOSE$ for V^0 s (a) before cuts; and (b) after cuts. The cut of $CLOSE \leq 0.5$ cm is shown.

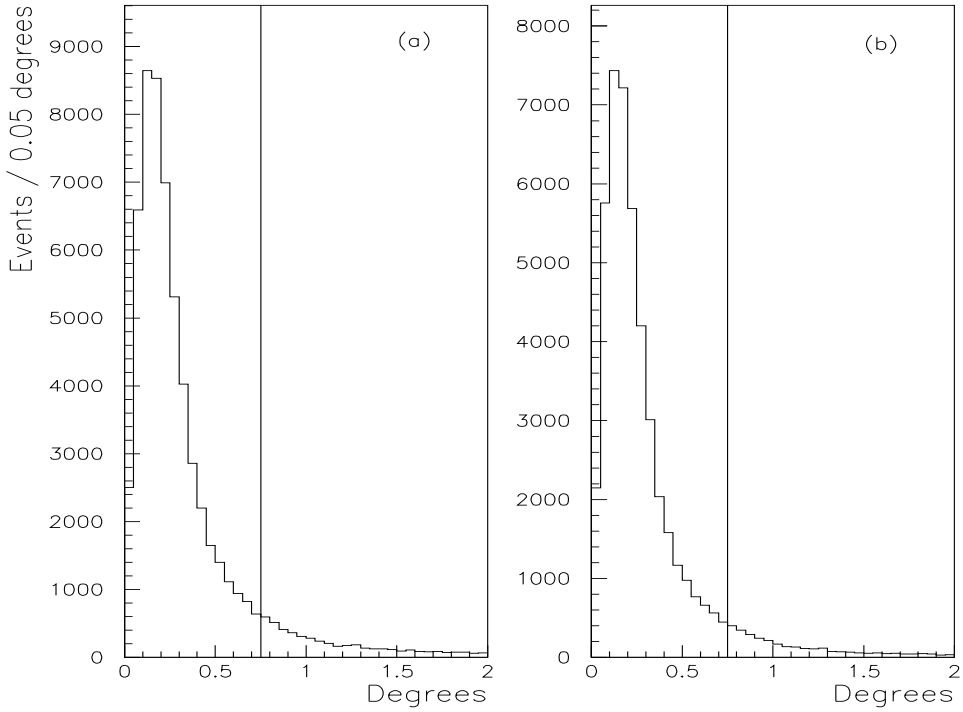

Figure 3.6: Distribution of $ANGLE$ for V^0s (a) before cuts; and (b) after cuts. The cut of $ANGLE \leq 0.75$ degrees is shown.

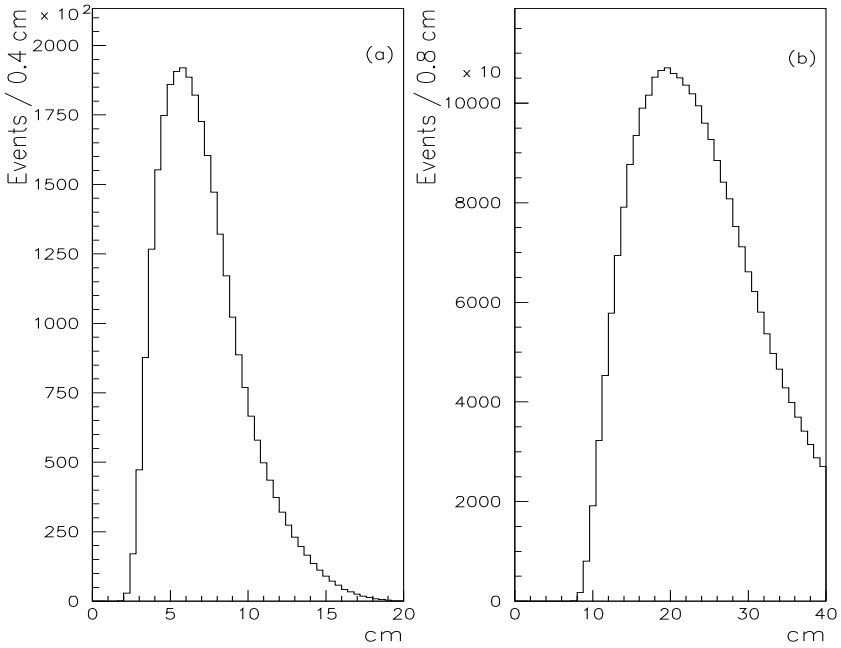

Figure 3.7: Distribution of y_{V^0} for 'clean' Monte Carlo Λ events for (a) the proton; and (b) the pion.

does not depend on the V^0 momentum, but on the decay tracks' momenta in the centre of mass frame, p^*, and the magnetic field strength. So, in a fixed magnetic field the maximum distance between the crossing points of the decay tracks is constant for a specific V^0 decay.

For Λs, it is found that this maximum distance is $\sim$ 40 cm and for K^0s $\sim$ 80 cm[1]. The impact parameter, y_{V^0}, is defined as the distance in the bend direction of the magnetic field, between the track intersection with the target plane and the centre of the target. Since the region in which Λ decays are accepted is at least 140 cm from the target the two tracks cannot trace back to the target. This is illustrated in figure 3.7 where the y_{V^0} distribution for the decay tracks of 'clean' Monte Carlo Λ decays, *i.e.* with no background implanted into the event, is shown.

Figures 3.8 (a) and (b) show the impact parameter distributions for the pion decay track for real V^0s seen as Λ decays before and after cuts 1 - 10 are applied respectively. Similarly figures (c) and (d) show the effect of such cuts on the proton decay track. The cuts remove the small amount of background

[1]see Appendix B for further discussion.

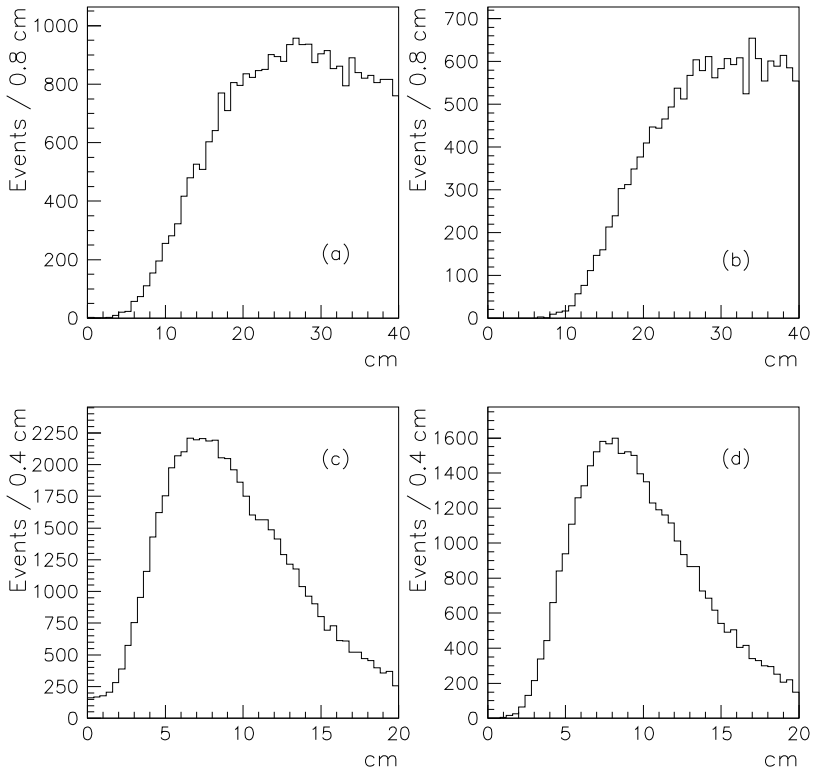

Figure 3.8: Distribution of y_{V^0} for (a) the pion before cuts; (b) the pion after cuts; (c) the proton before cuts; and (d) the proton after cuts.

due to tracks from the target. The distribution of y_{V^0} against the effective mass, M($p\pi^-$), of the STRIPV0 candidates for positive and negative tracks is shown in figures 3.9 (a) and (b) respectively. This plot further illustrates the background noise before impact parameter cuts are made.

The Robust Method vertex cut used for K^0s

It has been shown that the separation of the two crossing points in a K^0 decay can be up to 80 cm. This large separation means that even greater care must, therefore, be taken in selecting such decays than in Λ decays. STRIPV0 provides the best fitted vertex in a V^0 type event by minimizing the distance between the two tracks. However, if the real vertex corresponds to the crossing which is furthest removed from the A chambers its position will be determined with less accuracy than the other crossing due to extrapolation errors and so is less likely to be fitted as well as the 'fake' vertex. It is

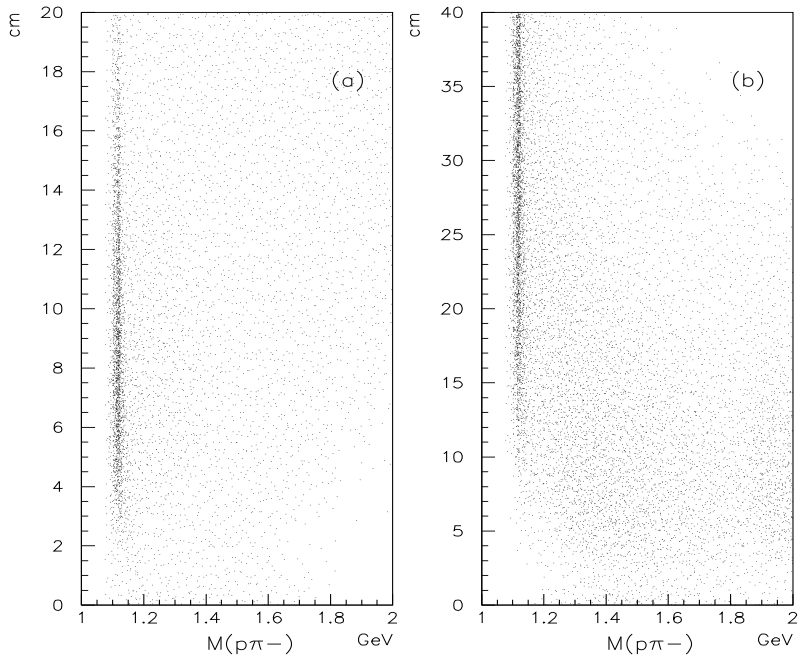

Figure 3.9: Distribution of target impact parameters projected onto the effective mass M($p\pi^-$) for (a) positive STRIPV0 tracks; and (b) negative STRIPV0 tracks.

therefore required that both vertices must be found within a certain fiducial region. This ensures that they will both be well determined and that it does not matter which vertex is the real one. The method employed is as follows: Using the STRIPV0 vertex and parameterizing the two decay tracks by circles in the x-y bend plane, the other crossing can be found in this plane, where the best resolution exists. If both crossings lie within the fiducial region defined as $-15 \leq x \leq 90$ cm the event is accepted, as illustrated in figure 3.10. This region corresponds to 105 cm in length, greater than the 80 cm maximum separation and was found to reduce the data sample by approximately half compared with requesting that only the best vertex found by STRIPV0 has to lie in the fiducial cut region. In addition, this method reduces the background, because the two decay tracks cannot now come from the target. Figure 3.11 shows the distance between the two crossings plotted against the STRIPV0 'best vertex'. The plot illustrates that the crossings are generally separated by about 60 cm to 80 cm and the acceptance requires

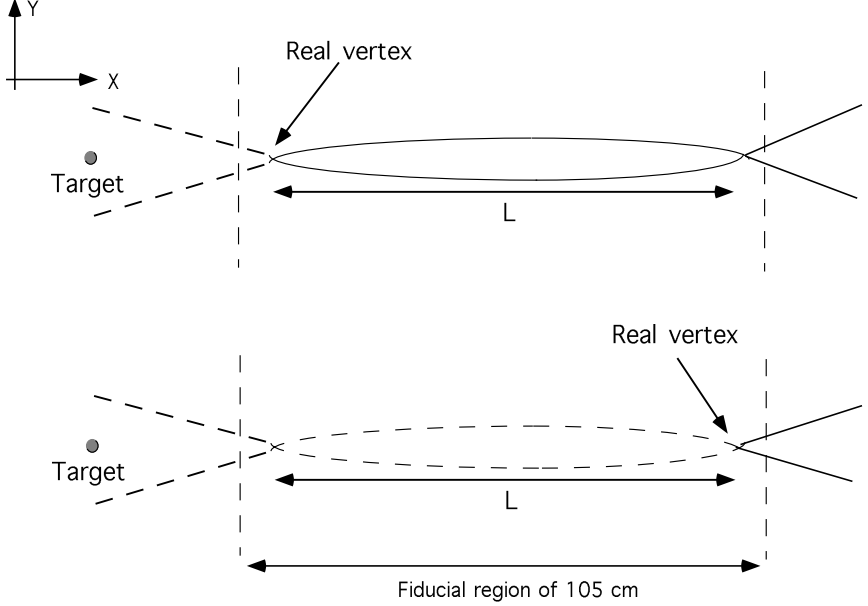

Figure 3.10: Schematic showing the K^0 passing the Robust Method criteria, used to define 'good' K^0 candidates and to reduce background. The two possible decay geometries are shown. In the top figure the V^0 decays and the decay tracks cross again, whereas in the bottom figure the decay tracks can be traced back to an earlier crossing point than that of the real vertex .

that the STRIPV0 'best vertex' must lie either close to the A chambers or about 80 cm from them.

The Podolanski-Armenteros Variable α

The quality of the V^0 candidates that have passed the above cuts can be assessed by considering their distribution on the Podolanski-Armenteros plot [59]. Components of the V^0 decay particles three-momenta are resolved to define the variable α which is given by

$$\alpha = \frac{q_L^+ - q_L^-}{q_L^+ + q_L^-}$$

where q_L^+ and q_L^- are the momentum components parallel to the direction of the V^0 for positive and negative tracks respectively. This variable is used to describe the asymmetry of a decay by considering its distribution with q_T. Further discussion of the α quantity and its relation to q_T for different decays is given in Appendix C. The Podolanski-Armenteros plot for V^0s is shown in figure 3.12. The regions of allowed kinematic range for the various V^0 decays

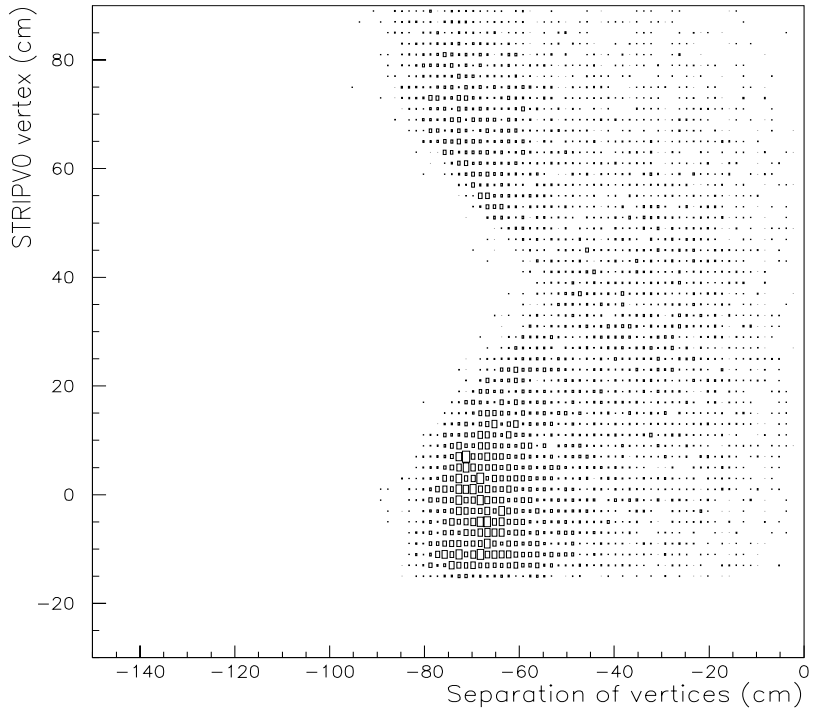

Figure 3.11: Distribution of STRIPV0 vertex versus the difference in the two vertices found using the robust method for K^0s .

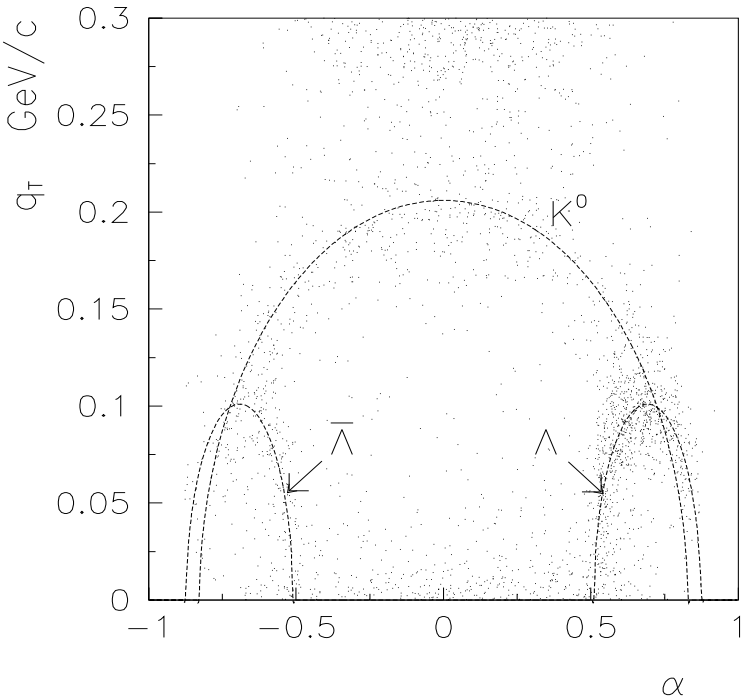

Figure 3.12: The Podolanski-Armenteros plot illustrating the loci of points along which genuine decays lie.

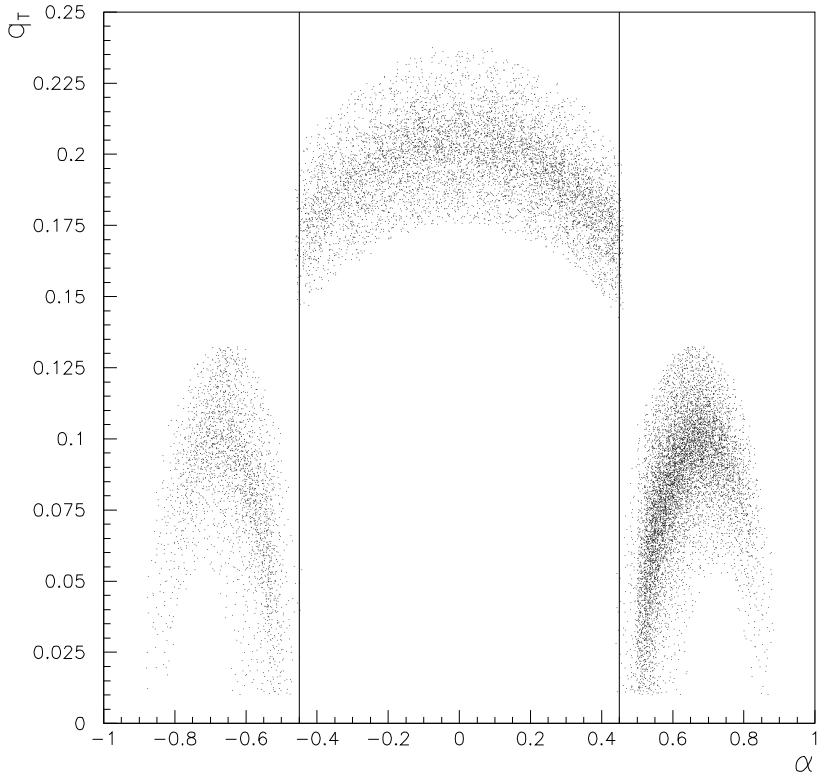

Figure 3.13: The Podolanski-Armenteros plot for Λ , $\overline{\Lambda}$ and K^0 candidates after cuts.

are defined by ellipses. The data shows a clear correlation between q_T and α for Λs, $\overline{\Lambda}$s and K^0s. Clusters are seen around these bands with relatively low background. The dark cloud at the top of the figure is due to tracks from the target combining to produce fake V^0s. A small amount of background due to e^+e^- pair production from γ conversions occurs at low q_T. This is removed by a cut of $q_T > 0.01$ GeV/c.

V^0s are accepted in the regions given by

- $\overline{\Lambda}$s $\cdots \alpha < -0.45$;
- Λs $\cdots \alpha > 0.45$;
- K^0s $\cdots -0.45 < \alpha < 0.45$ [2].

Figure 3.13 shows the Podolanski-Armenteros plot for the Λ, $\overline{\Lambda}$ and K^0 candidates after all cuts have been applied. The ellipse which defines the

[2] the full kinematically allowed range of $\mid \alpha \mid$ for K^0s is approximately ≤ 0.83. However, the tighter cut is employed to remove Λ and $\overline{\Lambda}$ contamination from the K^0 sample.

region of K^0 decays partially overlaps that of the Λs and $\overline{\Lambda}$s , as was seen in figure 3.12. This contamination has been estimated to be about 4% for Λs and 17% for $\overline{\Lambda}$s .

To define a set of Λ and $\overline{\Lambda}$ candidates that are unambiguous in a specific kinematic region a further α cut is applied; it is given as

- Λs unambiguous $\cdots 0.45 < \alpha < 0.6$;
- $\overline{\Lambda}$s unambiguous $\cdots -0.45 > \alpha > -0.6$.

This cut in α is equivalent to a cut in $\cos\theta^* \leq -0.5$ [3]. It has been found that the ratio of $\Lambda/\overline{\Lambda}$ does not vary as a function of $\mid \alpha \mid$ up to the value of 0.6.

Further kinematic cuts

The region of kinematic acceptance will be discussed in detail in 5.1. Only reconstructed V^0 decays which lie in the kinematic region where the acceptance varies by no more than a factor of 10 from the maximum value used are considered. This is defined as the region of 'good' acceptance. Figure 3.14 (a) shows the distribution of rapidity versus transverse momentum of the Λ candidates with cuts 1 - 11 applied and figure 3.14 (b) is the equivalent distribution for the K^0s . Finally, a mass cut of 50 MeV centred on the Λ mass, *i.e.* $1.09 < M_\Lambda < 1.14$ GeV, is applied to the Λ and $\overline{\Lambda}$ candidates and a mass cut of 100 MeV centred on the K^0 mass, *i.e.* $0.45 < M_{K^0} < 0.55$ GeV, is applied to the K^0 candidates.

3.1.2 Summary of cuts used to identify V^0s

1. Each decay track has at least four space points ;
2. Each track traces through all seven MWPCs within 1 cm of the edge of the interior of each chamber ;

[3] the angle, θ^*, is defined as that between the line of flight of the V^0 and the decay of the (anti)proton in the V^0 rest frame.

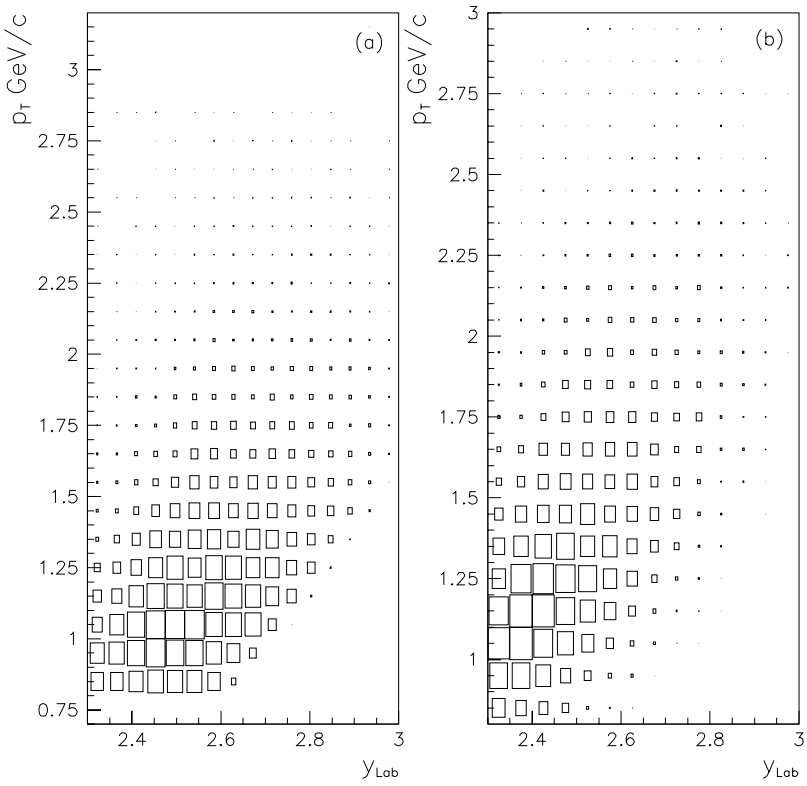

Figure 3.14: Distribution in $y_{lab} - p_T$ phase space of (a) Λ and $\overline{\Lambda}$ candidates; and (b) K^0 candidates after all cuts, except for the mass cut, have been applied.

3. The positive or negative decay tracks satisfies the level 1 trigger condition *i.e.* gives corresponding hits, RIGHT-RIGHT or LEFT-LEFT, in the two hodoscopes HZ0 and HZ1 ;

4. The V^0 must have a momentum of greater than 6.5 GeV/c ;

5. The positive and negative tracks of the V^0 are required to have a distance of closest approach of less than 1 cm ;

6. The angle between the V^0s line of flight from the target and the sum of the three-momenta for the V^0 decay tracks is $< 0.75^o$, *i.e.* the candidate comes from the target ;

7. $q_T > 0.01$ GeV/c.

   Cuts Specific to Λ and $\overline{\Lambda}$ Candidates :

8. The x position of the Λ vertex lies in the decay region of at least 140 cm to 230 cm from the target ;

9. $y_{V^0} > 0.8$ for $p(\overline{p})$ and $y_{V^0} > 1.8$ for $\pi^-(\pi^+)$, from the $\Lambda(\overline{\Lambda})$ decay ;

10. Λs $\cdots \alpha > -0.45$, $\overline{\Lambda}$s $\cdots \alpha < -0.45$;

11. the effective mass is in the range,
$M_\Lambda - 25$ MeV $< M(p\pi^-) < M_\Lambda + 25$ MeV ;

12. Unambiguous Λs $\cdots 0.45 < \alpha < 0.6$, $\overline{\Lambda}$s $\cdots -0.45 > \alpha > -0.6$.

Cuts Specific to K^0 Candidates :

13. The two K^0 crossings (vertices) are within the fiducial region given by $-15 \leq x \leq 90$ cm ;

14. $-0.45 \leq \alpha \leq 0.45$;

15. the effective mass is in the range,
$M_{K^0} - 50$ MeV $< M(\pi^+\pi^-) < M_{K^0} + 50$ MeV.

Figure 3.15 shows effective mass distributions for the set of data interpreted as M($p\pi^-$) after cuts (a) 1 - 2 and 10, (b) 1 - 5 and 8, (c) 1 - 9, and (d) 1 - 10 have been applied. Similarly in figure 3.16 the data is interpreted as M($\pi^+\pi^-$) after cuts (a) from STRIPV0, (b) 1 - 2 and 13, (c) 1 - 5 and 13, (d) 1 - 7 and 13 - 14. Both illustrate clear peaks, with little background resolved at the appropriate masses.

In figure 3.17 the mass plots for the full statistics of (a) Λs and (b) $\overline{\Lambda}$s without the K^0 contamination cut 12 are shown along with (c) Λs , and (d) $\overline{\Lambda}$s where the cut has been applied. In addition, superimposed is the K^0 contamination around the Λ mass. This is determined by applying to the sample a cut of $q_T \geq 0.12$ GeV/c.

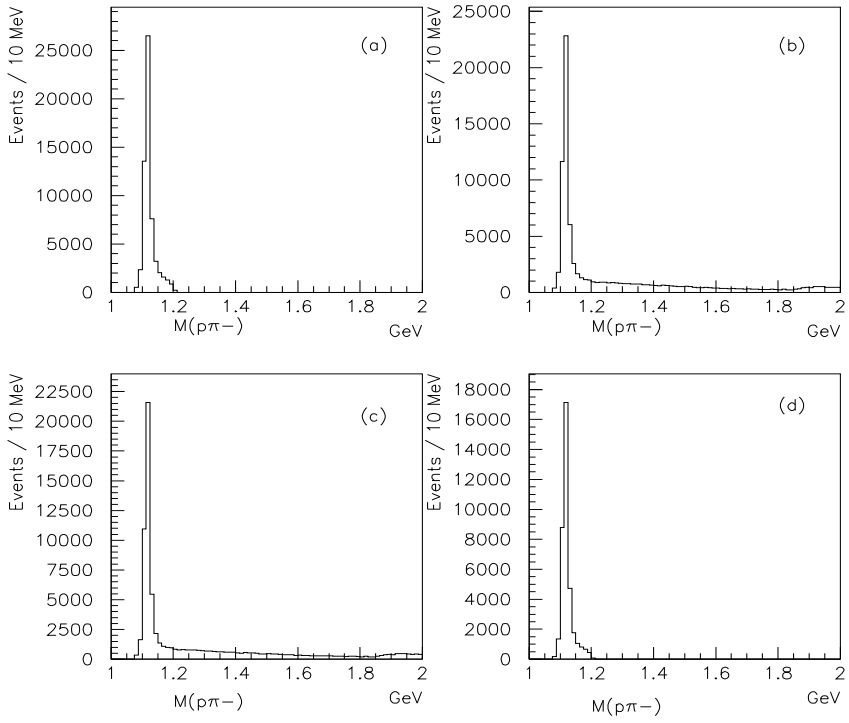

Figure 3.15: Effective mass distributions for Λ candidates with the application of various cuts: for cuts (a) 1 - 2 and 10; (b) 1 - 5 and 8; (c) 1 - 9; and (d) 1 - 10.

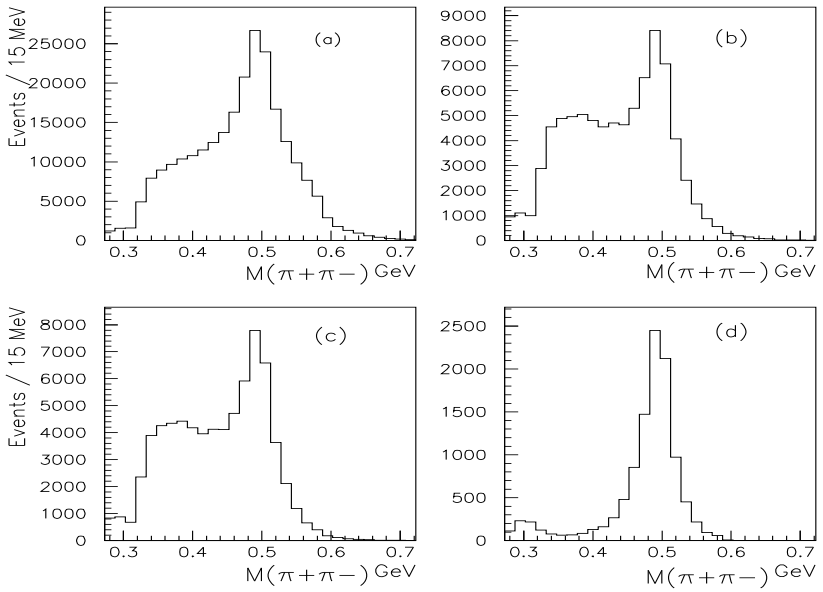

Figure 3.16: Effective mass distributions for K^0 candidates with the application of various cuts: for cuts (a) STRIPV0 defined (b) 1 - 2 and 13; (c) 1 - 5 and 13; (d) 1 - 7 and 13 - 14.

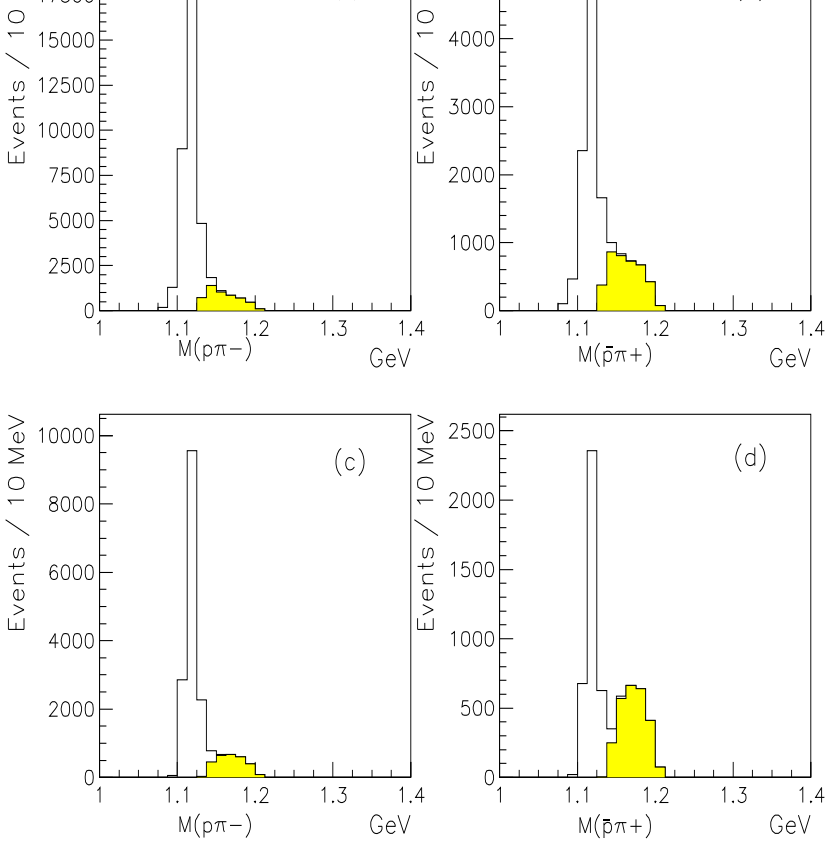

Figure 3.17: Effective mass distributions for Λ and $\overline{\Lambda}$ candidates after all cuts.

3.1.3 Λ and $\overline{\Lambda}$ Raw Yields

The number of reconstructed Λ, $\overline{\Lambda}$ and K^0 decays for the level 1 and 2 data samples are shown in table 3.1. These represent candidates who have passed cuts 1 - 11, and then also cut 12 employed to remove K^0 contamination. It is noted that the data taken from the level 2 events arise from approximately 29 M triggers and the level 1 data from about 22 M triggers.

It must be noted that these numbers are uncorrected for cascade feed-down, where Λs ($\overline{\Lambda}$s) originate from Ξ ($\overline{\Xi}$) decays; this is treated in section 6.2. In addition, the acceptances, reconstruction efficiencies and the effect of the level 2 losses must be included to compare the production rates of different particle types.

Table 3.1: Full statistics for Λs, $\overline{\Lambda}$s and K^0s for both field polarities in the case of level 2 and level 1 data.

Particle Type	α cut	Trigger Level	Field $\downarrow$	Field $\uparrow$
Λ	≥ 0.45	Level 2	17,437	13,677
Λ	0.45 to 0.6		7,878	5,963
$\overline{\Lambda}$	≤ -0.45		4,901	3,814
$\overline{\Lambda}$	-0.6 to -0.45		1,906	1,561
Λ	≥ 0.45	Level 1	1,273	1,355
Λ	0.45 to 0.6		566	588
$\overline{\Lambda}$	≤ -0.45		349	393
$\overline{\Lambda}$	-0.6 to -0.45		149	155
K^0	-0.45 to 0.45	Level 2	4,814	3,723
K^0	-0.45 to 0.45	Level 1	374	307

3.2 Ξ^- Reconstruction and Selection

Ξ^- and $\overline{\Xi^-}$ cascades are identified by their decay mode

$$\Xi^- \rightarrow \Lambda + \pi^-,$$

$$\overline{\Xi^-} \rightarrow \overline{\Lambda} + \pi^+.$$

The selection criteria used in a search for these decays involves the identification of a potential V^0 decay and an additional track. The events which have passed the STRIPV0 cuts are unbiased to such conditions and are passed to a further program called STRIPXI. This program searches for the intersection of a negatively (positively) charged track with the line of flight of a Λ ($\overline{\Lambda}$). A schematic diagram illustrating the form of a Ξ^- decay is shown in figure 3.18.

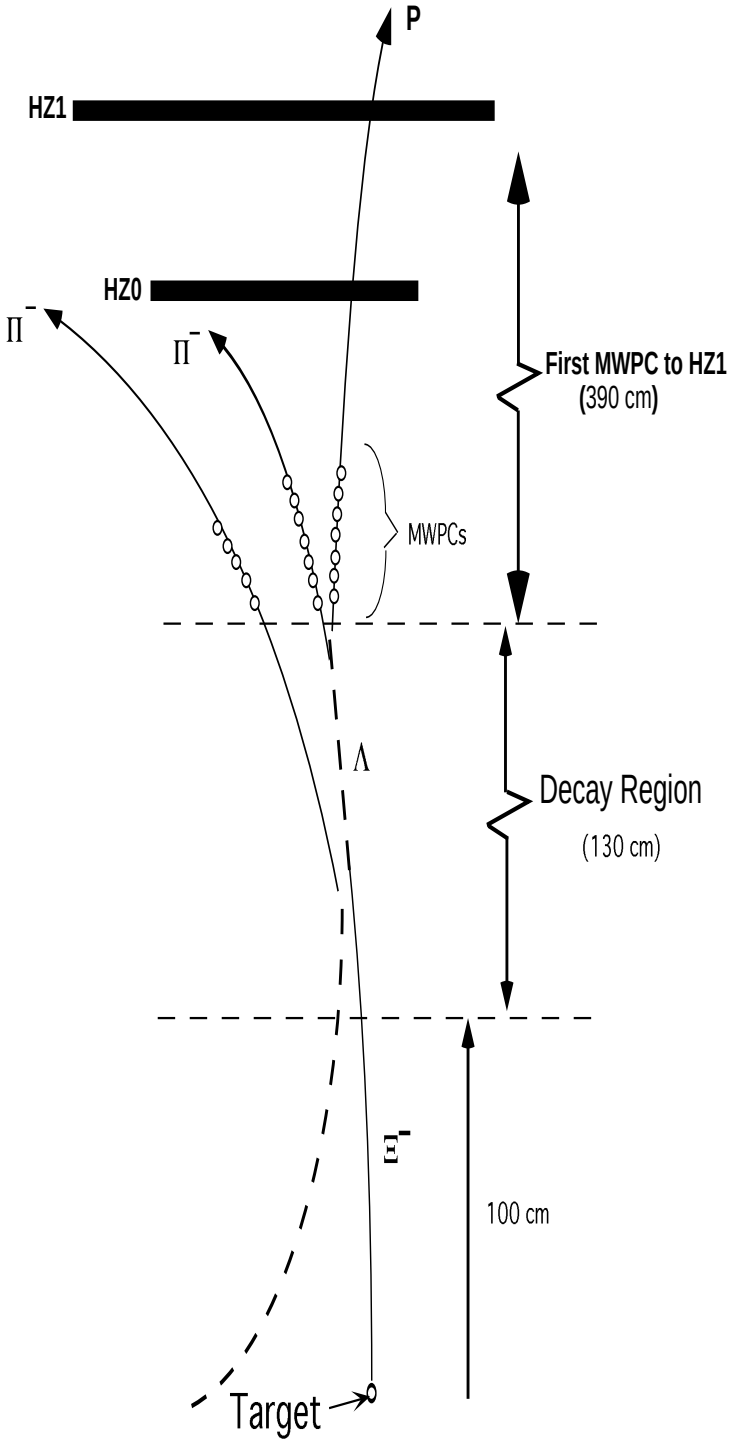

Figure 3.18: Schematic illustration of a cascade decay; the geometric parameters are illustrated.

STRIPXI requires some preliminary loose cuts on the V^0 candidate :

1. $|\alpha| \geq 0.4$;
2. and the effective Λ ($\overline{\Lambda}$) mass must be in the range of $M_\Lambda \pm$ 40 MeV.

The potential cascade candidates are passed to a final analysis program if the intersection of the V^0 and 'additional' track are traced to within 3 cm of each other and the cascade vertex lies in the region of $-50 \leq x \leq 90$ cm.

3.2.1 Final Ξ^- Selection Criteria

The selection is now tightened by the final analysis program. As in the case of the Λ analysis, the three potential Ξ^- decay tracks are required to have at least 4 space points. To define the acceptance they must each trace through the first four A chambers with the 1 cm edge gap and either the p or π^- from the Λ decay must satisfy the level 1 hodoscope condition. The π^- from the Ξ^- decay will reach the hodoscope planes less than 1% of the time. The final selection criteria for the V^0 candidates from a potential cascade decay are slightly relaxed in comparison to the Λ sample and are reviewed below :

- the vertex lies in the region $-15 \leq x \leq 90$ cm ;
- the distance of closest approach of the V^0 decay tracks is not larger than 1.6 cm ;
- the decay tracks have $q_T \leq 0.14$ GeV/c.

The condition that the V^0 points back to the target is not required for the cascade selection.

The cuts upon the Ξ^- are now considered. In figure 3.19 (a) is shown the distribution of the x coordinate of generated Monte Carlo Ξ^- vertices

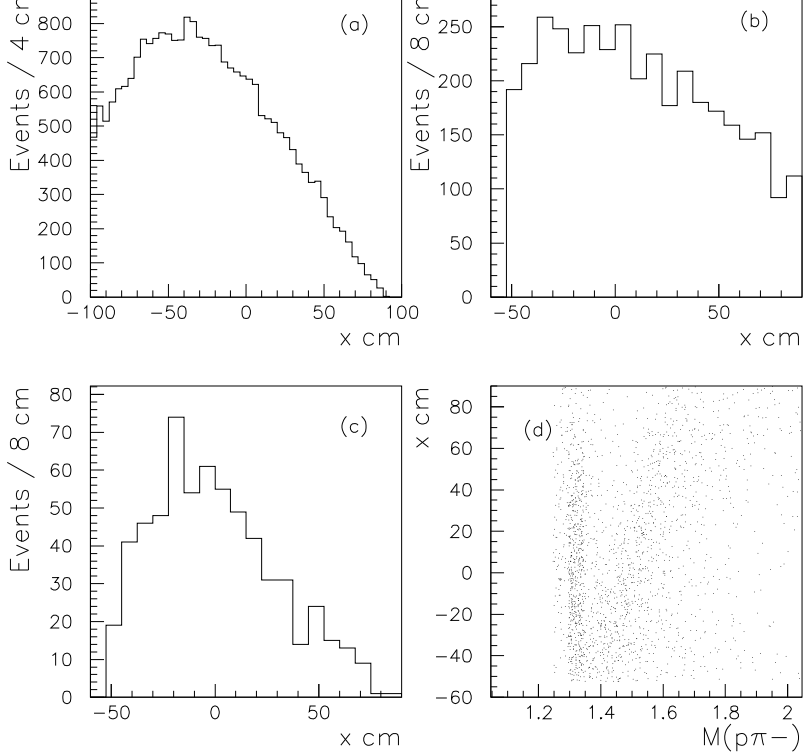

Figure 3.19: Distribution of vertices in x for (a) Monte Carlo Ξ^-s whose decay tracks have traced through chambers A1 and A4 and have satisfied the hodoscope condition; (b) real STRIPXI Ξ^- candidates; (c) real Ξ^- candidates after all other cuts have been applied; and (d) STRIPXI Ξ^- candidates plotted against the effective mass M(Λ π^-).

after the chamber and hodoscope requirements have been satisfied. The acceptance of Ξ^-s starts to fall when the distance between the decay vertex and the A chambers becomes sufficiently large. It is also noted that the vertex determination in x decreases in accuracy as this distance increases. In figure 3.19 (b) the vertex distribution for real raw Ξ^- candidates after STRIPXI and (c) after all other cuts have been made, are shown. Due to the acceptance fall off and to reduce background a cut of $-40 \leq x \leq 90$ cm is applied to the Ξ^- vertex position. This background reduction is illustrated by figure 3.19 (d) where the vertex is plotted as a function of the effective mass M(Λ π^-).

Figure 3.20 shows the distribution of $x_{V^0} - x_{\Xi^-}$, the distance between the Λ and Ξ^- vertices, for (a) STRIPXI data and (b) candidates which have survived all the other cuts. The cascade vertex should lie upstream of the Λ

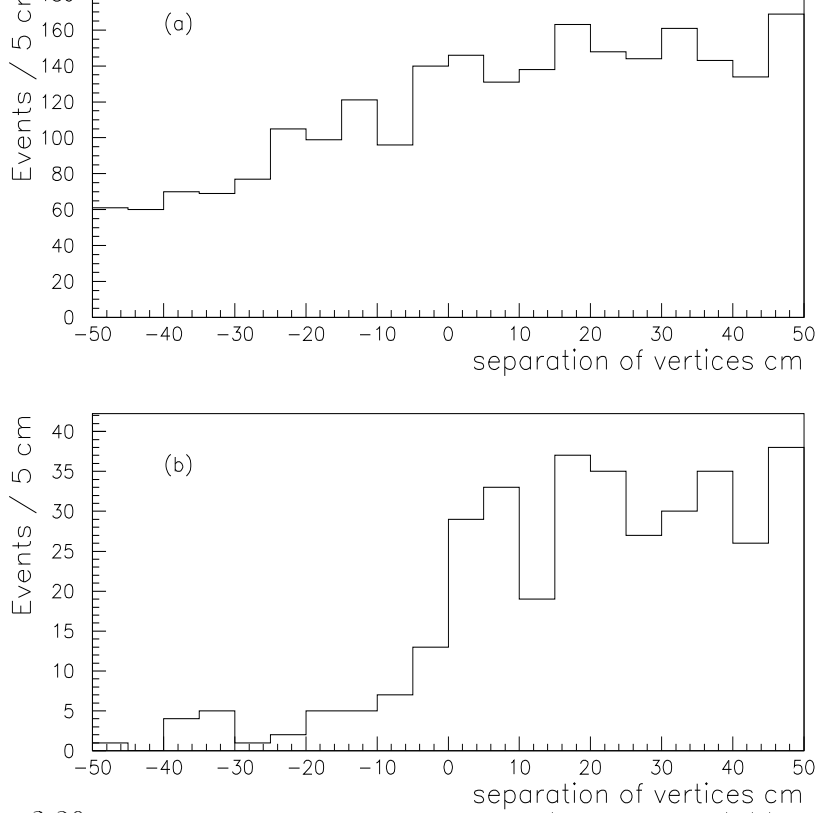

Figure 3.20: Distance between Λ and Ξ^- vertices (*i.e.* $x_{V^0} - x_{\Xi^-}$) (a) before cuts; (b) after all other cuts.

($\overline{\Lambda}$) vertex. The following causality cut is therefore applied

$$x_{V^0}\text{-}x_{\Xi^-} \geq 0\text{cm}.$$

However, smearing of the vertex positions of Ξ^- candidates (and their associated V^0 decays) will result in a small loss of genuine Ξ^- particles. The effect of this cut is accounted for in the reconstruction efficiency calculation discussed in section 5.2.3.

Figure 3.21 shows the distribution of *CLOSXI*, which is half the distance of the closest approach of the charged track and V^0 decay, for (a) STRIPXI candidates and (b) for all other cuts; the cut is chosen at 1.0 cm.

The Ξ^- candidates must originate in the target, so they are traced back to the target plane. The distribution of the impact at the target plane in the bend direction of the magnetic field, y_Ξ, versus the effective mass M($\Lambda\ \pi^-$) is shown in figure 3.22 (a) for STRIPXI data. There is a strong correlation of Ξ^- candidates to the target region. In figure (b) the distribution of y_Ξ is plotted when all other cuts have been applied.

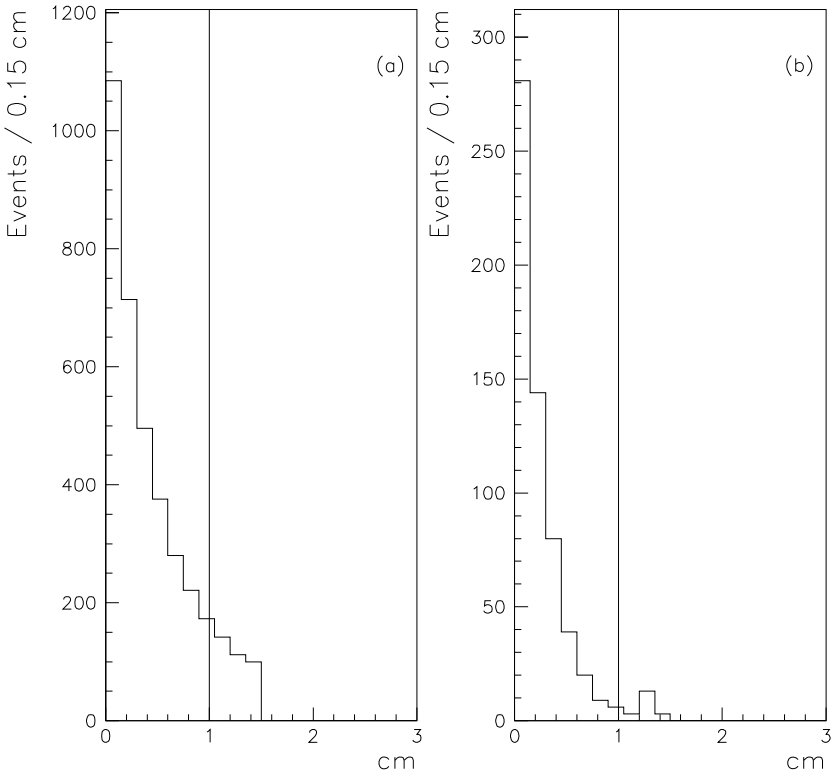

Figure 3.21: Distribution of *CLOSXI*; the cut of $CLOSXI \leq 1.0$ cm is shown.

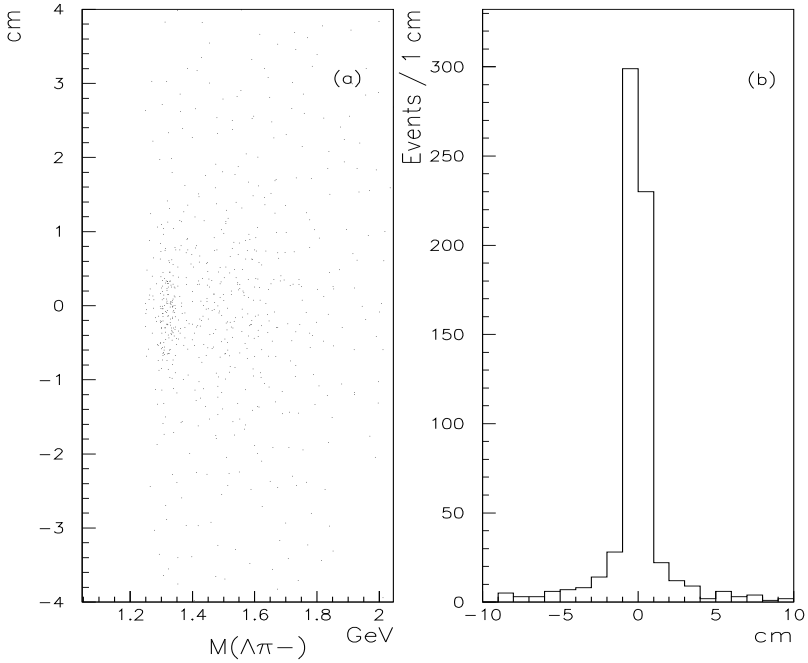

Figure 3.22: (a) The projection of y_Ξ on the effective mass M($\Lambda\ \pi^-$); and (b) y_Ξ after all other cuts have been applied.

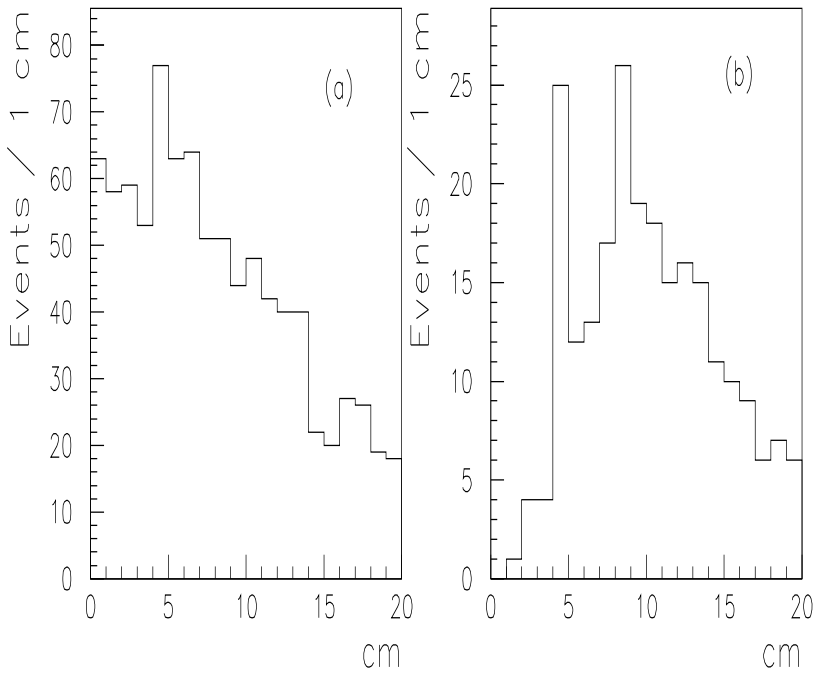

Figure 3.23: y_π distributions.

To reduce background from spurious charged tracks intercepting V^0 candidates the impact parameter of the π^-, y_π, from the Ξ^- decay is considered. A π^- from a genuine Ξ^- decay does not come from the target, however some π^-s may intercept the target position by chance. Figure 3.23 shows the y_π distribution for the π^- (a) for STRIPXI data and (b) with all other cuts applied to the sample. A cut of $|y_\pi| \geq 6$ cm is made on the cascade sample and as is seen in the previous figure removes some of the background. Indeed this cut reduces the sample by about 10% and the effect of this cut on the real Ξ^- data is accounted for in the acceptance calculation, see section 5.1.2.

To illustrate the application of various cuts upon the cascade data, figure 3.24 shows the distribution of the effective mass M_Ξ after various selection criteria have been applied. As illustrated by figure 3.25, Ξ^-s are considered if they lie, essentially, in the region of $2.3 \leq y_{lab} \leq 3.0$ and $1.2 \leq p_T \leq 2.9$ GeV/c. The final mass distributions are given in figure 3.26 and show clear peaks at M_Ξ. Ξ^-s and $\overline{\Xi^-}$s are chosen in the mass range of $M_\Xi \pm$ 50 MeV, where M_Ξ is given as 1321 MeV [58].

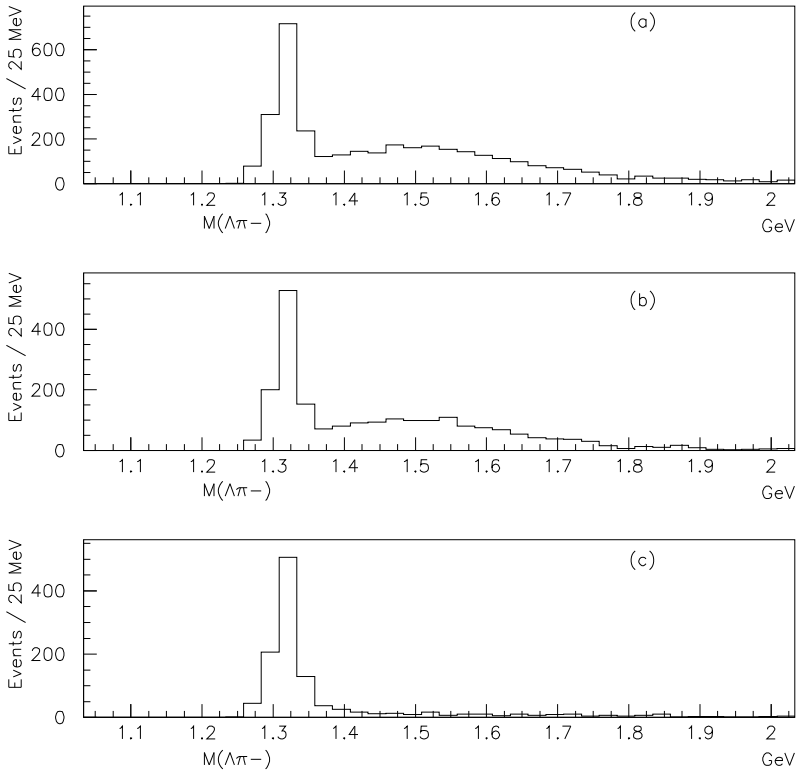

Figure 3.24: Cascade effective mass distributions interpreted as $\Lambda\pi^-$ for (a) STRIPXI candidates; (b) after the Ξ^- target impact parameter cut *i.e.* $y_\Xi \leq 2.0$ cm and the Ξ^- vertex cut; and (c) after the π^- target impact parameter cut *i.e.* $y_\pi \geq 6.0$ cm and the Ξ^- vertex cut.

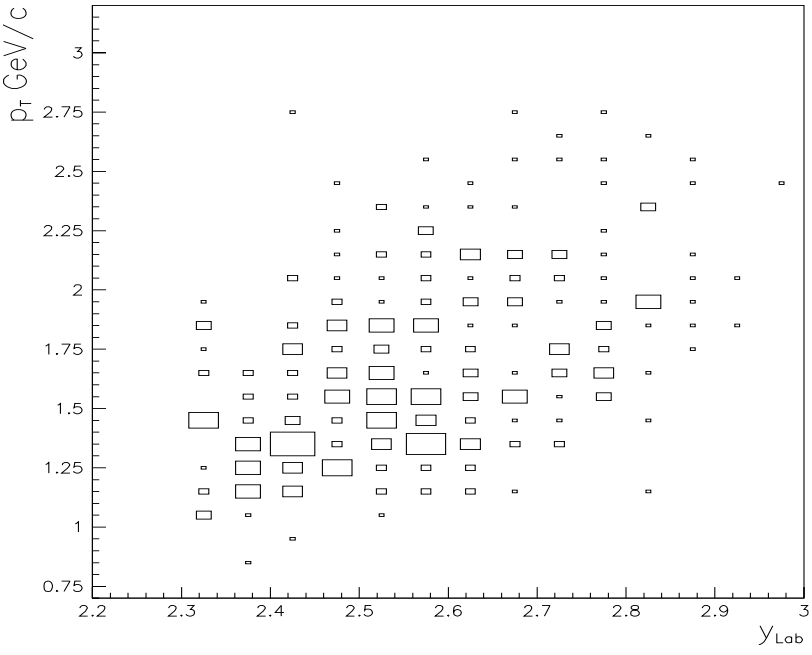

Figure 3.25: Region of good acceptance for Ξ^-s .

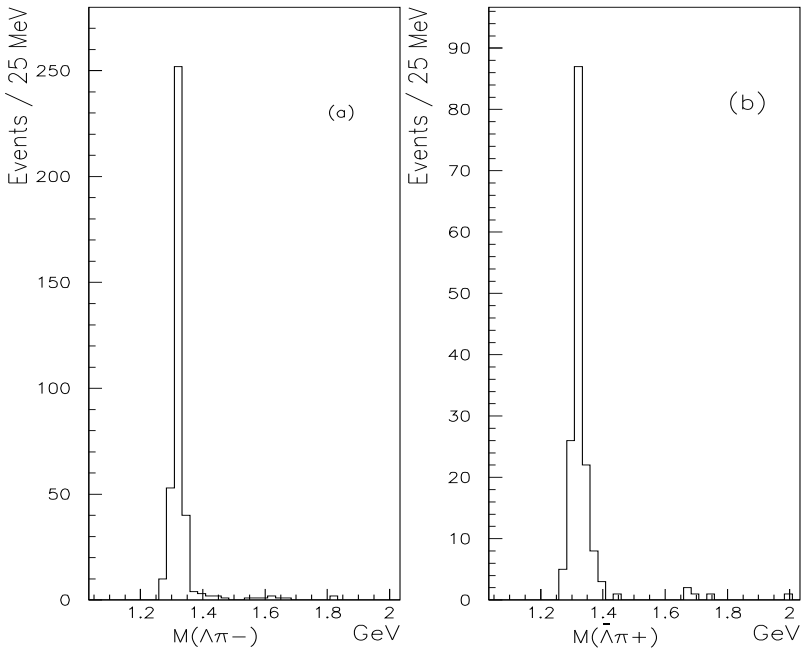

Figure 3.26: Effective mass distributions after all cuts for (a) M($\Lambda\ \pi^-$); and (b) M($\overline{\Lambda}\ \pi^+$).

3.2.2 Summary of cuts used to identify Cascades

1. Each decay track has at least four space points ;
2. each decay track traces through the first four MWPCs within 1 cm of the edge of the interior of each chamber ;
3. at least one of the Λ decay tracks must satisfy the level 1 hodoscope condition.

   Selection for V^0 candidate:

4. The distance of closest approach of the positive and negative decay tracks at the V^0 vertex must be less than 1.6 cm ;
5. the V^0 vertex must lie in the region $-15 \leq x \leq 90$ cm,
6. $|\alpha| \geq 0.4$ and $q_T \leq 0.14$ GeV/c ;
7. the effective mass of the V^0 candidate is $M_\Lambda \pm$ 40 MeV.

Selection for Ξ candidate:

8. The distance of closest approach of the decay π and V^0 must be less than 2.0 cm ;
9. the separation of the decay vertices is $x_{V^0} - x_{\Xi} \geq 0$ cm ;
10. the Ξ decay vertex lies in the range $-40 \leq x \leq 90$ cm ;
11. the cascade traces to the target, $y_{\Xi} \leq 2.0$ cm and the π from the cascade decay does not come from the target, $y_{\pi} \geq 6.0$ cm ;
12. the effective mass of the Ξ candidate is $M_{\Xi} \pm$ 50 MeV.

The final uncorrected selection yields 294 Ξ^-s and 136 $\overline{\Xi^-}$s for level 2 events which results in an uncorrected ratio of 0.46 $\pm$ 0.05. These findings are summarized in table 3.2 including the level 1 data. Again, as for all particle species the data must be corrected for acceptances and reconstruction efficiencies which will be discussed in chapters 4 and 5.

Table 3.2: Full statistics numbers for Ξ^-s and $\overline{\Xi^-}$s for both field polarities of the level 2 and level 1 cascade data.

Particle Type	Trigger Level	Field $\downarrow$	Field $\uparrow$
Ξ^-	Level 2	156	138
$\overline{\Xi^-}$		75	61
Ξ^-	Level 1	8	15
$\overline{\Xi^-}$		2	4

3.3 Negatives Study

In order to compare the production rates of hyperon decays with the yields of negative particles (h^-) [4] and to normalise the p-W data to the S-W data

[4] the $(h^-$s) are interpreted as π^-s.

a set of data, with only the level 1 stage of the trigger, was taken during the p-W run. These events were suitably unbiased, both towards strange decays and h^- production, unlike that of level 2 data. The nature of the tracking detectors used by WA85 means that direct particle identification is not possible. As has been discussed, in the case of particle decays selection criteria can be applied to determine if the decay is indeed a Λ decay, for example. This is not possible in the case of a π^-, so only the production of these particles rather than its positive conjugate partner is considered, due to the greater contamination which is expected in the case of the π^+ *i.e.* there are far more protons than anti-protons initially and the anti-protons are easily annihilated.

Selection Criteria for h^-s

The negatives analysis was based on approximately half a million triggers selected evenly throughout the run. These events yielded about 40,000 tracks satisfying the following conditions:

It is required that each h^- traces through the seven A chambers with the 1 cm edge gap and satisfies the hodoscope level 1 trigger condition as discussed previously. Each track must be reconstructed with at least four space points.

The negative tracks are traced to the target plane and their impacts upon this plane are considered. Figure 3.27 (a) and (b) show the individual component distributions plotted with the required target cuts superimposed. In figure 3.27 (c) the correlation in the Omega coordinates of the z and y impact parameters of the h^- at the target plane is displayed . It is noticeable that the h^-s are well centred on the target position at $y = 0$ cm and $z = -0.5$ cm. In figures 3.27 (b) and (c) the individual component distributions have been plotted with the required target cuts superimposed.

The transverse momentum and rapidity distributions are shown in figure 3.28 (a) and (b). It can be seen that the p_T distribution falls off at around 0.6

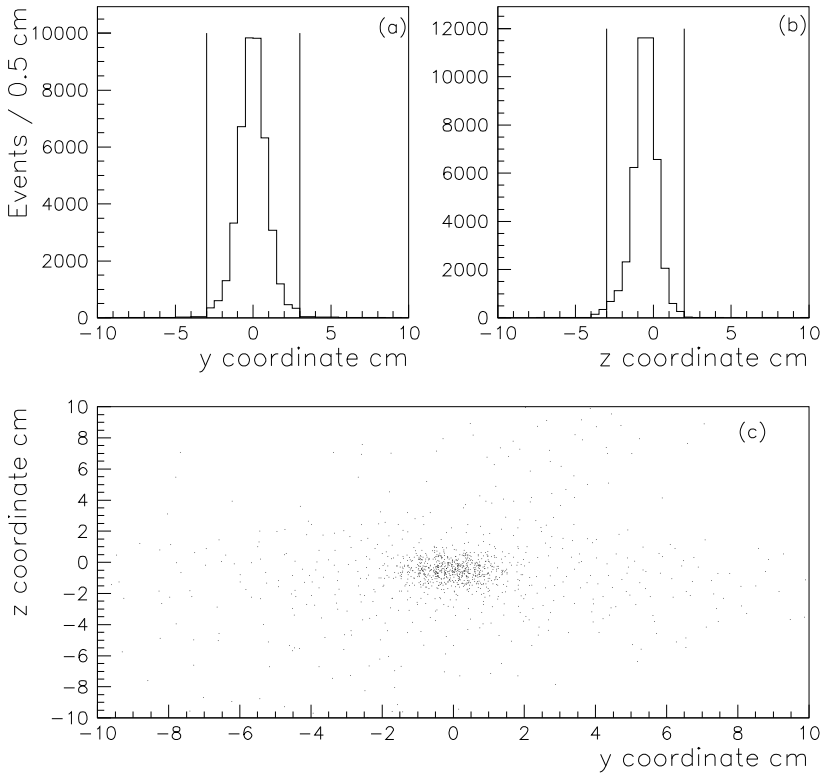

Figure 3.27: h^- impacts at the target plane; the impact parameter cuts are shown.

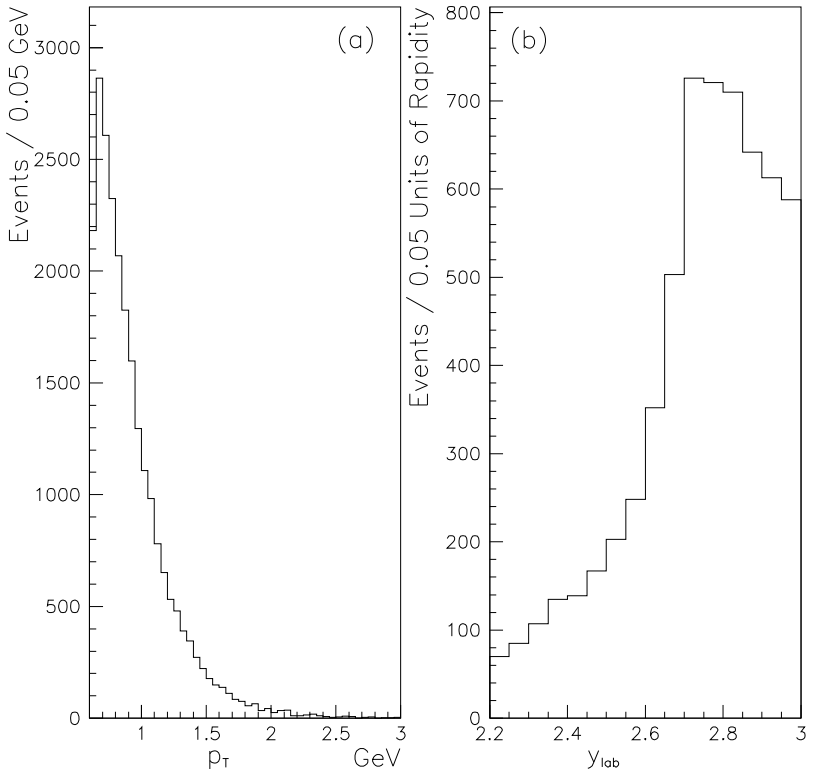

Figure 3.28: (a) Transverse momentum; and (b) rapidity spectra distributions for h^-s .

GeV/c, which is a reflection of the trigger constraint. The y_{lab} distribution is boosted towards the higher end of the acceptance range; this is an effect of the hodoscope tracing requirement.

3.4 Summary

The selection criteria for the above particles have been considered and must be treated for corrections in terms of the geometrical coverage and the efficiency of the experiment, as well as other systematic effects. These will be treated in the following chapters. It has been seen that there are sufficient statistics for the particles mentioned, specifically Λ and Ξ^- decays, to undertake a detailed comparison with the published S-W results.

Chapter 4

Chamber and Hodoscope Efficiencies

This chapter is concerned with the efficiency calculations for the seven MWPCs and two scintillator hodoscopes used in the 1990 proton run. These efficiencies serve as part of the calculation which determines the total yields of a particular particle. The method used to determine the production rates of different particle decays is a complex process involving numerous calculations and is examined in detail in chapter 5.

4.1 Electronic Efficiency of the Wire Chambers

Chamber efficiencies have been calculated using 400,000 level 1 events sampled evenly over the entire proton run. Data taken from the level 2 stage of the trigger cannot be used because, unlike that of level 1, it requires a multiplicity condition in the first four A chambers and is therefore biased.

4.1.1 Method of Efficiency Calculation

The efficiency for a given plane, U, V or Y, of a specific chamber has been found. Initially the TRIDENT level 1 sampled tape is stripped of its track information, the 'geometry block' added by TRIDENT, the headers are changed and the events are rewritten in EPIO format. The tape now resembles a raw data cartridge as produced in the run. TRIDENT is run on the tape with the chamber of interest 'disabled' from the track fitting process. This output is fed to a second program which identifies all the tracks in an event with a space point in each of the remaining six chambers, to provide as accurately measured a track as possible. Each track is traced to the U, V and Y wire planes of the chamber under consideration and the point of intersection in the Omega coordinate scheme is recorded. The program then unpacks the electronics block of that event, using the ROMULUS tree structure as discussed in section 2.6, to determine if there was a corresponding wire hit in the plane of intersection. It checks if the central wire of any cluster in that event is within 2 mm of the point of intersection of the plane and the track. If this criterion is fulfilled then the plane under consideration is deemed to have successfully detected the track. An example of the residual distribution between the points of intersection of a track on a particular plane and the centroid of the wire cluster is shown in figure 4.1.

4.1.2 Chamber Efficiency Results

To provide a sensitivity to variations in efficiency across the wire planes each chamber is divided into 4 logical quadrants as illustrated in figure 4.2. The efficiency per quadrant is defined as the number of successful detections divided by the total number of tracks traced to that quadrant. If a larger set of smaller regions had been used to increase sensitivity then the statistics would have to be increased and the number of calculated efficiencies could

Figure 4.1: Plot of residual distribution for a typical wire plane (plane Y, chamber 3); note that the full width half maximum is about the order of the wire separation.

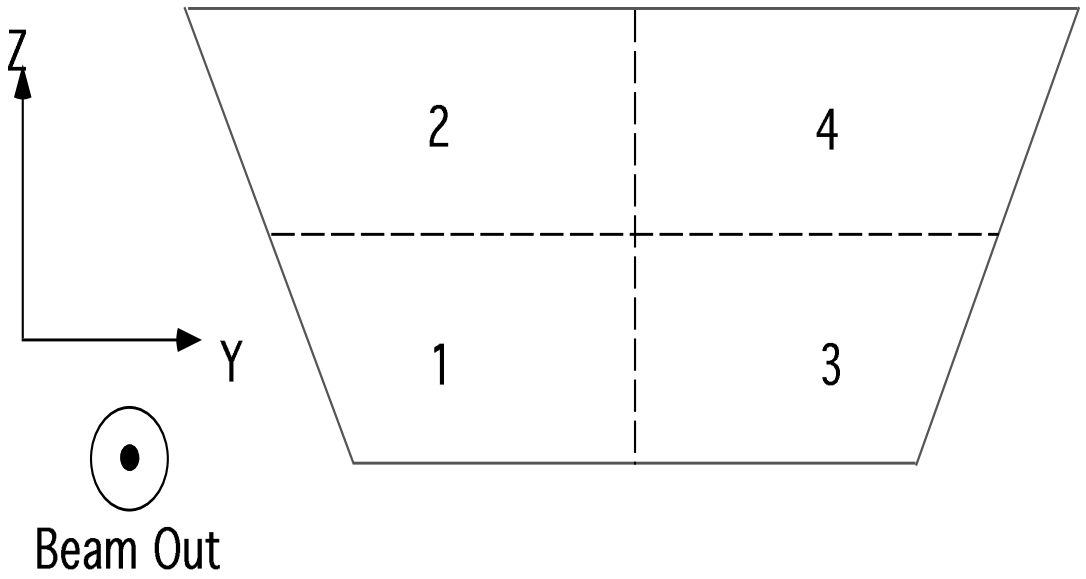

Figure 4.2: The MWPCs are divided into four logical quadrants to enable the efficiency calculation to take account of variations across the plane.

become excessive.

The efficiencies have been calculated separately for the field 'down' and 'up' polarities of the run. In addition, the total efficiency for the whole run has been calculated by combining the two sets of data. This represents 252 efficiencies of which the total efficiencies are listed in Appendix D. A sample of the results are presented in graphical form in figures 4.3, 4.4 and 4.5. Nearly all the efficiencies are greater than 90% and show no overall field dependence. There is also no dramatic fall off in efficiency over the different quadrants, although there is a reduced efficiency in plane V of chamber 7, especially in quadrant 2, see figure 4.5, which has been observed in earlier WA85 runs.

4.1.3 Chamber Edge Effects

The method used to create the 'Butterfly' profile was described in section 2.3.1. The effect of the removal of graphite paint from the chamber planes can reasonably be expected to alter the working efficiency of the planes near the edges of the profile region. A study was carried out [60] to consider the possible fall off in efficiency due to this process. Figure 4.6 shows the change in the efficiency with distance from the nominal butterflied chamber edge for the three planes of A1 and A7. Clearly, the efficiency is seen to drop-off gradually over the last $\sim$ 1 cm. To account for this systematic effect in all the analysis and chambers efficiency calculations a cut of 1 cm around the interior of all the chambers has been made. This increases confidence that the efficiency is uniform in the region used.

4.2 Scintillator Hodoscope Efficiencies

A preliminary study of the effectiveness of the hodoscopes in the run was carried out before the hodoscope efficiencies were determined in full. This study

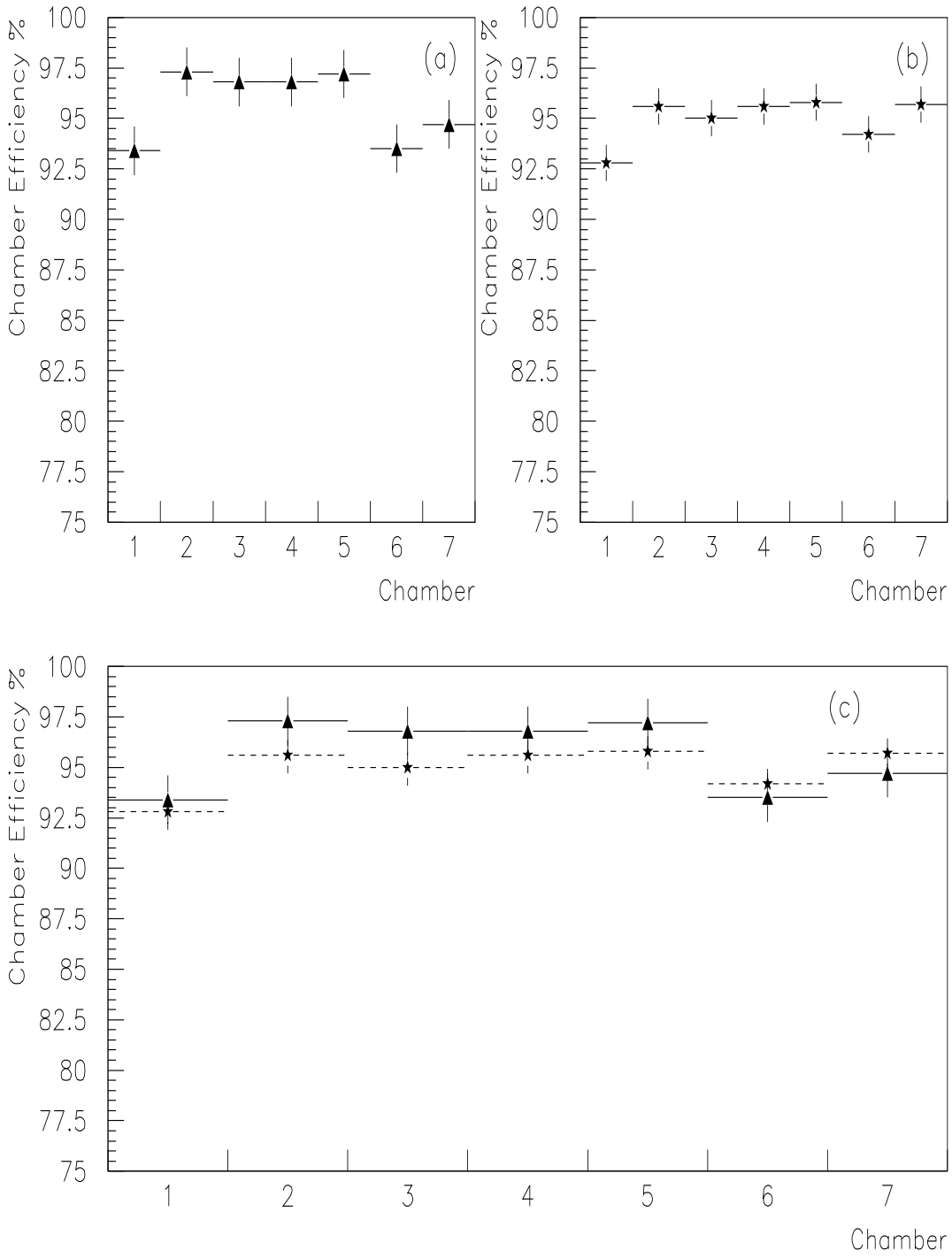

Figure 4.3: Chamber efficiencies in the case of plane Y, quadrant 3 for (a) field down; (b) field up; and (c) superimposed fields.

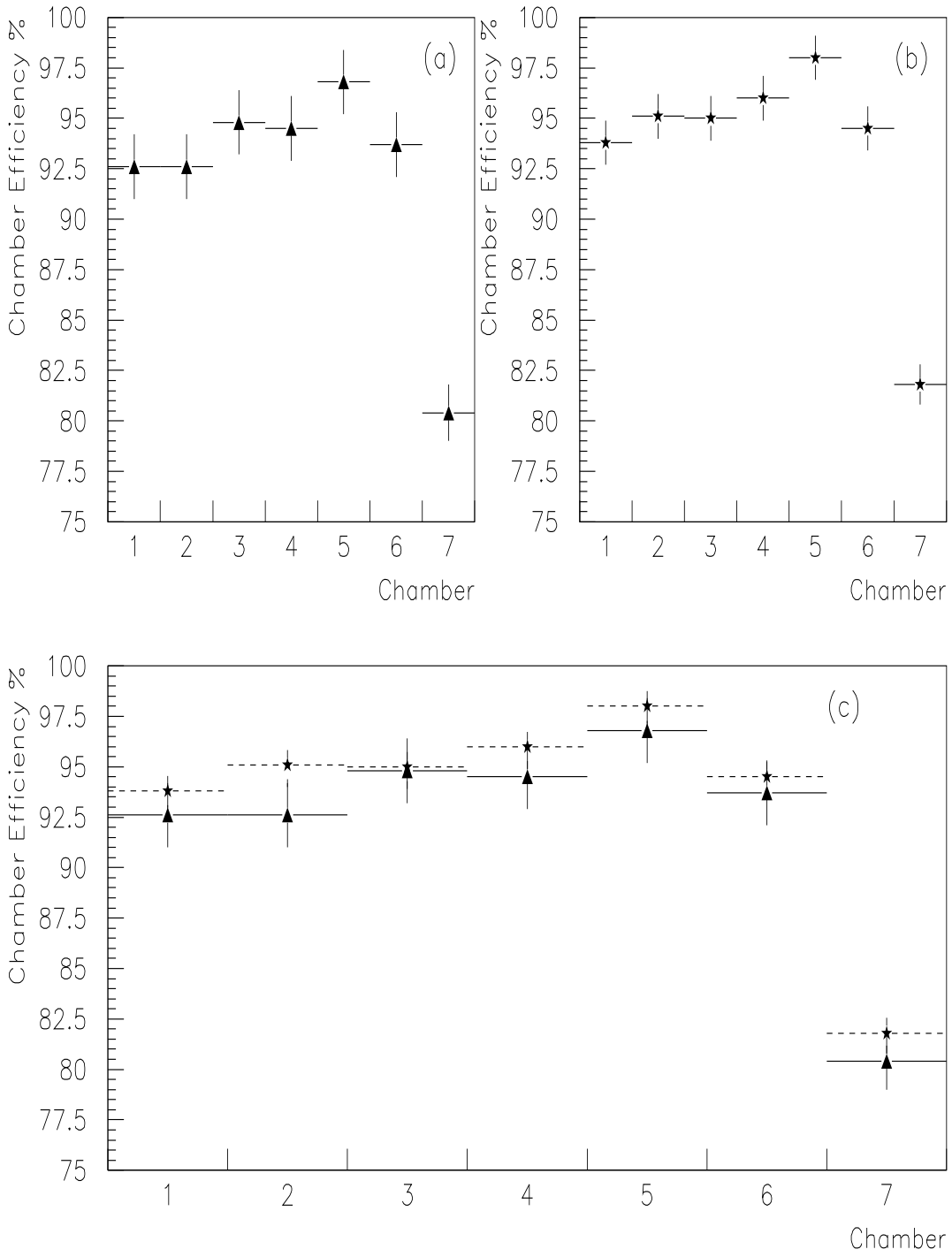

Figure 4.4: Chamber efficiencies in the case of plane V, quadrant 2 for (a) field down; (b) field up; and (c) superimposed fields.

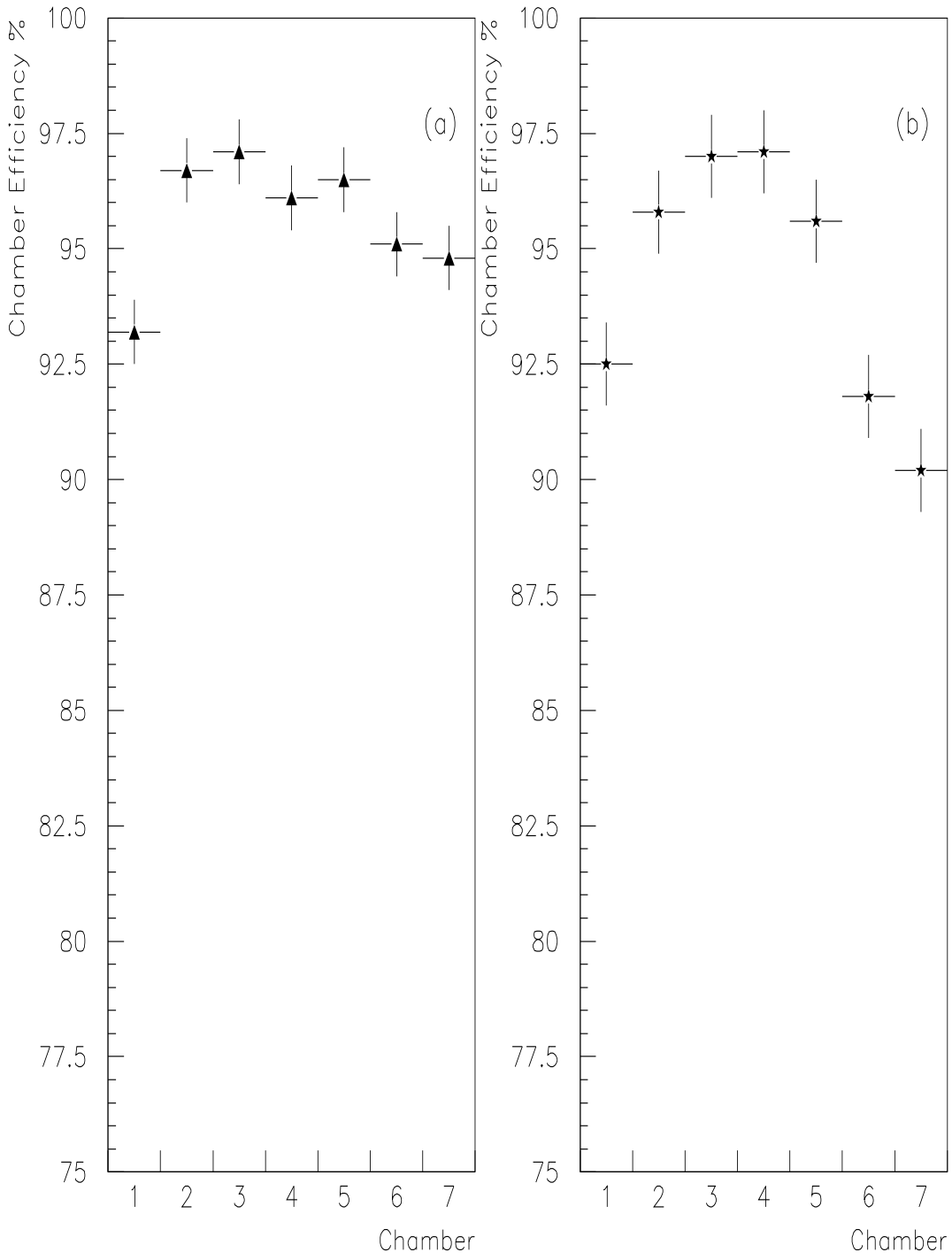

Figure 4.5: Total chamber efficiencies for (a) plane Y, quadrant 1; and (b) plane U, quadrant 2.

Figure 4.6: Chamber efficiency variation close to the edge of the chamber defined by the butterflying process for chamber 1 (a) plane Y; (b) plane U; and (c) plane V. The population of reconstructed tracks at the edge of the butterfly region are shown in (d).

was very helpful in developing the efficiency calculation method described in section 4.2.2.

4.2.1 Preliminary Hodoscope Study

It is important to determine any shift in the expected positions of the hodoscopes accurately. This cannot be carried out in the manner used for the A chambers, because the hodoscopes are not used in the track fitting of TRIDENT. In addition, the noise levels in the hodoscopes must be investigated with emphasis placed upon the effect of noise interfering with tracks firing the slabs of HZ0 and HZ1.

Any shift in the expected positions of the Omega coordinates of the 5 active slabs in both hodoscopes HZ0 and HZ1 can be checked by considering events which satisfy the requirement of only one track which can be traced to the hodoscope planes and only one 'fired' hit in one slab of the hodoscope half the track is traced to. So if, for example, slab 13 of the right-hand half of HZ0 fired, then the Omega y and z coordinate positions of the track traced to the HZ0 plane can be found and should define the outline of slab 13 in this case. Figure 4.7 illustrates the method outlined in the text. This method will only work however, if the noise levels in the hodoscope are low, so that the track is the main cause in triggering the fired slab when it passes through it. This study then provides a measure of the effectiveness of the hodoscopes as a track triggering device in the WA85 scheme for proton events.

Figure 4.8 (a) to (d) show the coordinates of tracks traced to the x position of HZ0 and HZ1 in the yz plane for the cases where the right side slabs 12 and 14 respectively have fired. It is found that about 99% of the tracks from level 1 events trace to the expected positions of the slabs within a fiducial 1 cm region around the exterior of the slabs. The 1 cm fiducial region is used to counteract the expected track smearing, because of tracing errors at this

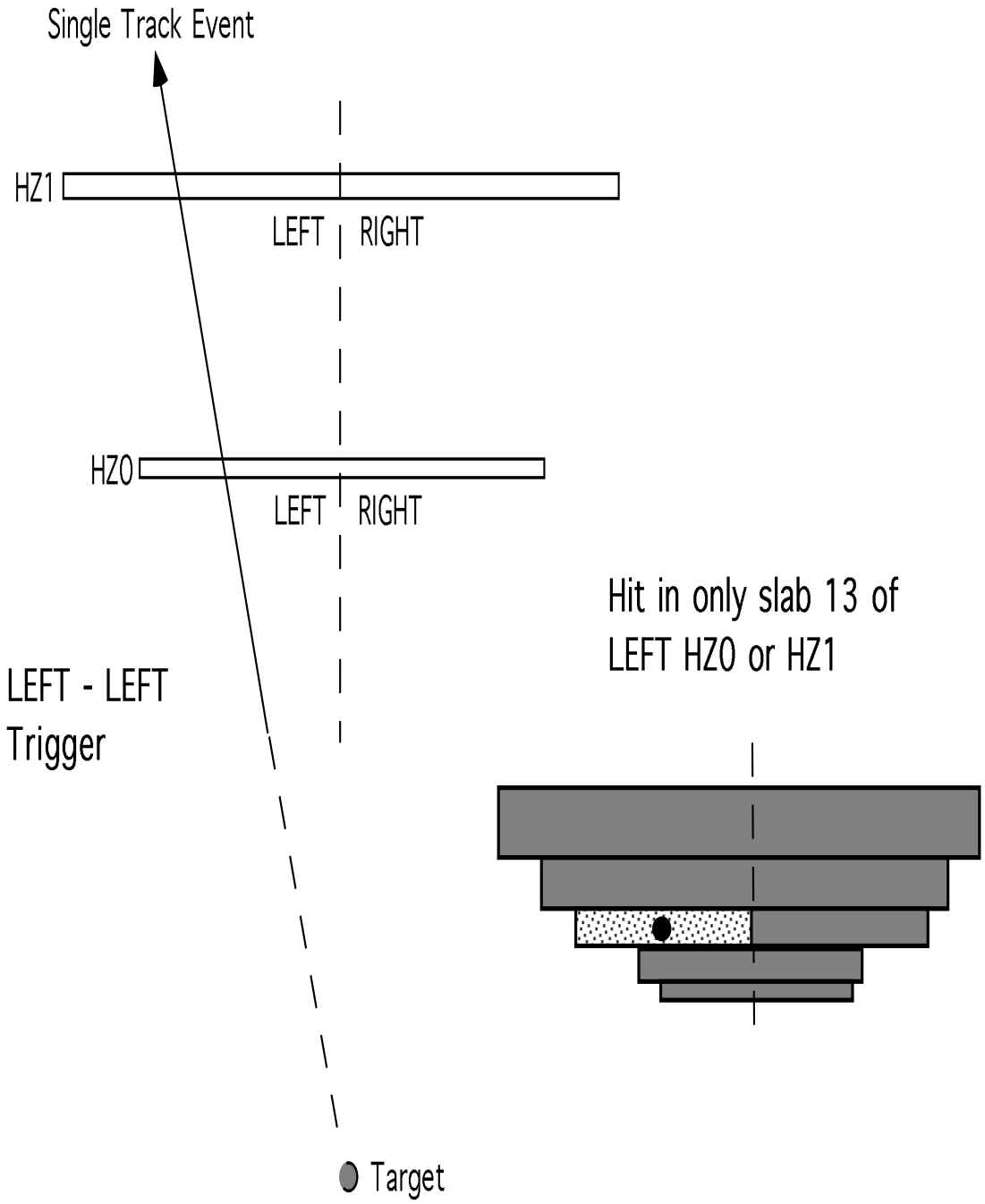

Figure 4.7: Schematic to show the requirements used to consider events for the hodoscope investigation.

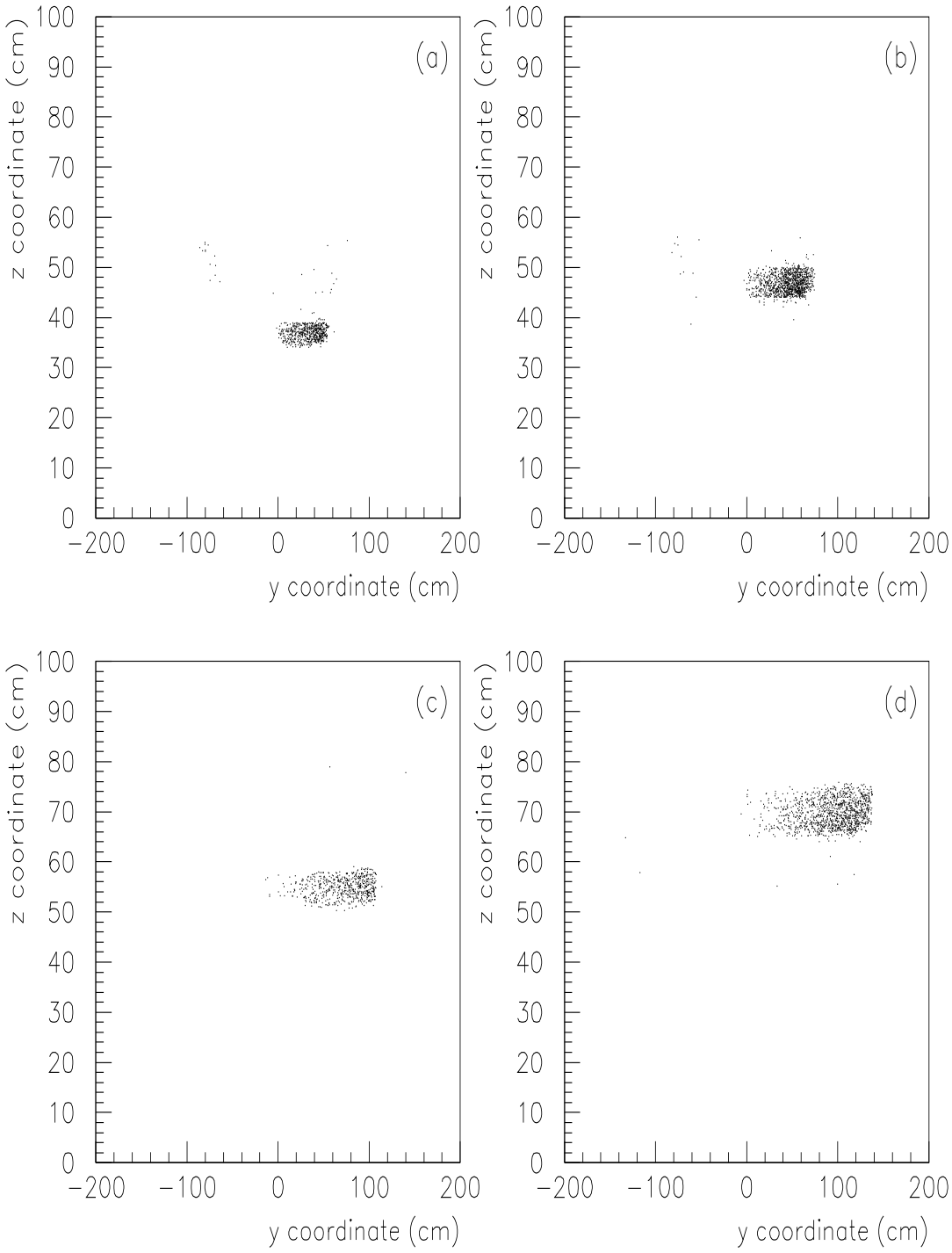

Figure 4.8: Omega coordinates of the track in the yz plane at the x position of HZ0, where only slabs (a) 12; (b) 14 in the right side of HZ0 have fired and the x position of HZ1, where only slabs (c) 12; (d) 14 in the right side of HZ1 have fired.

distance from the 'A' chambers, especially in the case of HZ1. This smearing is better illustrated in figure 4.9 (a) to (d), where the residual between the expected z centre of slabs 12 - 15 respectively and the z coordinate of the traced track for the left-hand half of HZ1 is plotted. In all cases the width of the residual is about 0.5 cm larger than the actual width of the slab. The central values which were determined are within 1 mm of the 'expected' central values.

The 1% of events where the tracks have traced outside the fiducial region are the events which have been triggered by noise. Indeed, there is no sign of adjacent slab firing, where tracks which have passed through one slab have caused a neighbouring slab to fire. This is illustrated in figure 4.10 which shows the number of fired slabs in the case for events where slab 12 in 4.10 (a) and slab 13 in 4.10 (b) in the left side of HZ0 have fired due to tracks passing through there defined region. All that is seen in the adjacent slabs is a noise background dependent on the size of the slab.

4.2.2 Hodoscope Efficiency Method

The hodoscope efficiencies were determined using approximately 100,000 interaction triggered events which were sampled over the run. At the interaction level of the trigger the hodoscopes were not used so these events are suitably unbiased. This trigger level was discussed in section 2.4.2. To calculate the hodoscope efficiencies slab by slab the requirement for 'good' tracks was that they should have seven space points so that their momentum is very well defined and that the track traces to the hodoscope of interest. The slab which a track traces through is recorded and then the electronics block for that event is looked up to determine if that slab fired. If this condition is satisfied then the track is deemed to have successfully fired the slab. The smearing effect mentioned in the previous section must be taken into account.

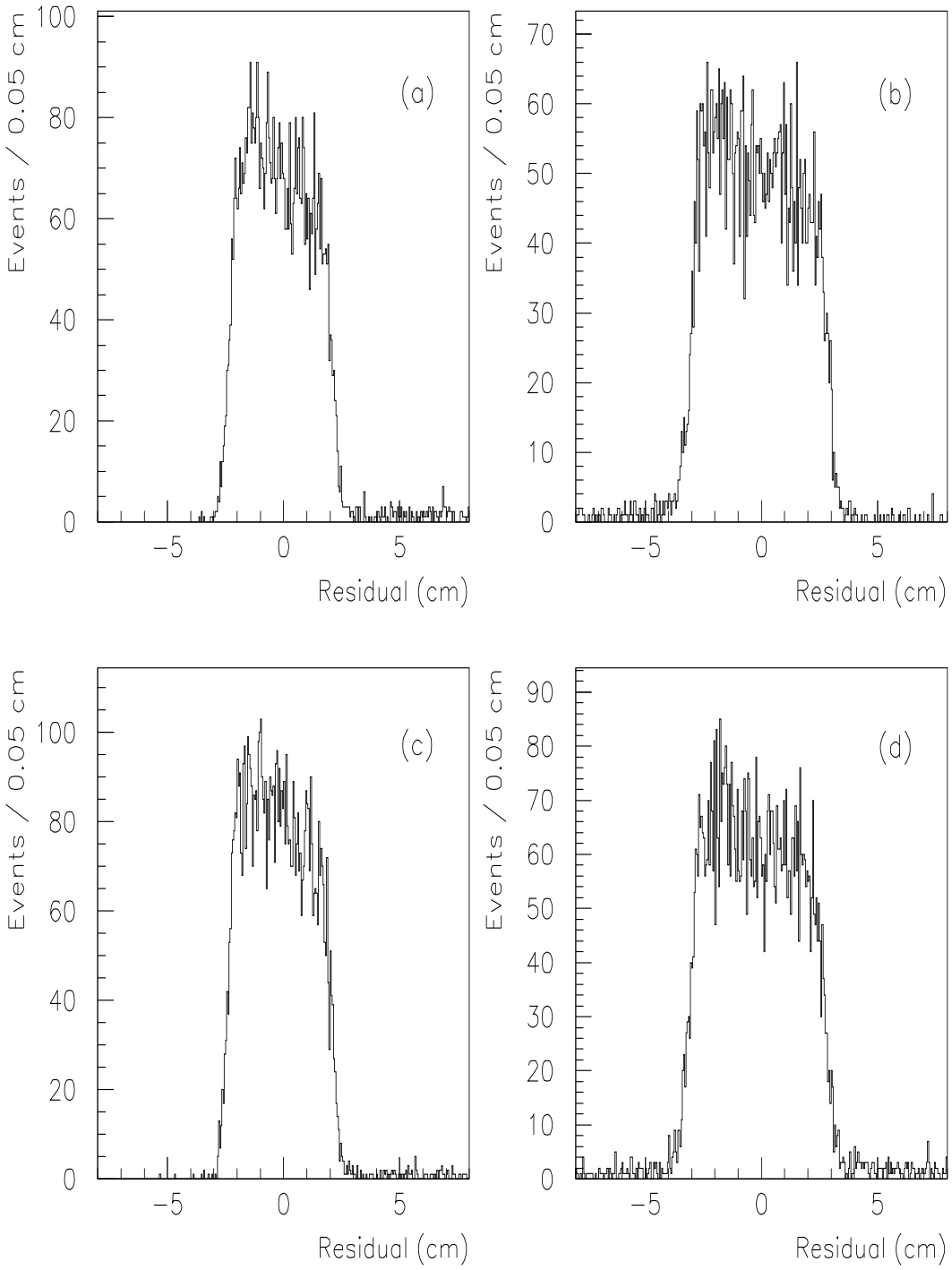

Figure 4.9: Residual in the Omega z coordinate between track position and the centre of the slab where 'only' slabs (a) 12; (b) 13; (c) 14; or (d) 15 have fired in the left side of HZ1.

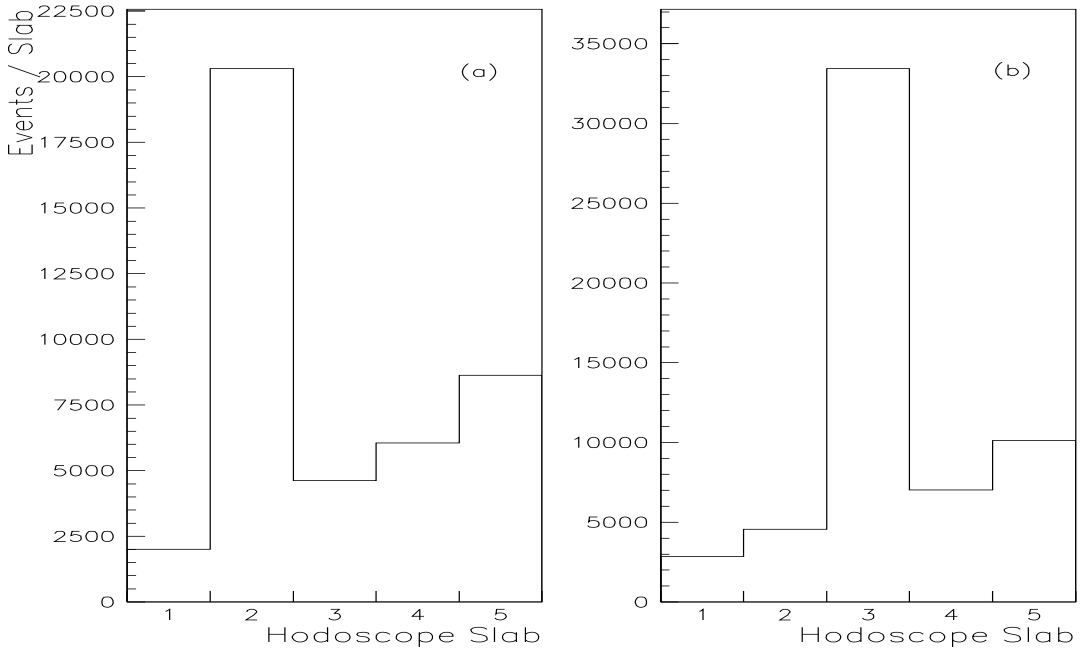

Figure 4.10: Plot of fired slabs in HZ0 LEFT, where only slabs (a) 12; or (b) 13 have been required to fire; Note the adjacent slabs do not fire substantially more than would be expected by noise which reflects their geometry.

If a track in reality passes through the hodoscope outside the region defined by a particular slab, but due to tracing errors is believed to pass through this slab then it would effectively reduce the efficiency of that slab, because it could not possibly have caused it to fire. So to account for this problem the tracks used in the efficiency calculation were required to pass through a region 1 cm inside the interior of the slab of interest. Also, for comparison a less restrictive region of 0.5 cm and a tighter region of 1.5 cm were used.

4.2.3 Hodoscope Efficiency Results

The slab efficiencies for both halves of the hodoscopes HZ0 and HZ1 are listed in Appendix E in full. The efficiencies are also given in graphical form in figure 4.11. In figure 4.11 (a), (b) and (c) the efficiency per slab for the edge cut region of 0.5 cm, 1.0 cm and 1.5 cm are shown respectively. It is seen that there is a slight increase in the efficiency per slab in the case where the larger 1.0 cm edge cut was used from that of the 0.5 cm cut. However, the

larger cut of 1.5 cm did not significantly change the efficiencies and the 1.0 cm efficiency results were used for further analysis. Most of the efficiencies were found to be greater than or equal to 80%.

4.3 Summary

The physical efficiency of the wire chambers and scintillator hodoscopes has been calculated. These will ensure that the physical characteristics of the detector can be incorporated in the calculation of the reconstruction efficiencies for a particular particle decay in the case of the A chambers and acceptances in the case of the hodoscopes. The A chamber efficiencies were found not to vary significantly with the field and were quite constant over the wire planes. A detailed study into the workings of the hodoscopes during the run has been undertaken and the understanding gained concerning the effectiveness of the hodoscopes has been used in the calculation of their efficiencies. The variation across the hodoscope planes slab by slab is significant enough so as to expect the acceptances to be sensitive to these findings; this is studied in the next chapter.

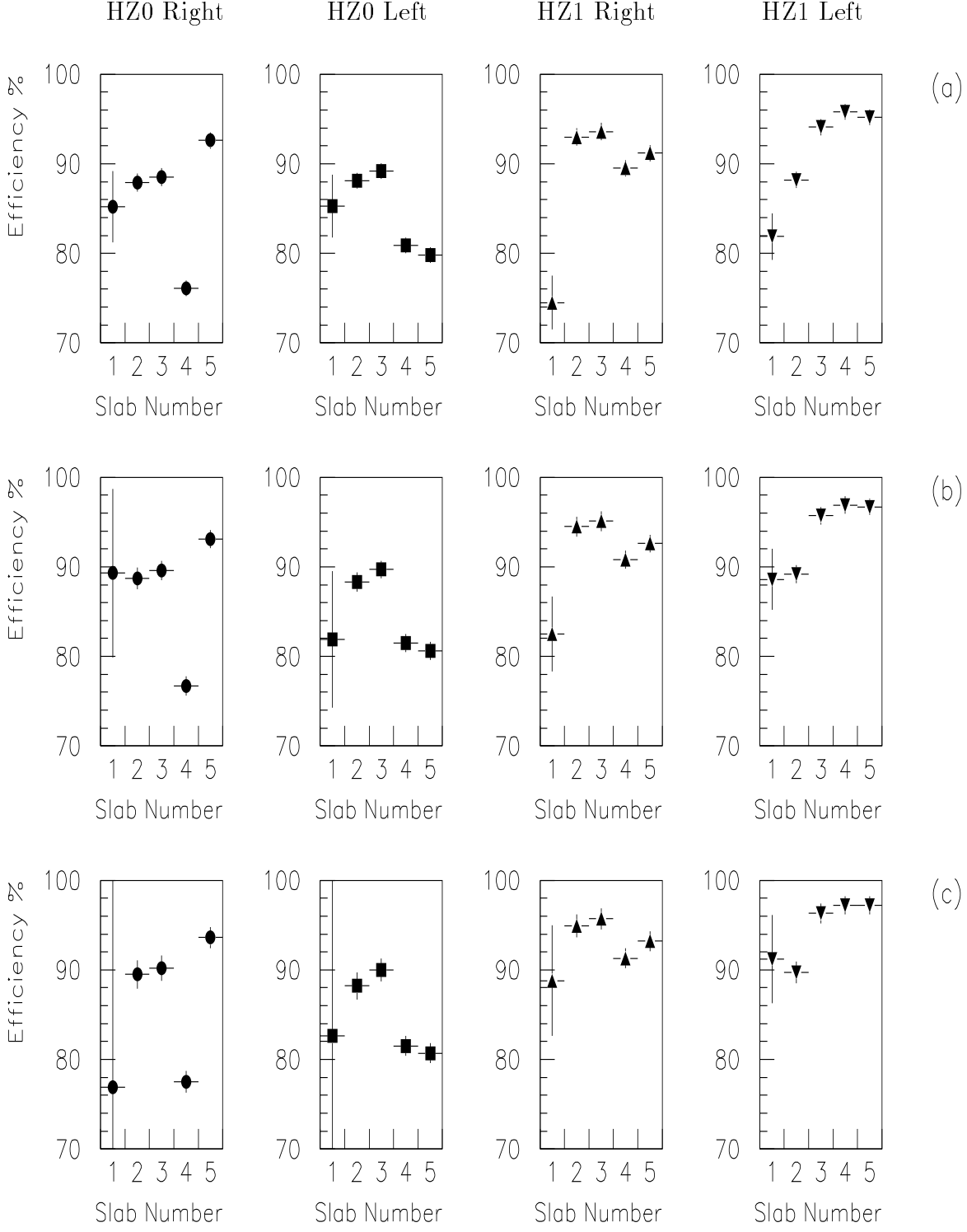

Figure 4.11: The hodoscope efficiency per slab for HZ0 and HZ1 for a (a) 0.5 cm; (b) 1.0 cm; and (c) 1.5 cm fiducial edge gap around the interior of each slab; the slab numbers 1 to 5 correspond to the slab numbers 11 to 15 in the Omega scheme.

Chapter 5

Acceptance and Reconstruction Efficiencies

The main aim of the WA85 experiment is to investigate the relative production rates of strange baryon and antibaryon decays. In addition, strange meson decays are of great interest and with h^- yields can be used as a comparison with the baryonic decays. This information can lead to a greater understanding of the dynamics of the constituents of S-W and p-W reactions. To be able to compare the various particle species a full understanding of the performance of the WA85 detector is required. A perfect detector would find all particles emanating from the region of interaction. In reality, some particles are lost, and 'fake' signals occur. This has the effect of reducing the number of reconstructed V^0s, h^-s and cascades. The losses are determined by way of two major calculations.

Geometrical acceptance is essentially a measure of how the geometry of the experimental apparatus constrains the number of particles detected. Tracks were measured if they emanated from the target within a narrow solid angle of approximately 2% of the total 4π. This limits the tracks kinematic range to $p_T \geq 0.6$ GeV/c in a rapidity interval of $2.0 \leq y_{lab} \leq 3.2$. Of course

the complex nature of, for example, a Λ or Ξ^- decay, compared with that of tracks from the target, make the understanding of how the geometry of the detector affects the reconstruction of such decays more difficult, but of vital importance. The spatial cuts discussed in chapter 3 for different particle decays, such that tracks from a decay vertex must trace through a specified number of A chambers and that the x coordinate of the vertex of, for example, a Ξ^- decay, must be in a certain region, will inevitably affect the acceptance and so must be accounted for. In addition, the data is corrected for unseen decay modes, such as $\Lambda \rightarrow \mathrm{n} + \pi^0$.

Reconstruction efficiency provides a measure of the effectiveness of the analysis programs to reconstruct the correct signal from the detector. Reconstruction efficiencies are determined by the ability of the reconstruction software in terms of track identification and momentum fitting and in addition decay vertex finding. Incorporated within the reconstruction efficiency calculation is the electronic efficiency of the relevant parts of the detector used in the run, in this case the wire chambers, which were calculated in section 4.1. This will of course reduce the number of space points produced per track and so adversely affect the track fitting and vertex finding.

5.1 Method of Acceptance

To determine the geometrical acceptance of the detector, a known number of Monte Carlo particles are generated with an identical rapidity, y_{lab} and transverse momentum, p_T, which corresponds to the centre of a square region of $y - p_T$ whose size is 0.05 units of y_{lab} by 0.1 GeV/c in p_T. Using many such squares a grid can be produced, which will be sensitive to the gradual changes in the acceptance over the entire range of $y_{lab} - p_T$ studied.

The particle is then assigned the following kinematic components

$$\begin{aligned} m_T &= \sqrt{M^2 + p^2{}_T}, \\ p_L &= m_T \sinh(y_{lab}), \\ |\, p \,| &= \sqrt{p^2{}_T + p^2{}_L}, \end{aligned}$$

where p_L is the longitudinal momentum, M, the mass of the particle, m_T, the transverse mass and $|\, p \,|$, the total momentum of the particle.

The particles are generated randomly in the upper hemisphere of Omega as the region below the beam was not used in the experiment. Thus the azimuthal angle, ϕ, is allowed to range between from 0 to π radians. Each particle is decayed isotropically taking into account the lifetime distribution associated with a particular decay. The tracks from the decay system are then traced through the A chambers. For a given hyperon decay, the simulated tracks are required to trace through the same number of chambers as the corresponding real tracks. In addition, to define the acceptance at least one track must pass through the hodoscopes and satisfy the level 1 stage of the trigger, which was discussed in chapter 3. The acceptance is essentially defined by the number found divided by the number generated.

5.1.1 Calculation of Λ and K^0 Acceptances

In the case of the Λ decay, for each value of the azimuthal angle, ϕ, a decay length along the flight of the Λ is produced by a random distribution according to the exponential decay of the Λ whose mean lifetime is given by τ. The decay probability, $P(\ell)$, that a particle of mass M travels a distance ℓ or greater before decaying is given by

$$P(\ell) = \exp\left(-M\ell/\tau p\right).$$

This leads to the determination of the distance of the Λ decay given by

$$d = -\frac{\tau p}{M_\Lambda} \ln(r),$$

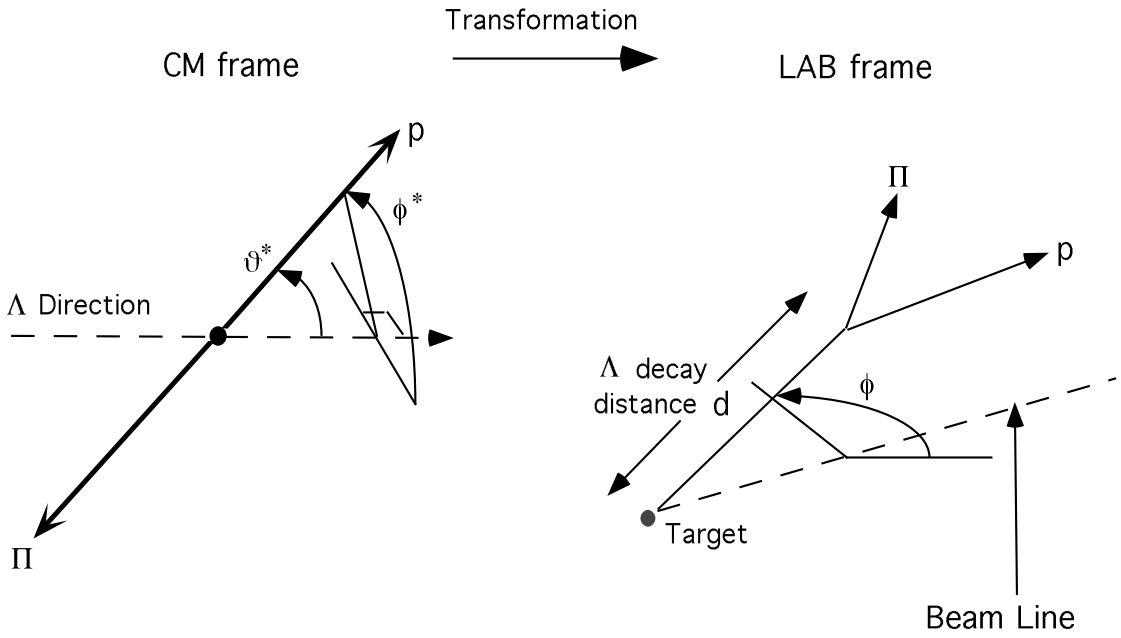

Figure 5.1: Generation of Λ and decay products for the acceptance calculation.

where the $c\tau$ for the Λ is 7.89 cm and r is a random number generated with a flat distribution between 0 and 1. If the decay vertex is found in the region $0 \leq x \leq 90$ cm the Λ is accepted at this stage of the calculation.

The decay tracks are generated isotropically in the CM frame of the Λ with equal and opposite momentum, as illustrated in figure 5.1; the tracks are then boosted to the laboratory frame. The decay tracks are traced through the A chambers and to the hodoscope planes. Both tracks must pass through A1 and A7 and at least one track must satisfy the level 1 hodoscope trigger requirement, which to the level of 90% is the proton. The variation in the efficiency across the hodoscope planes could reasonably be expected to affect the $y_{lab} - p_T$ spectra of a Λ decay. This is accounted for by allowing the hodoscope slab efficiencies to weight the event in the following manner. Firstly the proton is traced to the hodoscope planes being the most likely track from the decay to reach HZ0 and HZ1. Upon satisfying the level 1 condition, if the combination of the efficiencies [1] of the two slabs which the track passed through is less than a random number generated between 0 and 1 then the

[1] each slab efficiency has a maximum of one.

proton track has failed the hodoscope efficiency criteria. If the proton fails at either the level 1 or hodoscope efficiency stage of the acceptance calculation then the process is repeated with the π^- .

In addition, the Λ decay must be unambiguous (*i.e.* the Armenteros-Podolanski variable, α, lies in the range $0.45 \leq \alpha \leq 0.6$). If these conditions are satisfied the decay is accepted. The acceptance is defined by,

$$\textbf{Acceptance} = \frac{\textbf{no.out}}{\textbf{no.generated}} \times \frac{\textbf{1}}{\textbf{2}} \times \textbf{0.641}$$

The factor of 1/2 is a result of the Λ being generated only in the upper hemisphere; the factor 0.641 accounts for unseen decay modes. For each $y_{lab} - p_T$ point 1,000,000 Λs were generated.

The K^0 acceptance table is generated in a very similar manner to that of the Λ with a $c\tau$ of 2.676 cm and an α cut of $-0.45 \leq \alpha \leq 0.45$. The factor to account for hidden decay channels is 0.686. The only major difference in the cuts is reflected in the treatment of the vertex for the K^0 decay with respect to the Λ decay. As described in chapter 3 both the vertex and other 'crossing' must lie in the fiducial region of $-15 \leq x \leq 90$ cm.

5.1.2 Calculation of Ξ^- and π^- Acceptances

The Ξ^- acceptance table was generated in a similar manner to that of the Λ table. The Ξ^- is decayed isotropically to a Λ and π^-; the Λ is in turn decayed isotropically. The Ξ^- decay length distance is given by

$$d = -\frac{\tau \mathrm{p_L}}{M_\Xi} \ln(r),$$

where the $c\tau$ of the Ξ^- is 4.91 cm. To accept a Ξ^- its decay vertex must lie in the fiducial region $-40 \leq x \leq 90$ cm and the decay vertex of the Λ must be in the range of $-15 \leq x \leq 90$ cm. In addition, the three decay tracks must trace through the first four A chambers and either the p or π^- from the Λ decay is required to satisfy the level 1 hodoscope condition. The π^-

from the Ξ^- decay satisfies the hodoscope cut less than 1 % of the time. The impact parameter cut which demands that the π^- from the Ξ^- decay misses the target by at least 6 cm is also incorporated due to its geometrical nature. As for the Λ calculation the statistics per $y_{lab} - p_T$ point were 1,000,000.

In the case of the π^- acceptance table only 100,000 statistics were used due to the much higher acceptances involved. The π^- is required to satisfy the hodoscope condition as well as tracing through the seven MWPCs.

5.1.3 Acceptance Results

The acceptance tables for the Λ, K^0, Ξ^- and π^- particles determined for the p-W data are given in Appendix F. The results are also presented in graphical form for the Λ, K^0 and Ξ^- decays in figures 5.2 (a), 5.3 (a) and 5.4 (a) respectively, along with the equivalent acceptances, without the hodoscope condition, used for the S-W data in figures 5.2 (b), 5.3 (b) and 5.4 (b). The π^- acceptances are given in figure 5.5. The acceptances for the corresponding antiparticles are the same due to the symmetry of the magnetic field and apparatus.

It is noted that the shape of the acceptance plot in the region of high acceptance upon inclusion of the hodoscope trigger condition tends to narrow and shift towards slightly higher rapidities. Essentially, at lower rapidity for a specified transverse momentum the proton will tend to miss the hodoscope planes. The most obvious difference is in the shape of the π^- acceptances where a distinct dip is seen at a transverse momentum of approximately 1.4 GeV/c. The existence of this 'valley' region arises directly out of the RIGHT-RIGHT or LEFT-LEFT level 1 hodoscope condition. Tracks of various $y_{lab} - p_T$ points within the area of the 'dip' were traced to the hodoscope planes and the y coordinate of their intercepts on the two planes were recorded. The correlation of the y coordinates in the two hodoscopes is shown in figure

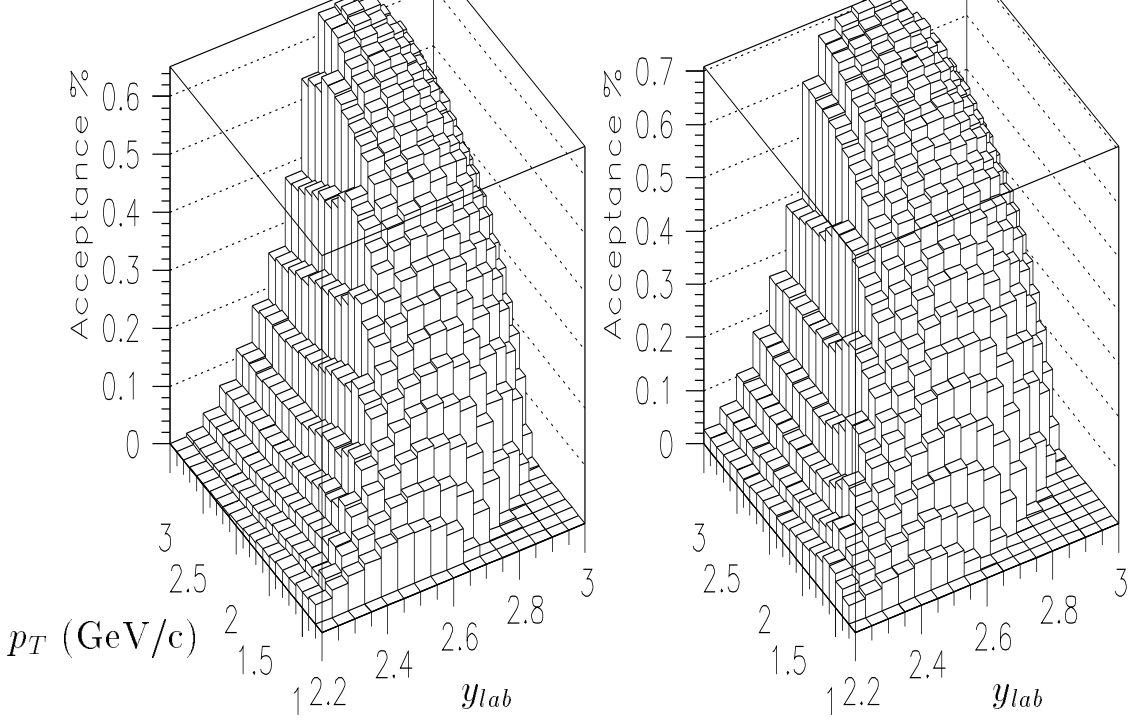

Figure 5.2: Geometrical acceptances for (a) Λs with the hodoscope condition; and (b) Λs without the hodoscope condition.

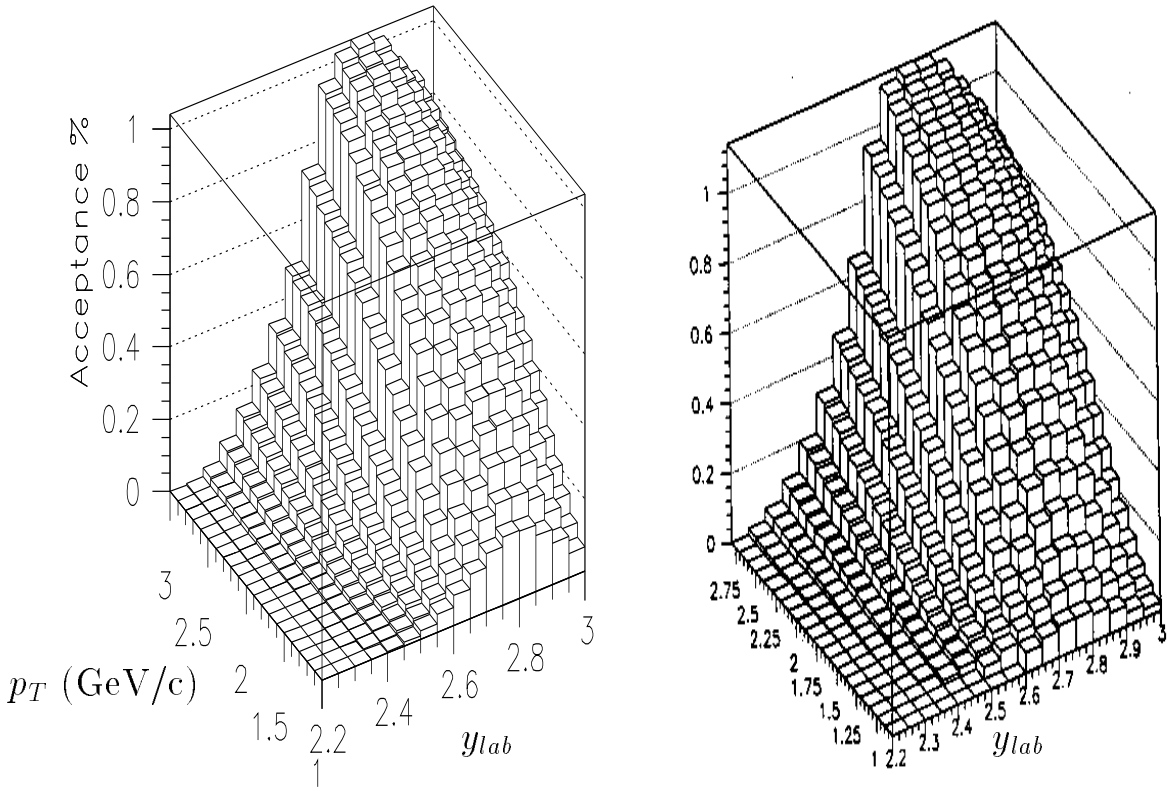

Figure 5.3: Geometrical acceptances for (a) K^0s with the hodoscope condition; and (b) K^0s without the hodoscope condition.

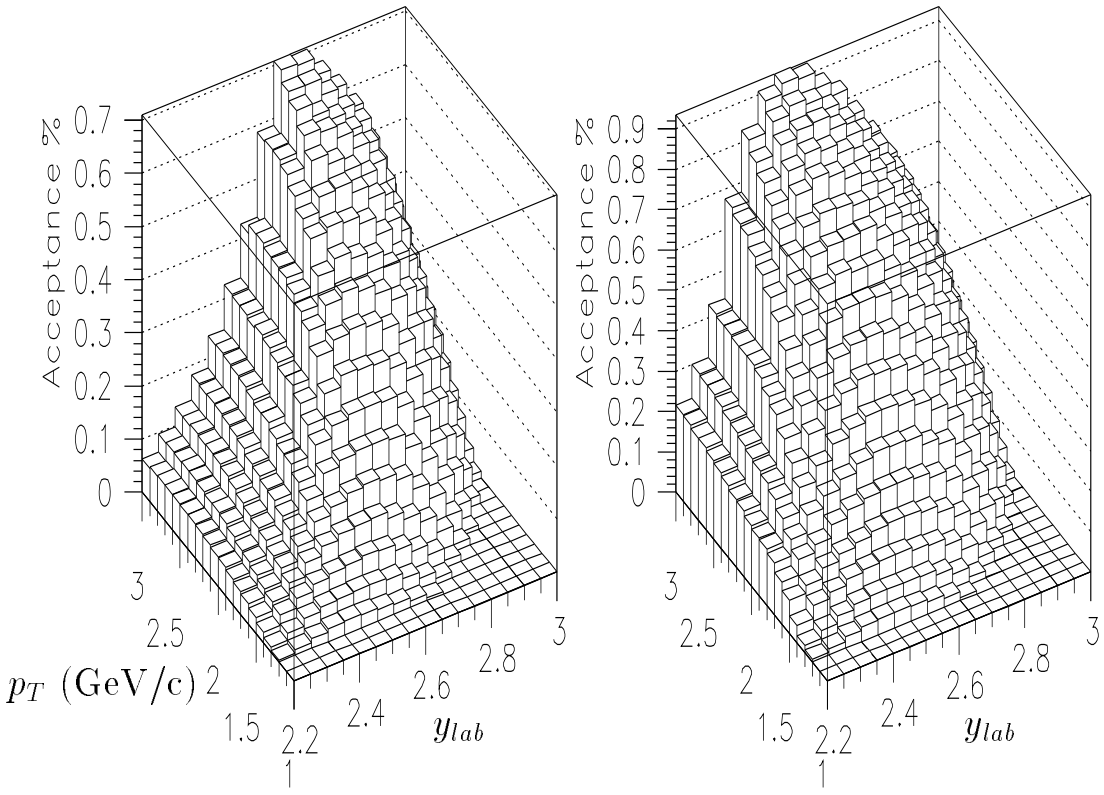

Figure 5.4: Geometrical acceptances for (a) Ξ^-s with the hodoscope condition; and (b) Ξ^-s without the hodoscope condition.

5.6. Tracks whose $y_{lab} - p_T$ is well within the 'dip' area are found to sweep from positive to negative y Omega coordinate positions when incident upon HZ0 and HZ1 respectively, so failing to fulfill the level 1 requirement. The 'valley' can also be seen in the real data. In figure 5.7 the p_T spectra for level 1 negatives is shown for a cut in the rapidity of (a) $2.2 \leq y_{lab} \leq 3.0$ and (b) $2.2 \leq y_{lab} \leq 2.4$. There is a noticeable dip in the latter plot which centres the data upon the 'dip' region.

The events which are used for the final corrected analysis are those which lie in regions of 'good' acceptance, defined by a variation of a factor of 10 from the value of maximum acceptance used.

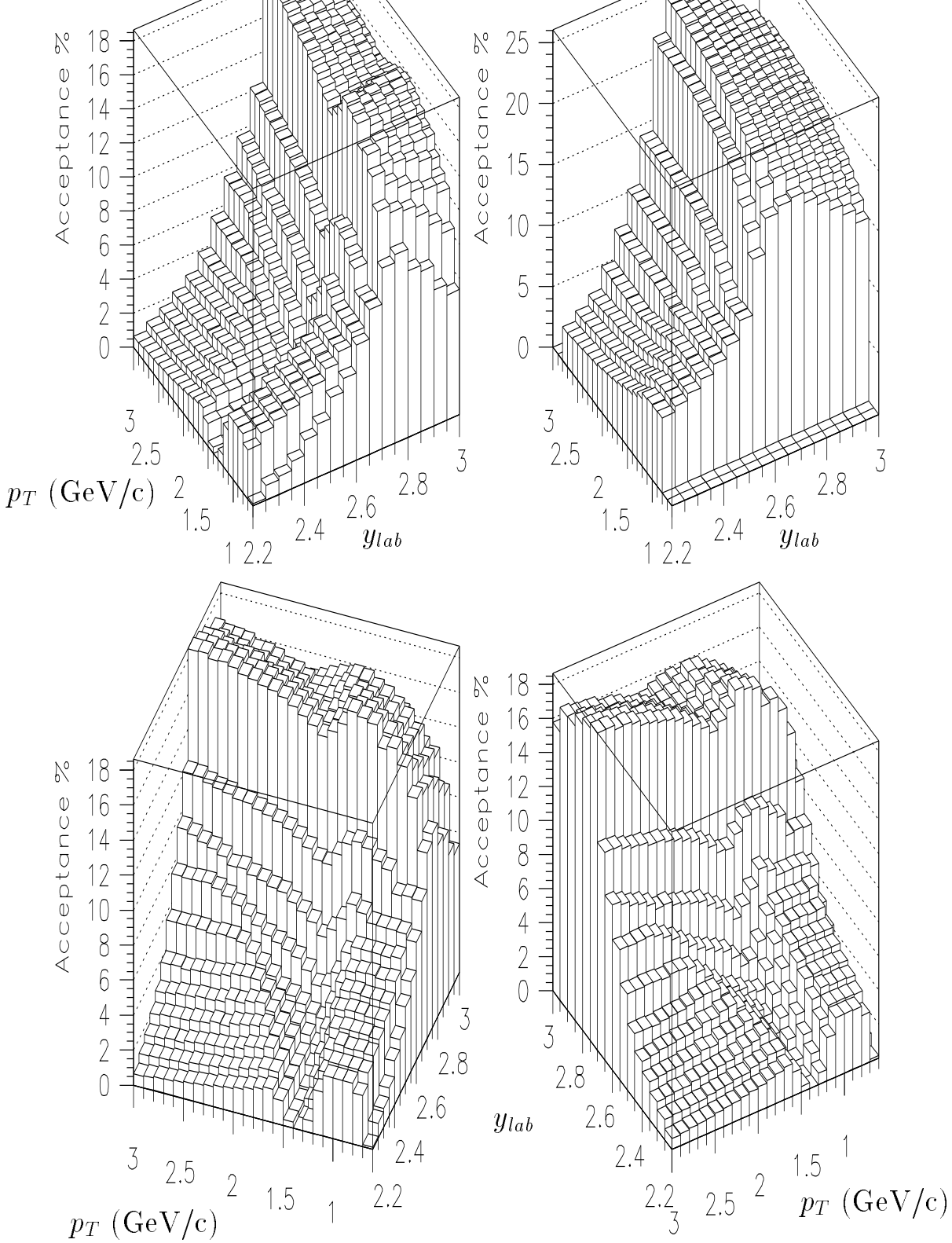

Figure 5.5: Geometrical acceptances for (a) π^-s with the hodoscope condition; and (b) π^-s without the hodoscope condition. To illustrate more clearly the differences arising in the acceptances due to the hodoscope condition plots (c) and (d) show rotated versions of (a).

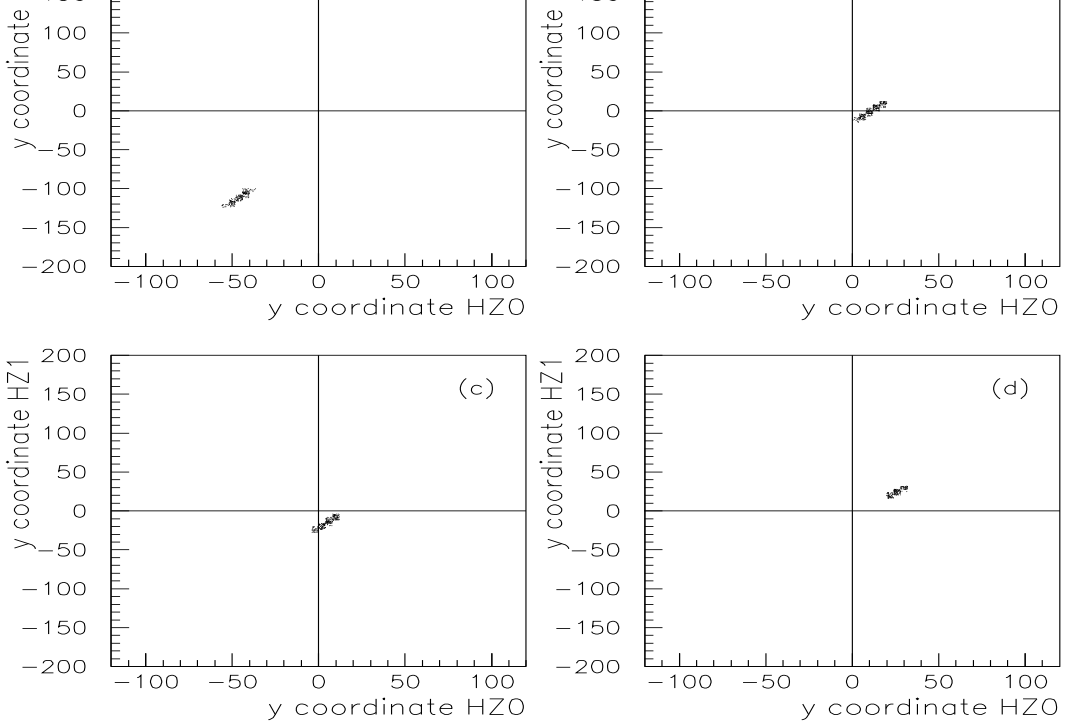

Figure 5.6: Correlation of y coordinate of tracks, with specific $y - p_T$ points, incident on HZ0 and HZ1. For (a) p_T - 0.75, y - 2.275; (b) p_T - 1.35, y - 2.325; (c) p_T - 1.45, y - 2.425; and (d) p_T - 2.15, y - 2.325.

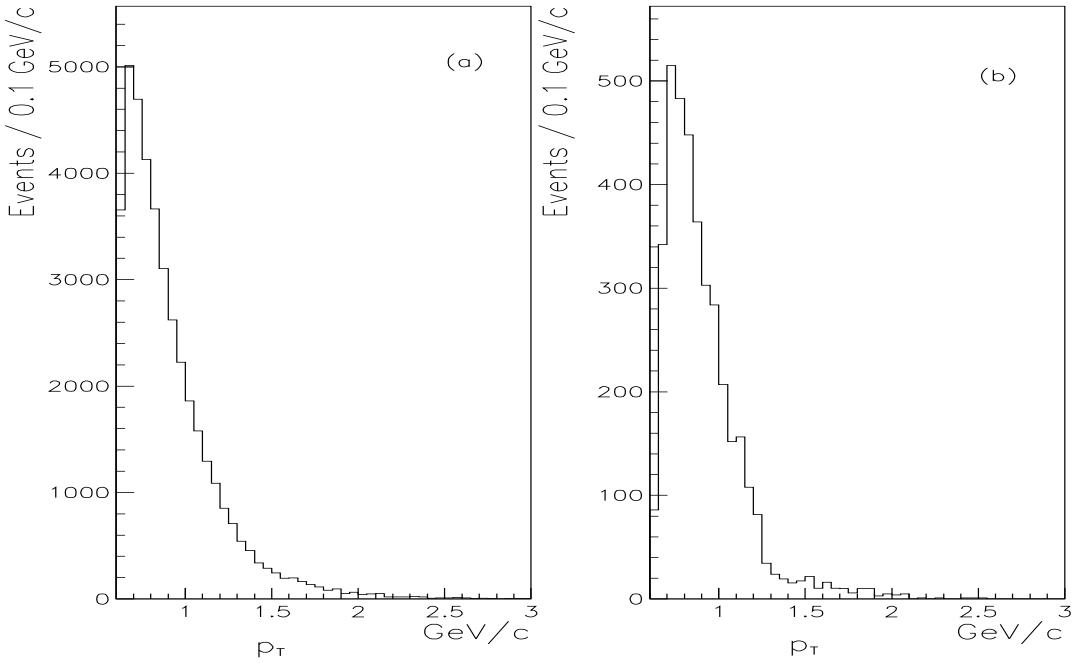

Figure 5.7: Transverse momentum spectra for real negatives which satisfy the level 1 condition and pass the following rapidity criteria (a) $2.3 \leq y_{lab} \leq 3.0$; and (b) $2.2 \leq y_{lab} \leq 2.4$.

5.2 Reconstruction Efficiency

As was discussed in the introduction to this chapter it is crucial to take account of the performance of the WA85 experiment in detecting and reconstructing tracks and decay vertices, such as a Ξ^- decay which involves two decay vertices and three tracks. Reconstruction efficiencies are calculated by generating a large number of Monte Carlo particles in the same manner as the acceptance particles were produced. The tracks from these particles are then traced through a detector simulation whose job is to simulate hits in the MWPCs according to the chamber efficiencies associated with the 21 planes of the A chambers. To ensure that the Monte Carlo events are able to imitate real events the simulated cluster hits are implanted into real event records. The process of analysis then continues as for the real data. The reconstruction efficiency is considered as a function of the mean cluster multiplicity per plane in the MWPCs. This parameter has been found [61] to be directly related to the reconstruction efficiency. Typically higher multiplicity densities per plane result in lower reconstruction efficiencies.

In figure 5.8 the flow diagram of the reconstruction efficiency chain is shown. In the following sections the efficiency chain will be explained in greater detail, examining certain subtleties inherent to the calculation.

5.2.1 Reconstruction Efficiency Method

The finished Monte Carlo event is produced by two programs. The first program NAININ generates the 4-vectors relevant to the particle of interest. This event must satisfy the acceptance implications of the detector and selection criteria described in chapter 3 with an allowance made for smearing to be considered as a 'good' event. Smearing is described shortly.

The event record of this program contains the coordinates of the hits on each plane of each chamber for every generated track. In addition, cut infor-

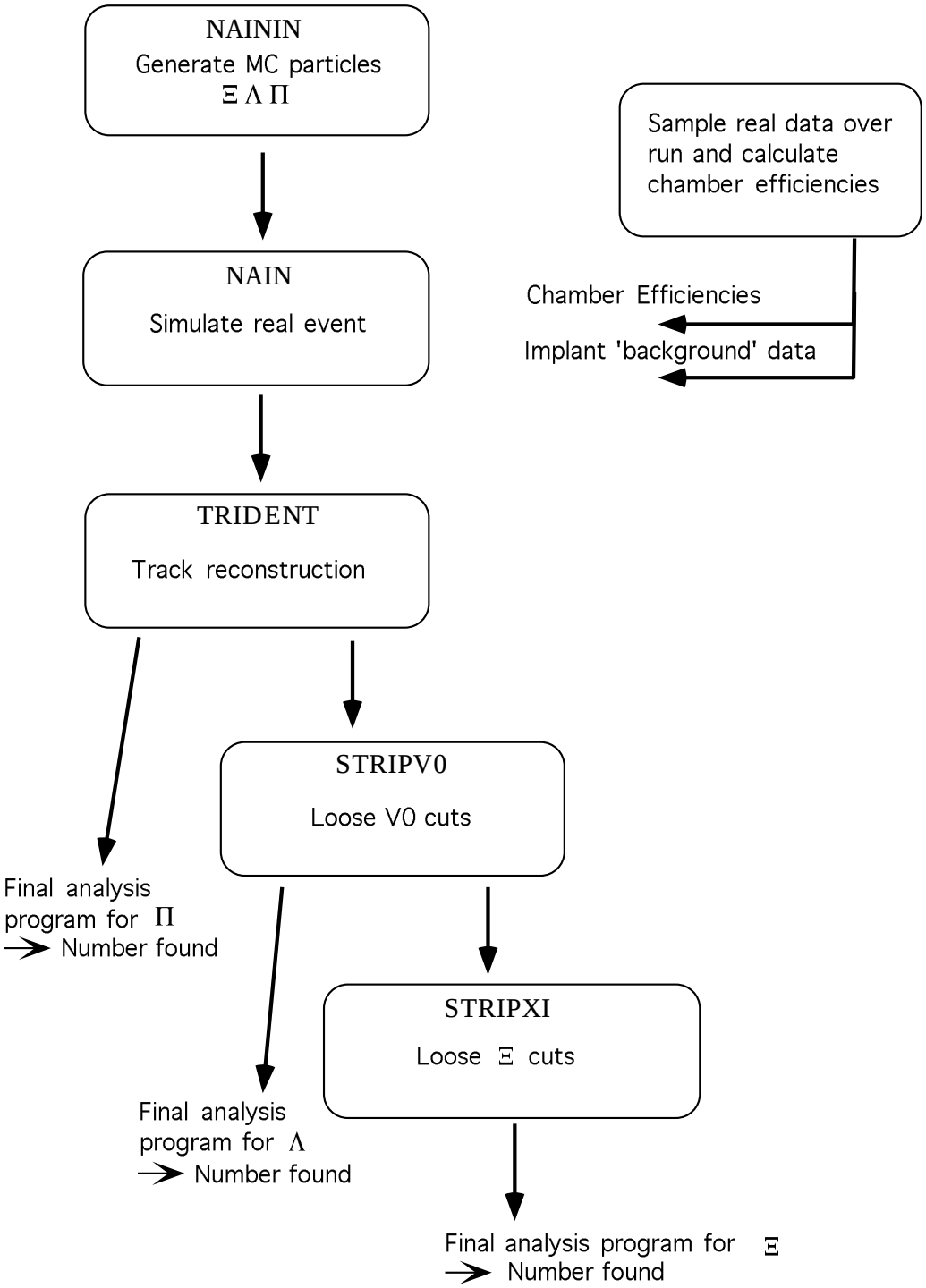

Figure 5.8: Schematic flow chart to illustrate the elements involved in the reconstruction efficiency chain.

mation relating to which kinematic region the decay lies in and whether the event satisfies 'all' the selection criteria applied to the real data is recorded.

Smearing

The generated particles kept by NAININ satisfy wider cuts, in terms of kinematics and spatial regions, than are applied in the final program of the analysis chain. This accounts for 'smearing' of variables, such as a vertex position or $y_{lab} - p_T$ coordinate of a decay, which stems from the momentum resolution of the detectors.

The second program used in the chain is called NAIN. Its job is to generate hits in the wire planes according to the positions of the Monte Carlo tracks and taking into account the chamber efficiencies.

Background Data

To simulate real events NAIN then implants the Monte Carlo events into real 'background' events; the end result is a Monte Carlo event resembling that of a real raw data event. As the reconstruction efficiency is derived as a function of planar cluster densities it is important to implant the Monte Carlo decay into a suitable background event. For example, if a level 2 Λ is generated by adding it to a real level 2 event, the total cluster multiplicities found would be significantly higher than those observed in the real data. The two tracks from a Λ will usually fulfill the trigger's prerequisite by satisfying the multiplicity condition asked for by the level 2 trigger. Hits are generated in the MWPCs according to the intercepts which a track makes with the A-chamber planes. The quadrant planar efficiencies are then consulted to determine whether a hit will be produced in this plane. The inter-wire distance is 2 mm, so to simulate a cluster of wire hits around this track intercept the following algorithm is used. If a track traces to a position of greater than a 1/3 of the wire pitch from its nearest wire then the wires on either side of the track impact are fired, if this is untrue then only the nearest wire will

fire. The wire hits from the real events are unpacked from the 21 A-chamber planes from the ROMULUS block, merged with the Monte Carlo hits and repacked into a new ROMULUS block containing the extra words. This is described in greater detail elsewhere [60, 61].

In addition, when generating level 2 type events the problem of FASTRO must be incorporated into the event. This is achieved by simply asking for the level 2 trigger requirements when the event has been repacked, using only those wires which were used in the trigger of the real run, see section 2.5. It is noted that, because only the flanks of chamber A4 are hindered by this problem, the losses of Λ and Ξ^- decays are about 1% to 2%. These losses have been investigated in detail and the results are presented in section 6.3. The output of NAIN events must be in an identical format to the raw data events so they can be treated in the same manner as the real data. This means that the combination of the background data event and Monte Carlo cluster hits must be written to tape in EPIO format as described in chapter 2.7. The events are then written out for TRIDENT to analyse.

5.2.2 Λ Reconstruction Efficiencies

As mentioned in the last section the particles are generated in a slightly larger acceptance window than that defined by the selection cuts in chapter 3. The Λs that pass the tighter final cuts are flagged. To accept a Λ both of its decay tracks must pass through the seven A chambers without the usual 1 cm edge cut to allow for smearing. In addition the following conditions must be satisfied to define a 'good' Λ:

- Λs are generated over the range of $0.7 \leq p_T \leq 3.3$ GeV/c in transverse momentum with an m_T distribution given by

$$\left(\frac{1}{m_T}\right)^{\frac{3}{2}} \frac{dN}{dm_T} \propto e^{-m_t\beta}$$

where β is determined from the real data when only corrected for acceptances. The relevance of this expression to the m_T distribution of the particles considered is examined in section 6.1. The final accepted decay must have a p_T in the region $0.8 \leq p_T \leq 2.9$ GeV/c.

- The generated rapidity distribution is flat in the region $2.2 \leq y_{lab} \leq 3.3$. The final Λs are accepted if their rapidity lies in the range $2.3 \leq y_{lab} \leq 3.0$. The rapidity is expected to be fairly flat over the narrow range of rapidity considered for Λs , and indeed most particles. The smearing of especially Λ and Ξ^- decay rapidities and transverse momenta, increases slightly as a function of rapidity and transverse momentum.

- The Λ is generated with a vertex between $-40 \leq x \leq 90$ cm. Vertex smearing increases with the distance of the decay from the A chambers.

- Finally, Λs are kept if one of their decay tracks traces to the hodoscopes, not necessarily within the 1 cm edge region defined inside the hodoscope, again to allow for smearing. There is also slight smearing on the high value of the α cut 0.6. The Λs are therefore generated with an alpha value of up to 0.65.

For each field direction approximately 10,000 Monte Carlo Λs are kept after all these cuts have been applied. The data are processed by TRIDENT, STRIPV0 and a final analysis program as for the real data. The Λ vertex distribution in x generated by NAININ is shown in figure 5.9 (a) and the final vertex distribution with all cuts applied is seen in figure 5.9 (b). In addition, the real Λ vertex distribution is superimposed on figure 5.9 (b), where the Monte Carlo plot has been normalised to the same number of events as in the real data. Figures 5.10 (a) and (b) show the mass distributions for real Λs and Monte Carlo Λs respectively at the end of the analysis chain. The efficiency is given by the number found at the end of the chain with respect

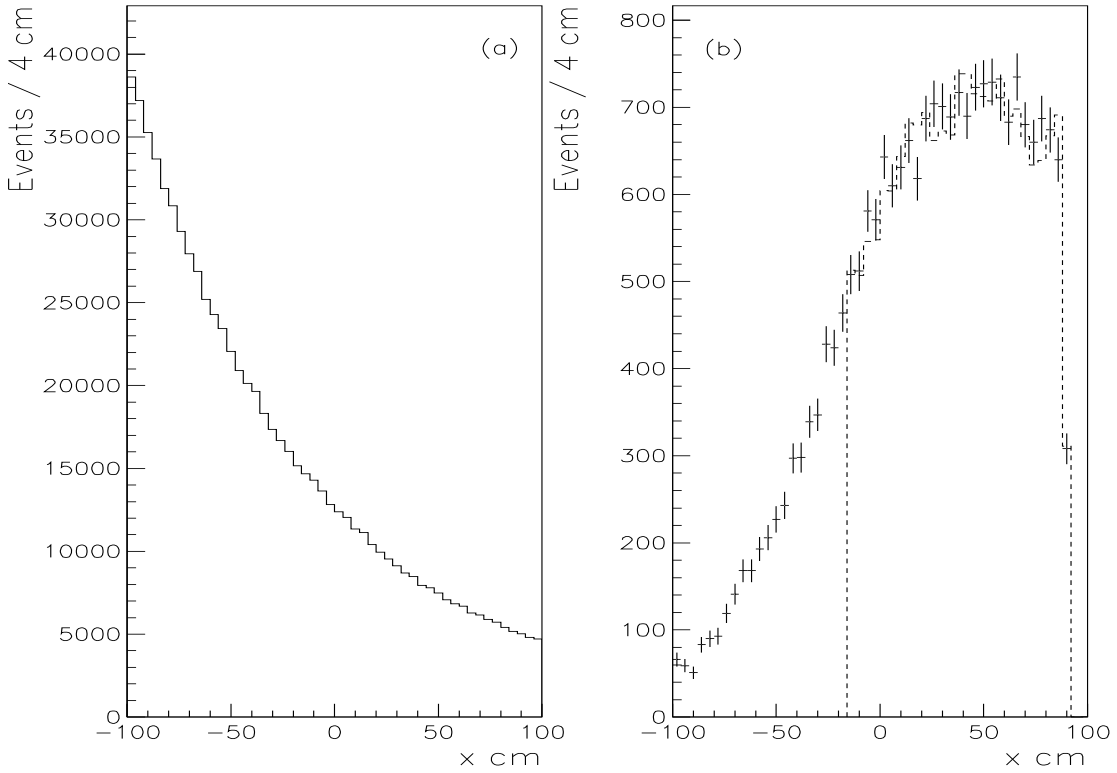

Figure 5.9: Vertex distribution in x of Monte Carlo (a) generated Λs ; and (b) Λs after the entire chain of analysis; superimposed is the real Λ vertex distribution.

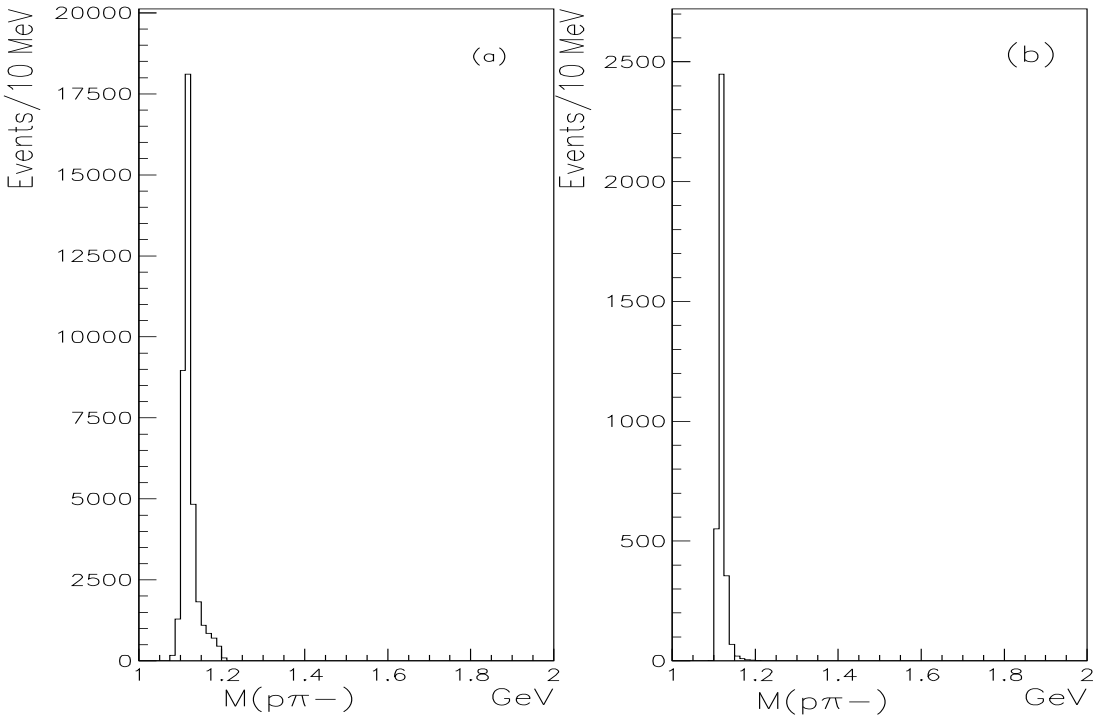

Figure 5.10: Effective mass distributions M($p\pi^-$) after the entire chain of analysis for (a) real data Λs ; and (b) Monte Carlo Λs .

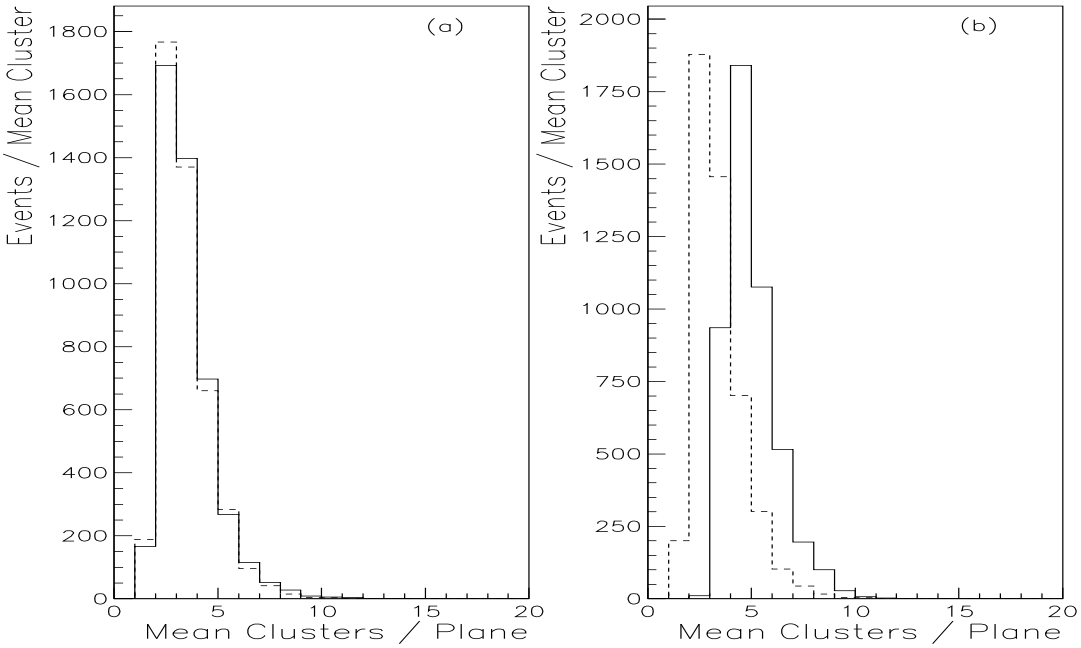

Figure 5.11: Monte Carlo mean planar multiplicity plots when implanted background is (a) Level 1; and (b) Level 2; superimposed is the real Λ multiplicity.

to the initial number given by

$$\textbf{Efficiency} = \frac{\mathbf{N_{Rec}}}{\mathbf{N_{Gen}}},$$

where $N_{\rm Gen}$ is the number of events which have been generated within the defined window of final cuts as discussed in section 3.1.2 and $N_{\rm Rec}$, the reconstructed events which survive the same cuts. It was found that the total efficiency for Λs was $77 \pm 1\%$ for field up and $78 \pm 1\%$ for field down and for $\overline{\Lambda}$s $78 \pm 1\%$ for field up and $79 \pm 1\%$ for field down. As already mentioned the reconstruction efficiencies are calculated as a function of the A-chambers' mean cluster multiplicity. So the data is corrected in this manner rather than a weighting based simply on the total efficiency. The mean multiplicity is determined by summing the total number of clusters in the 21 wire planes (3 planes $\times$ 7 A chambers) and dividing by 21. In figure 5.11 the cluster multiplicity distributions at the end of the analysis chain are shown for the case where Monte Carlo Λs have been merged with background from (a) level 1 and (b) level 2 data. This is to be compared with the equivalent distribution for the real data which has been superimposed upon both plots. It is clear that the level 1 event added to the Monte Carlo Λ seems to produce the best

approximation to the real Λ distribution and is chosen as the most suitable background. In addition, it is noted that most of the data lies in the region between one and six mean clusters per plane and indeed only data with up to eight mean clusters per plane is used in the final analysis. The efficiency as a function of multiplicity is given in figure 5.12 for (a) (H $\Downarrow$) Λs , (b) (H $\Downarrow$) $\overline{\Lambda}$s , (c) (H $\Uparrow$) Λs and (d) (H $\Uparrow$) $\overline{\Lambda}$s , where the arrows $\Downarrow$ and $\Uparrow$ denote the fields of down and up respectively. The efficiency has also been determined using level 2 events implanted as a background. This is shown in figure 5.13 for the $\Lambda \Downarrow$ case where the efficiencies using level 1 data as a background have been superimposed on the efficiencies with level 2 data implanted as a background. It can be seen that the highest efficiencies are shifted slightly towards higher mean multiplicities and the overall total efficiency is reduced by a few percent with the level 2 background. So the effect of using quite a different background is a minor one as far as the efficiencies are concerned.

5.2.3 Ξ^- Reconstruction Efficiencies

The Monte Carlo Ξ^- decays are generated in a similar manner to the Λ decays using the same procedure as in the acceptance determination.

It is required that the three charged tracks, which are the product of the Ξ^- decay, pass through the first four A chambers and fulfill the hodoscope condition. The following criteria must also be passed:

- Ξ^-s are generated over the p_T range of $1.1 \leq p_T \leq 3.3$ GeV/c with an m_T distribution given by

$$\left(\frac{1}{m_T}\right)^{\frac{3}{2}} \frac{dN}{dm_T} \propto e^{-m_t\beta}.$$

  The 'good' decay lies in the region $1.2 \leq p_T \leq 2.9$ GeV/c.

- The generated rapidity distribution is flat in the region $2.2 \leq y_{lab} \leq 3.3$. The final Ξ^-s are accepted if their rapidity lies in the range

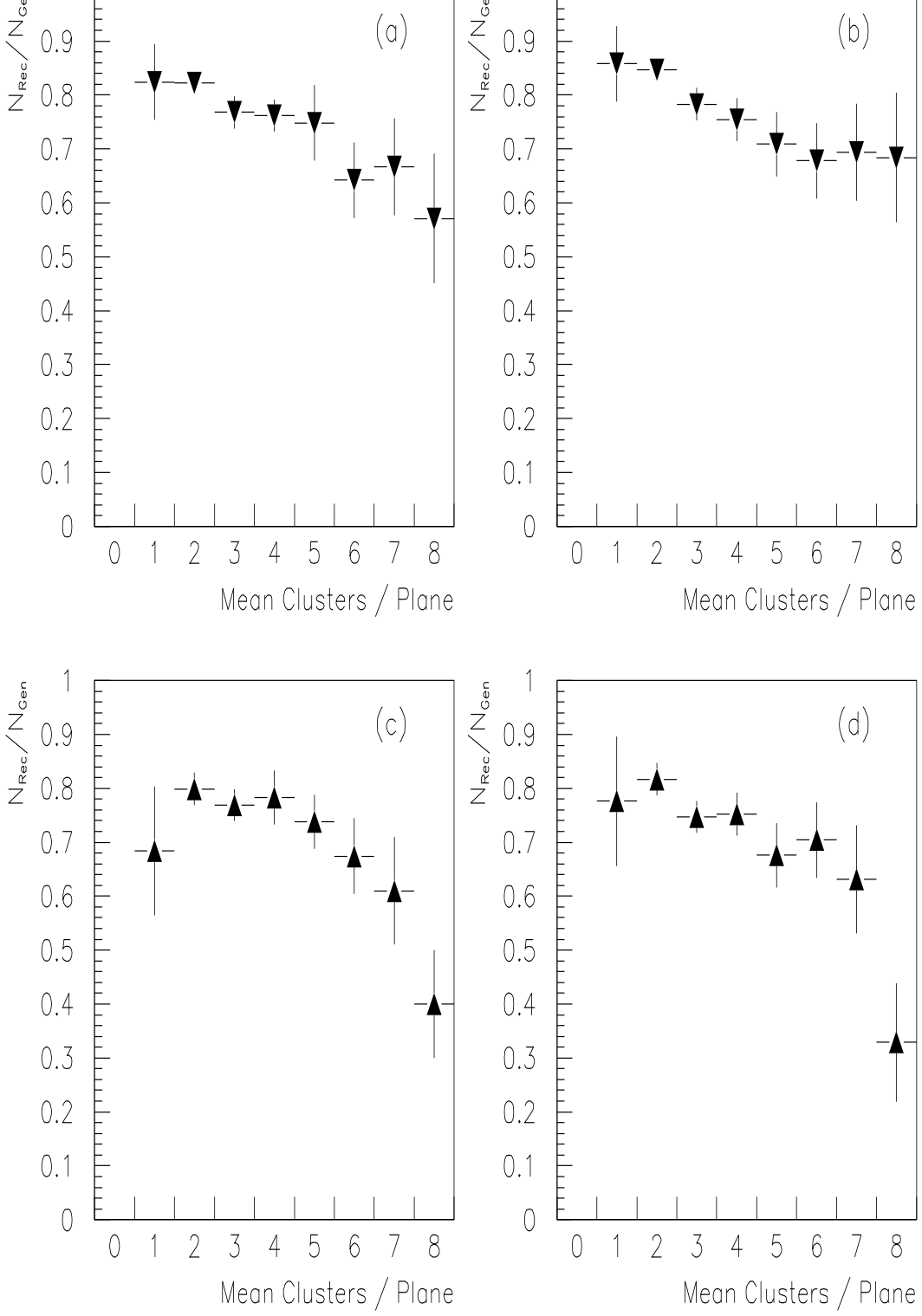

Figure 5.12: Reconstruction efficiencies as a function of the mean planar MWPCs multiplicity for (a) (H $\Downarrow$) Λs ; (b) (H $\Downarrow$) $\overline{\Lambda}$s ; (c) (H $\Uparrow$) Λs ; and (d) (H $\Uparrow$) $\overline{\Lambda}$s , all using level 1 as background.

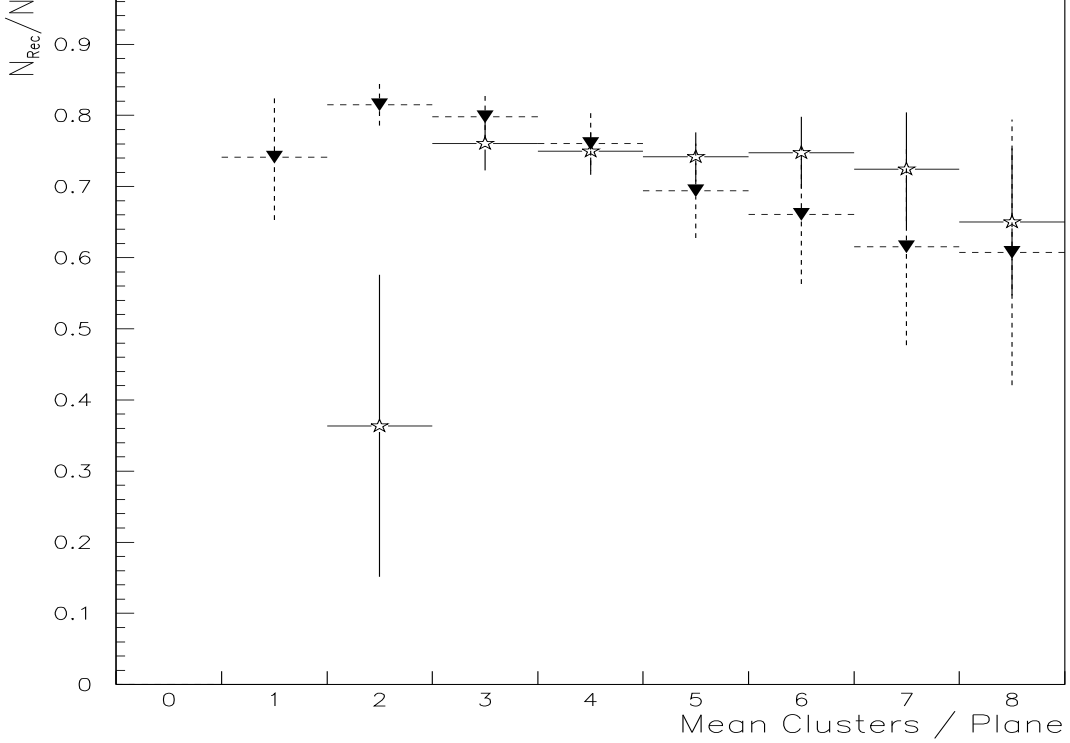

Figure 5.13: Reconstruction efficiencies as a function of mean planar MWPCs multiplicity for Λs with Level 2 background; superimposed (triangles) is the case where level 1 has been implanted.

$2.3 \leq y_{lab} \leq 3.0$.

- The Ξ^-s are generated with a vertex between $-70 \leq x \leq 90$ cm with a final cut of $-40 \leq x \leq 90$ cm.

- The Λ decay from the Ξ^- decay is asked to lie within the range -50 cm to 90 cm in x with a final selection requiring the vertex to lie in the region $-15 \leq x \leq 90$ cm.

- Lastly, it is required that one of the decay products of the Λ traces to the hodoscopes, but not necessarily within the 1 cm region.

14,000 Ξ^-s were kept for both field polarities in the region of cuts described.

The efficiency is determined in essentially the same manner as for the Λs , however after STRIPV0 has processed the data STRIPXI is used to look for Ξ^- candidates as described in section 3.2. The vertex distribution after generation and after the entire chain of analysis has been applied are shown in figures 5.14 (a) and (b) respectively; superimposed upon 5.14 (b) is the

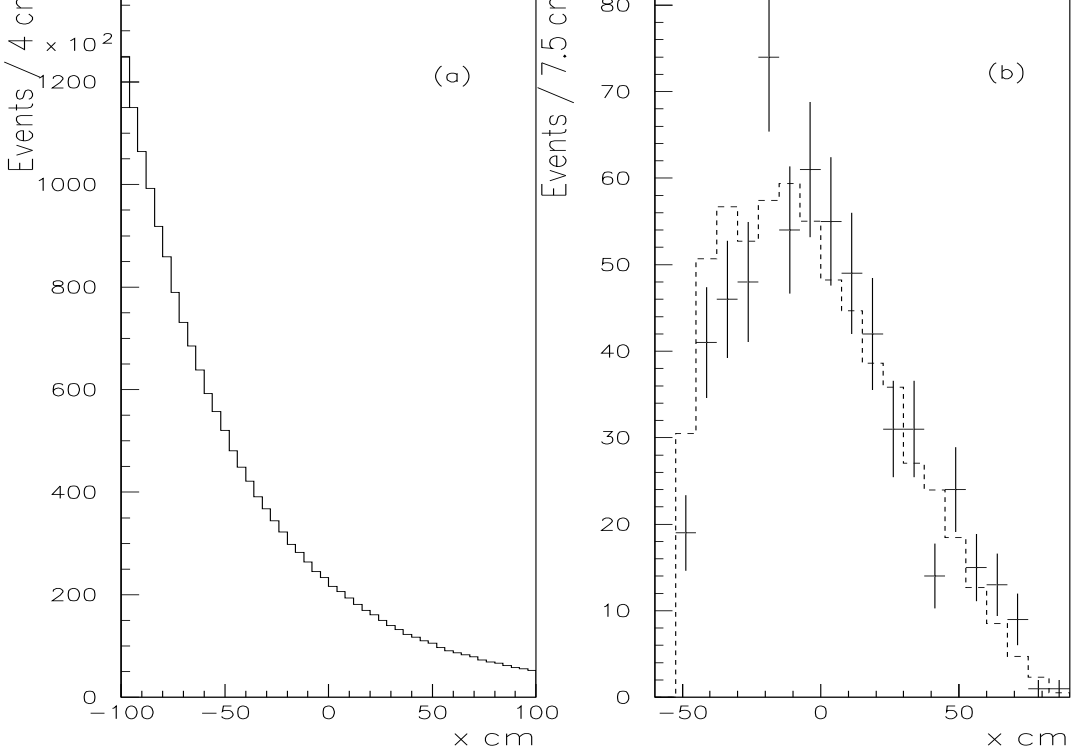

Figure 5.14: Vertex distribution of Monte Carlo (a) generated Ξ^-s ; and (b) Ξ^-s after the entire chain of analysis; superimposed is the real Ξ^- vertex distribution.

real Ξ^- data where the Monte Carlo data has been normalised to the real data statistics. The mass distribution for the real Ξ^-s is shown in figure 5.15 (a) and the Monte Carlo Ξ^- mass resonance is shown in figure 5.15 (b). The efficiencies again use level 1 data as the background.

The total efficiency for Ξ^-s was found to be 64 $\pm$ 1% for field up and 67 $\pm$ 1% for field down and for $\overline{\Xi^-}$s 65 $\pm$ 1% for field up and 67 $\pm$ 1% for field down. The efficiency distributions as a function of cluster multiplicity are given in figures 5.16 for (a), (b), (c) and (d) for field down and up for Ξ^-s and $\overline{\Xi^-}$s respectively.

5.2.4 π^- Reconstruction Efficiencies

In the case of the π^- efficiency calculation 25,000 'good' π^-s were generated for both fields after the following cuts. The π^- must trace through chambers A1 to A7 and satisfy the hodoscope condition as usual. The π^- is generated with a flat rapidity distribution in the range $2.2 \leq y_{lab} \leq 3.2$ and the same m_T distribution as for the Λ and Ξ^- decays in the transverse momentum region

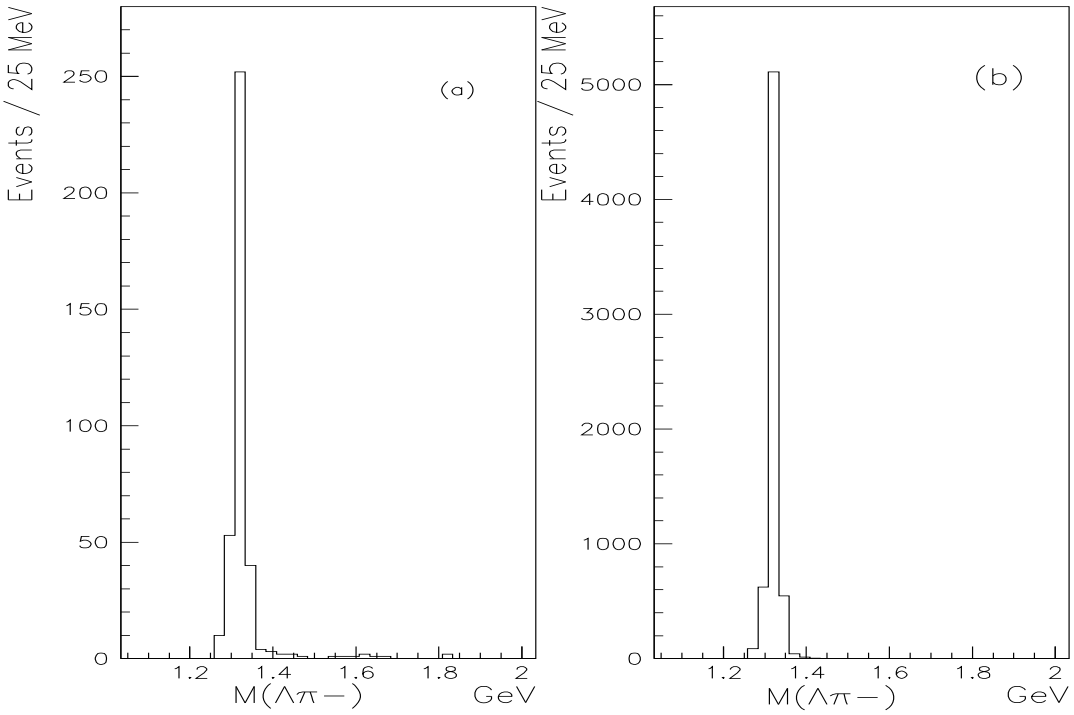

Figure 5.15: Effective mass distributions M($\Lambda\pi^-$) after the entire chain of analysis for (a) real data Ξ^-s ; and (b) Monte Carlo Ξ^-s .

0.6 GeV/c to 2.5 GeV/c. The smearing of both these kinematic parameters is reduced in relation to the smearing seen for the decays. In addition, the points of incidence on the chambers A1 and A7 are recorded for each Monte Carlo π^- track. This helps to ensure that in the final analysis program the Monte Carlo π^- is identified and not a background track.

The background used in the π^- case was that of data taken using only the interaction trigger. Level 1 data would be biased to too high a multiplicity, as is shown in figure 5.17. It is seen that the real h^-s multiplicity distribution compares well with the implantation of a Monte Carlo π^- into interaction level events. The total reconstruction efficiency was found to be 88 $\pm$ 1% and 89 $\pm$ 1% and are displayed in figures 5.18 (a) and (b), for the cases of field down and up respectively. In addition, shown in figure 5.18 (c) is the reconstruction efficiency as a function of multiplicity using π^-s implanted into interaction events, as usual, and superimposed with the higher multiplicity level 1 data used as a background, both in the field down case; there is a slight reduction in the efficiency when level 1 is used.

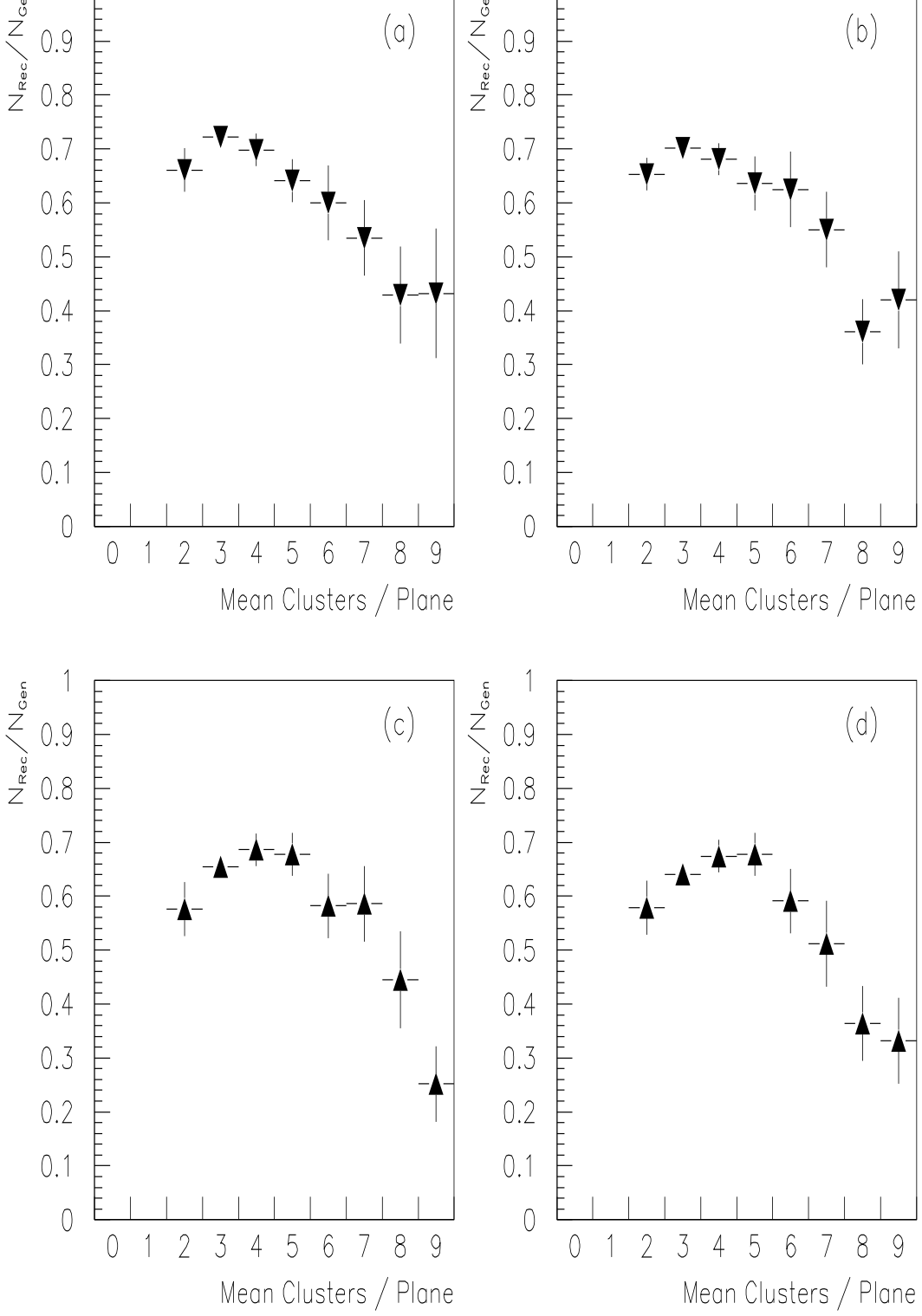

Figure 5.16: Reconstruction efficiencies as a function of the mean planar MWPCs multiplicity for (a) (H $\Downarrow$) Ξ^-s ; (b) (H $\Downarrow$) $\overline{\Xi^-}$s ; (c) (H $\Uparrow$) Ξ^-s ; and (d) (H $\Uparrow$) $\overline{\Xi^-}$s all using level 1 as background.

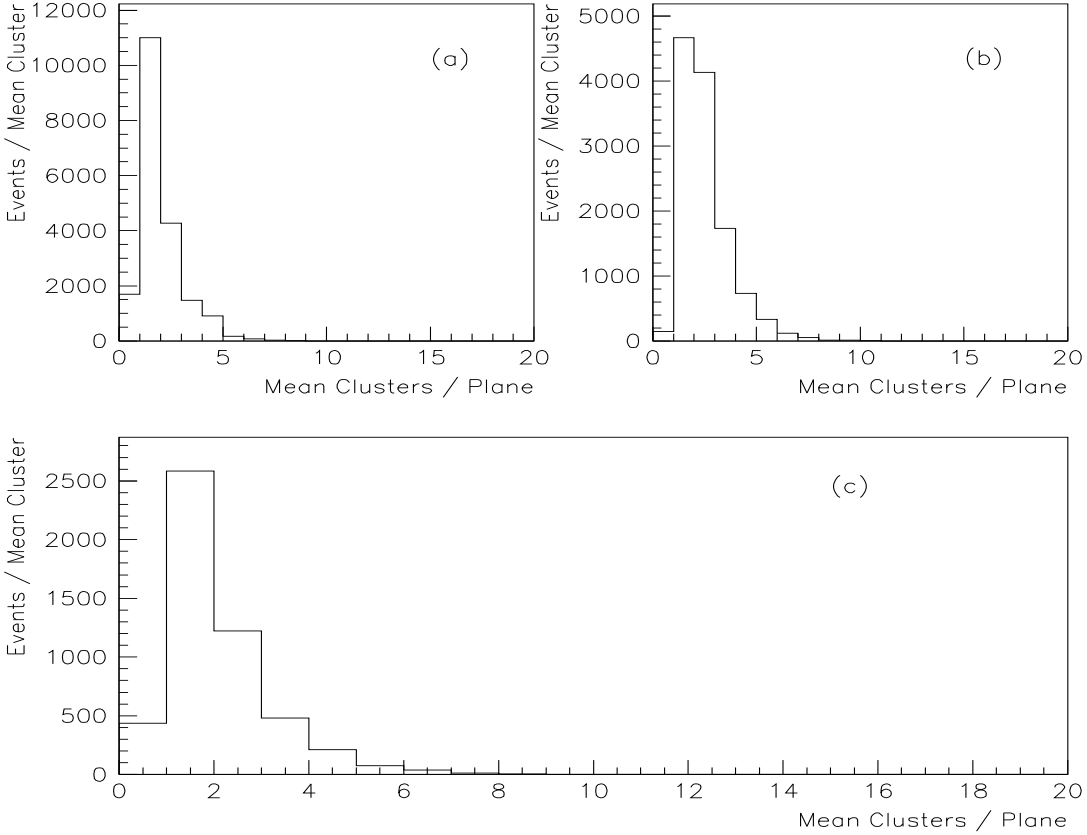

Figure 5.17: Multiplicity distribution for Monte Carlo π^-s using (a) Interaction triggered data; and (b) Level 1 data as a background. In figure (c) the real distribution for negatives is shown.

5.3 Summary

To compare the relative yields of different particle species directly, the acceptances and reconstruction efficiencies must be determined for the particles of interest. The acceptances have been well understood incorporating the hodoscope efficiencies, with typical acceptances in the 'good' region used for analysis of the order of 1% for Λs , K^0s and Ξ^-s and higher acceptances of about 15% for the π^- . This is a reflection of the large decay length cut applied to the data.

The chamber efficiencies calculated in the previous chapter have been used in the reconstruction efficiency calculation, providing a sensitivity to the physical characteristics of the detector, as well as the functioning ability of the software to reconstruct the particle of interest. The Λ efficiencies were found to vary slightly in the multiplicity region of highest statistics, namely

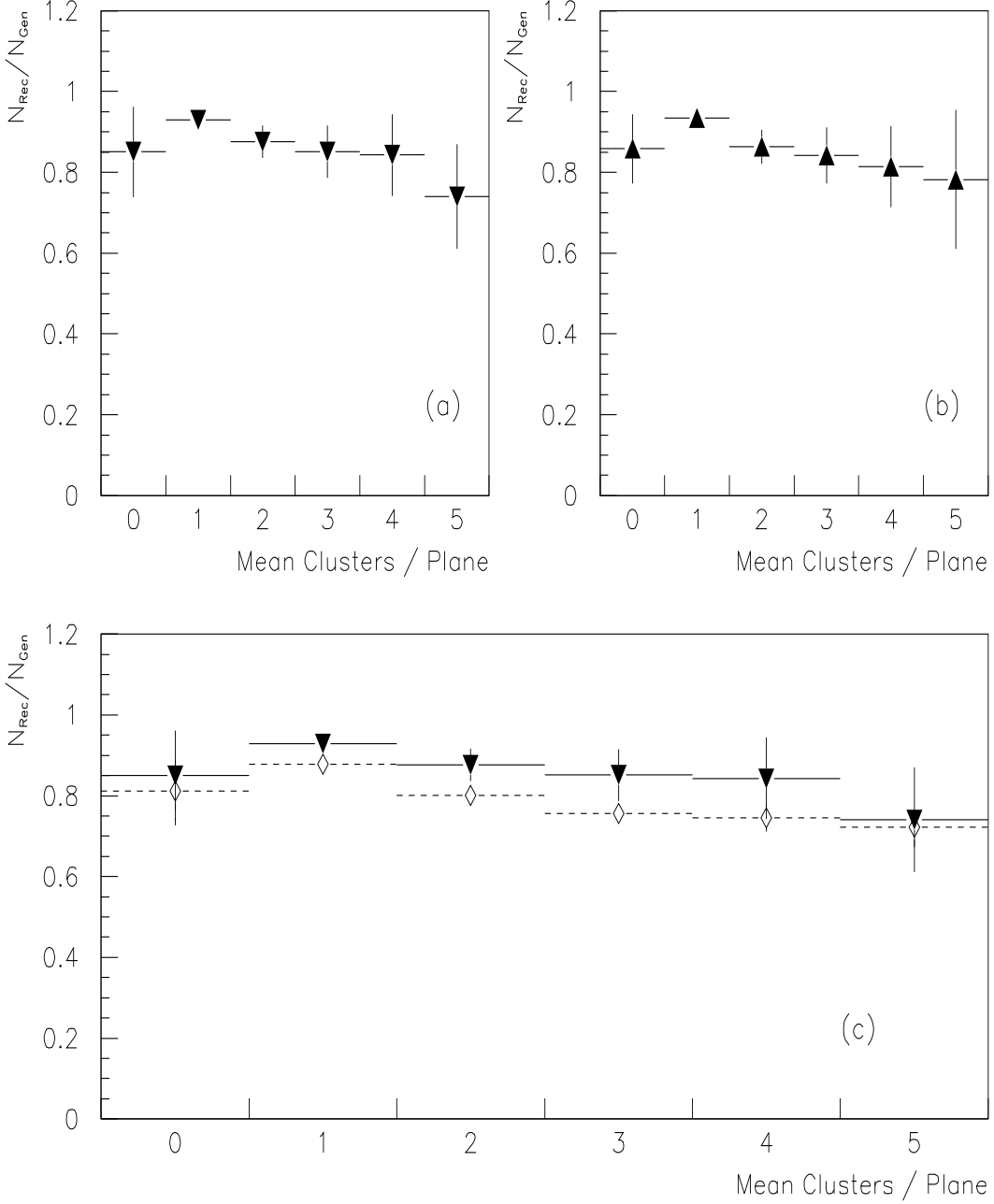

Figure 5.18: Reconstruction efficiencies as a function of the mean planar MWPCs multiplicity for (a) (H $\Downarrow$) π^-s ; and (b) (H $\Uparrow$) π^-s all using interaction data. In figure (c) the reconstruction efficiencies (H $\Downarrow$) π^-s with interaction data are shown with the level 1 background case superimposed (triangles).

of one to six mean clusters per plane with an overall efficiency of about 78%. The Ξ^- decay is harder to reconstruct, consisting of three tracks and two vertices. In the area of most statistics it was found to be about 65%. The π^- efficiencies are higher, just below 90%.

Chapter 6

Corrected Particle Ratios, m_T and y_{lab} Distributions

6.1 Introduction

The preceding chapters have centred upon the detection of different particle species ranging from doubly strange baryons and anti-baryons to the simple reconstruction of tracks. The limitation of the detector's phase space coverage and reconstruction software has been discussed at some length and this information will be used to determine the total 'corrected' production yields and kinematic distributions for the decays and negative particles considered. The main intention is to compare the yields of particles with different quark content, especially strangeness, so as to develop an understanding of the underlying processes which occur in the fireball created in a collision of two ions (NN). As has been mentioned, to extract such information a fuller understanding of the simpler hadron-nucleus (hN) system is desirable.

As well as considering the relative yield of various particles much enlightenment is provided by examining their kinematic spectra. The heavy ion community studies the transverse mass, m_T, distributions of different parti-

Figure 6.1: Thermal fit to the NA35 hadron spectra from 200 GeV/c per nucleon S-S interactions. The various spectra are normalised to each other at $m_T = m_o$, the mass of each particle.

cles. Transverse mass is considered instead of transverse momentum because it has been shown experimentally that the invariant cross section $1/({m_T}^n)$ dN/dm_T, where n is usually 1 or 3/2 as will be discussed shortly, is better represented by an exponential in m_T rather than in p_T [62]. The spectra of different particles are expected to be similar when plotted as a function of m_T, an effect known as 'm_T scaling'. However, when plotted as a function of p_T the particle slopes vary with mass. Indeed, the NA35 [63] plot in figure 6.1 illustrates that particles of differing masses will almost all fall on a universal straight line with a slight convex modulation when plotted as a function of m_T. The data were fitted with the following distribution,

$$\left(\frac{1}{m_T}\right)^{\frac{3}{2}} \frac{dN}{dm_T} \propto e^{-m_T\beta} \tag{6.1}$$

where the inverse slope $(1/\beta)$ provides information on the source temperature.

M_T scaling has been exhibited in certain models [64] where thermal equilibrium cannot be approached. However, if the particles are assumed to be produced thermally and they all have the same m_T slope, then they all origi-

nate from at least one source or multiple sources at the same temperature. It has been estimated that a system whose constituent particles undergo three or more collisions will approach thermalization [65] and so it is reasonable to expect the fireball created in a heavy ion collision to approach thermal equilibrium or indeed the centre of a hN reaction. The inverse slope $(1/\beta)$ though cannot be directly related to the temperature of the source due to other contributory factors, such as collective flow effects [66, 67], which relate to the expansion of the fireball and can result in an increase in the inverse slope. For example, correction for transverse flow effects has been estimated to shift the measured NA36 Λ inverse slope of 246 $\pm$ 14 MeV, derived from a p_T distribution, to a temperature of about 173 $\pm$ 10 MeV [68]. In addition, secondary scattering of the particles produced can lead to changes in the m_T slope.

Equation (6.1) is an approximation of the expression [41]

$$\frac{1}{m_T}\frac{dN}{dm_T} \propto \beta m_T K_1(\beta m_T),$$

where K_1 is the modified Bessel function [62]. Another approximate expression which is used is

$$\left(\frac{1}{m_T}\right)\frac{dN}{dm_T} \propto e^{-m_T\beta}.$$

However, the latter expression is better suited to an emitting source of fixed rapidity, whereas (6.1) is used for a range in flat rapidity, a better approximation for most experiments [1]. Above a value of $p_T \geq 1.0$ GeV/c the differences in the two inverse slopes using either expression is about 20 - 30 MeV.

Another useful parameter is rapidity. The distributions of particles in rapidity provide information on which fragmentation regions of the collision, such as the target or central fireball, tend to be responsible for the production of a particular type of hadron. WA85's rapidity coverage is much narrower

[1] this is especially true for a cooling system [67].

than other experiments so less information can be extracted by such a study, although these distributions are still worthy of consideration.

Before the relative yields of different particles and their kinematic spectra can be discussed in terms of a comparison between the p-W and S-W results some final corrections must be applied to the data and a review of some areas of systematic errors will be undertaken.

6.2 Correction for Feed-down

As well as the corrections made by the reconstruction efficiencies and acceptances, a correction to account for the contamination, of the 'true' Λ yield, from Λs which originate from cascade decays, is considered. This is known as *feed-down* and affects a large proportion of the Λ sample. The region in which a Λ is accepted is at least 140 cm from the target and most Ξ^-s will have decayed before traversing this distance. Furthermore, the Λ from the Ξ^- decay will carry the largest component of the cascades momentum as its mass is approximately 10 times that of the π^-. Therefore, the Λ will assume a similar line of flight to the Ξ^- and point back to the target.

To estimate this contamination Monte Carlo Ξ^-s are generated and merged with background data in the same manner as for the reconstruction efficiency calculation as discussed in section 5.2, using Ξ^-s which originate from the 'good' acceptance region. The data are then processed by TRIDENT, STRIPV0 and the final analysis program for Λ decays, which corrects the particles for acceptances and reconstruction efficiencies as if they were real Λs. The *feed-down* is found by the following equation

$$\text{contamination} = \frac{\mathrm{N}_{\Xi_{\mathrm{Real}}}}{\mathrm{N}_{\Xi_{\mathrm{Gen}}} \times 2} \times \frac{\mathrm{N}_{\Lambda_{feeddown}} \times 0.641}{\mathrm{N}_{\Lambda_{\mathrm{Real}}}}$$

where $\frac{N_{\Xi_{Real}}}{N_{\Xi_{Gen}}}$ normalises the Monte Carlo data to the real data in the same $y_{lab} - p_T$ window. The factor 2 is included to allows for the fact that the

Monte Carlo particles were generated only in the upper hemisphere and that the real Ξ^-s have been corrected for this; the factor 0.641 takes account of unseen decay modes. The contamination from Ξ^0s is calculated in the same manner for as for the Ξ^-s making the assumption that the production of Ξ^0s is equal to that of Ξ^-s. The contamination for Λs was found to be about 4% from Ξ^- decays and 7% from Ξ^0s. In the case of the $\overline{\Lambda}$s the calculation was carried out in the same manner and was found to be 8% from $\overline{\Xi^-}$ decays and 13% from $\overline{\Xi^0}$s. The contamination varies slightly with increasing transverse momentum, by a maximum of 0.5% in the range of p_T considered. The hodoscope level 1 trigger condition was found to reduce the contamination by about 1%. The feeddown from Ξ decays found in the S-W data was 19% for Λs and 34% for $\overline{\Lambda}$s .

6.3 FASTRO Level 2 Correction

In this section the effect of the FASTRO 'problem', discussed in section 2.5, upon level 2 decays is considered. The results of the earlier mentioned study are briefly reviewed below.

The FASTRO 'Problem'

The level 2 multiplicity trigger requirements were as follows:

$\geq$ 2 Hits in the Y plane of chamber A4

and

$\geq$ 2 Hits in 2 out of the first 3 Y planes of chambers A1, A2 or A3.

However, the edges of the Y plane of A4 were not used by FASTRO to determine the multiplicity on this plane. These regions are given below:

$$\text{Wires} \rightarrow 0 - 215$$

and

$$\text{Wires} \rightarrow 704 - 752.$$

As was mentioned in section 5.2.1 the loss of V^0s and cascades was not as large as first might have been thought. This can be checked using two algorithms. Firstly, Monte Carlo particles can be created according to the usual methods explained in chapter 5 for reconstruction efficiencies. Upon repacking the event with a suitable background in NAIN, the FASTRO condition was invoked to create a level 2 type event. To recreate the conditions of the experiment the appropriate wires were disabled. However, if the entire Y plane wires of A4 were used in the simulated trigger the loss of a certain type of particle can be determined. The losses for various particle types are given in table 6.1

Table 6.1: The number of Monte Carlo level 2 triggered decays with and without the disabled wires, using level 1 as the most suitable background.

Particle Type	Trigger Requirement		% Loss
	Level 2 'Normal Wires'	Level 2 'Disabled Wires'	
Λ & $\overline{\Lambda}$	20000	19715	1.4
Ξ^- & $\overline{\Xi^-}$	20000	19906	0.05

These losses are dependent upon the background chosen to be implanted into the Monte Carlo event. To determine the effect of using lower multiplicity backgrounds the same method was used with interaction data and no background at all. The losses only increased by up to 0.5%, illustrating that the multiplicity is dominated by a V^0 or cascade decay in the conditions typical of a p-W event. The 'no background' case represents a top limit on the losses of the data due to this problem.

Another examination of the losses was carried out by considering the real level 1 decays and how these numbers are affected by asking for the level 2 multiplicity requirements with and without the disabled wires. The reduction

is of a similar proportion to the losses seen in the studies carried out above and are given in table 6.2

Table 6.2: The number of real level 1 decays after asking for the level 2 requirements with and without the disabled wires.

Particle Type	Trigger Requirement		% Loss
	Level 2 'Normal'	Level 2 'Disabled'	
Real Λ & $\overline{\Lambda}$	1415	1392	2
Real Ξ^- & $\overline{\Xi^-}$	29	29	0

The data have been corrected for these losses. In addition, the effect of the FASTRO problem has been considered in terms of a $y_{lab} - p_T$ dependence which could have the effect of altering the m_T spectra. Monte Carlo decays were put through the entire reconstruction efficiency chain, re-analysed and corrected for acceptances. The data were then fitted with (6.1) using MINUIT [69]. This process was completed with the wires disabled and repeated with all the wires included in the level 2 simulation. The differences in the inverse slopes, $(1/\beta)$, were of the order of 0.1 MeV, which is much less than the error on the fit of 2 - 5 MeV for real V^0 s and 10 - 15 MeV for real cascade data, see section 6.6. The rapidity was found to be independent of the FASTRO problem for all decays.

6.4 Other Systematic Errors

As a final systematic check to ensure confidence in the corrected ratios and kinematic distributions some other areas of potential systematic errors must be considered.

The process used to reconstruct tracks and vertices using TRIDENT and the other analysis programs may well alter the values of the fitted m_T dis-

tributions [70]. Monte Carlo particles were generated in the normal manner with an m_T distribution given by 6.1 with an inverse slope of 200 MeV [2]. At the end of the analysis chain the re-corrected events are then fitted to the usual m_T slope; the results are shown in table 6.3.

Table 6.3: The systematic shifts in the inverse slopes of particles before and after having passed through the entire chain of analysis.

Particle Type	Generated Inverse slope MeV	Reconstructed Inverse slope MeV	Difference MeV
π^-	200	201 ± 1	$+1 \pm 1$
Λ	200	187 ± 2	-13 ± 2
Ξ^-	200	205 ± 2	$+5 \pm 2$

In addition, the effect of altering the y positions of the hodoscopes in the Omega coordinate system has been considered with a view to the m_T distribution and total yields of the h^-s. The motivation for such a study is the acceptance 'problem' encountered in section 5.1.3 for π^-. Pion tracks of a specific transverse momentum and rapidity were found to fail the hodoscope level 1 trigger condition, which required the track to pass through corresponding halves, RIGHT-RIGHT or LEFT-LEFT, of HZ0 and HZ1. An artificial shift in the positions of the two hodoscopes was made in order to study the effect of small misalignments. One trial, for example, shifted HZ0 by 0.5 cm and HZ1 by -0.5 cm in y, see figure 6.2. This was an exaggerated shift compared to the expected misalignments of about 1 mm, as observed in section 4.2.1. The acceptance table was recalculated and the real h^-s data was corrected using the new acceptances, but with the normal 'correct' hodoscope positions. When the cut in rapidity ($2.3 \leq y_{lab} \leq 3.0$) included

[2] the effect of the shift on the inverse slope after the chain of analysis is relatively independent of the starting value of the inverse slope.

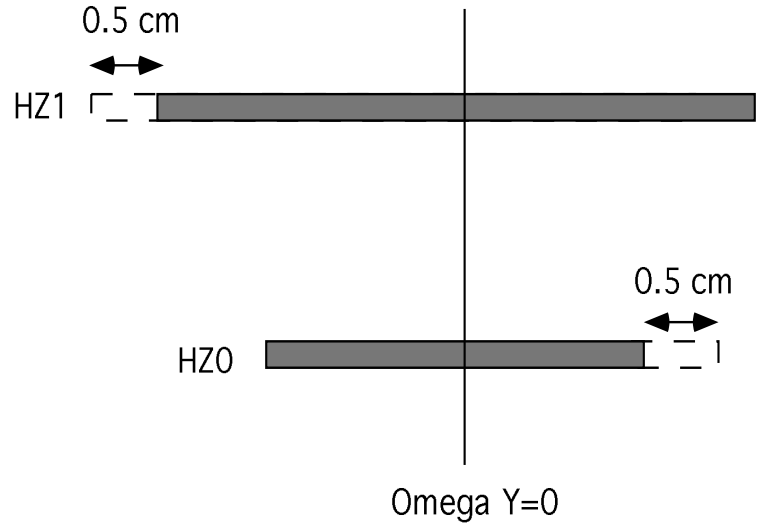

Figure 6.2: Shift in the y coordinate of HZ0 and HZ1 positions to determine the maximal error in acceptance which could be reflected in the m_T spectra and final ratios for h^-s.

that of the 'bad' region the total yields differed by about 1% and the shift in the inverse slope was of the order of 0.1%. In the final analysis the minimum cut in rapidity was made at 2.4 not 2.3 and the systematic error was found to diminish further.

6.5 Corrected Particle Ratios

The raw particle yields for Λs, $\overline{\Lambda}$s, Ξ^-s, $\overline{\Xi^-}$s, K^0s and h^-s are shown in table 6.4.[3] The table encompasses data taken from p-W level 2 events, where 28,996,441 good triggers were used and for level 1 events which constitute 21,552,695 good triggers. The kinematic region within which the uncorrected particle yields lie is $0.8 \leq p_T \leq 2.9$ GeV/c and $2.3 \leq y_{lab} \leq 3.0$ ($2.5 \leq y_{lab} \leq 3.0$ for the K^0 decays). The h^-s lie in the same rapidity range, but a wider transverse momentum window of $0.7 \leq p_T \leq 2.9$ GeV/c and are taken from

[3]ambiguous Λs and $\overline{\Lambda}$s satisfy the cut $0.45 \leq \mid \alpha \mid \leq 1.0$ and unambiguous Λs and $\overline{\Lambda}$s satisfy the cut $0.45 \leq \mid \alpha \mid \leq 0.6$.

568,213 (2.6% of the data) level 1 triggers sampled throughout the run. All the data have been corrected for reconstruction efficiencies, acceptances and, where appropriate, for the small losses due to the level 2 trigger problem. The Λ decays have been corrected for feed-down. It is also noted that the reconstruction efficiencies were determined in the exact window of kinematics used for a certain particle ratio, because slight variations in the efficiencies were seen for different kinematic cuts. For the rest of the analysis only unambiguous Λs are used.

Table 6.4: Raw yields of V^0s, cascades and h^-s observed in the 1990 p-W run.

Particle	Trigger Level	Raw Yield
Λ	Level 2	31,114 (ambiguous)
		13,841 (unambiguous)
$\overline{\Lambda}$	Level 2	8,715 (ambiguous)
		3,467 (unambiguous)
Λ	Level 1	2,628 (ambiguous)
		1,154 (unambiguous)
$\overline{\Lambda}$	Level 1	742 (ambiguous)
		304 (unambiguous)
Ξ^-	Level 2	294
	Level 1	24
$\overline{\Xi^-}$	Level 2	136
	Level 1	6
K^0	Level 2	8,537
	Level 1	681
h^-	Level 1	40,240

Table 6.5: Relative hyperon yields in p-W and S-W interactions ($2.3 < y_{lab} < 3.0$, $1.2 < p_T < 3.0$ GeV/c).

Ratio	p-W Interaction	S-W Interaction
$\overline{\Lambda}/\Lambda$	0.20 ± 0.02	0.196 ± 0.011
$\overline{\Xi^-}/\Xi^-$	0.47 ± 0.07	0.47 ± 0.06
Ξ^-/Λ	0.070 ± 0.006	0.097 ± 0.006
$\overline{\Xi^-}/\overline{\Lambda}$	0.16 ± 0.02	0.23 ± 0.02

6.5.1 Cascade and V^0 ratios

Relative hyperon ratios of Ξ^-s to Λs and their charge conjugate partners have been obtained in three kinematic windows as a direct comparison with the published WA85 S-W ratios [71]. The ratios comparing Ξ^-s to Λs in the region of highest statistics are presented in table 6.5. In this case the acceptance region used is where the Ξ^- and Λ 'good' acceptances overlap as illustrated in figure 6.3; the region used for the particle ratio calculation is the dashed and shaded areas; it is very similar to the region of shared Ξ^- and Λ acceptances in the S-W data.

The dashed region is where the acceptances exactly conform to the rule that they must not vary by a factor of greater than 10 from the maximum value of acceptance used, as mentioned in section 5.1.3. The multi(anti)strange to (anti)strange ratios calculated in the dashed region alone, when compared to the dashed and shaded regions, were found to alter by up to 2%. In addition, the tighter cut in rapidity, $2.5 \leq y_{lab} \leq 3.0$, was applied and resulted in minimal changes to the ratios, still well within the statistical errors which dominate the multistrange to strange ratios.

Theoreticians prefer to parameterize the ratios in terms of the transverse mass rather than the transverse momentum of the particles [72]. A cut

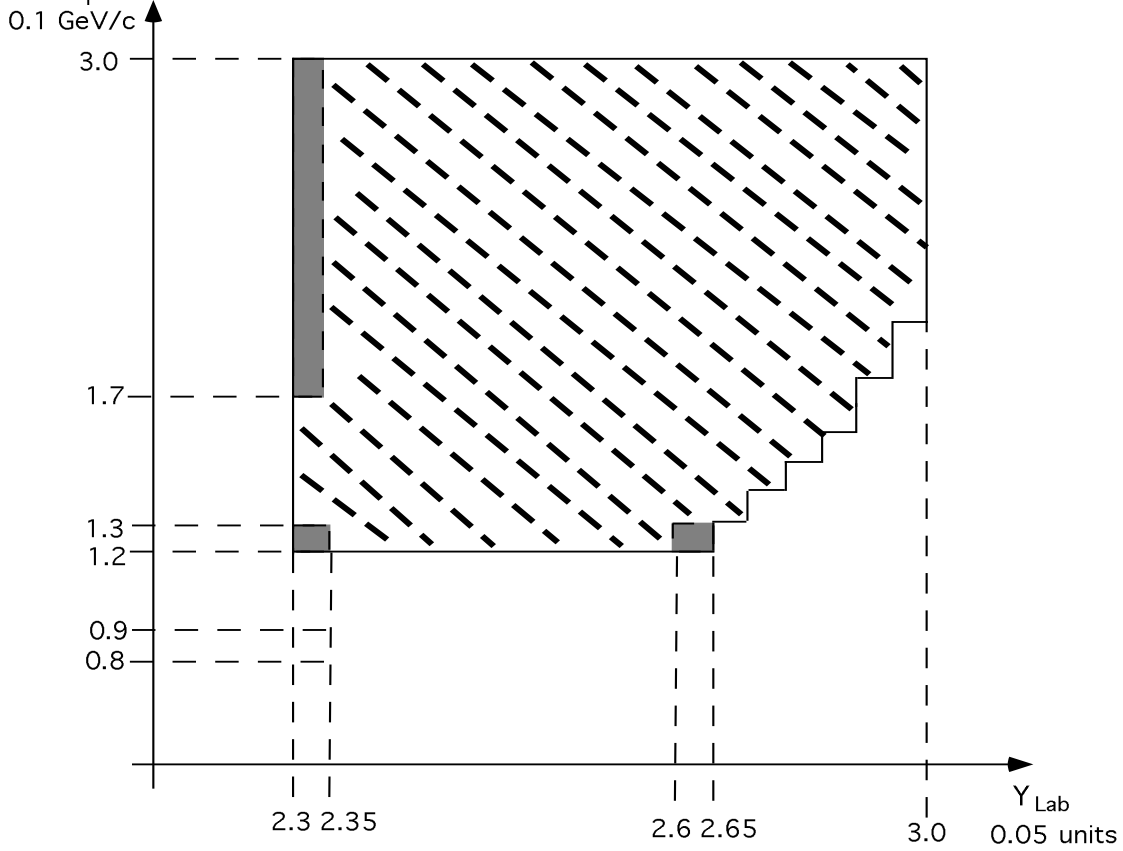

Figure 6.3: The region of 'good' acceptance overlap for Λ and Ξ^- decays. The dashed region is the area where there is no variation greater than a factor of 10 of the maximum acceptance in this region..

of $m_T \geq 1.9$ GeV is the lowest possible which considers data within the same region of rapidity for both Λ and Ξ^- decays. The ratios for this cut are given in table 6.6. For both sets of results the particle to anti-particle ratios are compatible when comparing p-W and S-W data. However, there is an increase of about 30% in the ratio of multi(anti)strange to (anti)strange baryons when going from p-W to S-W interactions. The difference in these ratios corresponds to about a two standard deviation effect.

To enable a comparison of the results with those from other experiments, the ratios have been determined within the region $1 \leq p_T \leq 2$ GeV/c and $2.3 \leq y_{lab} \leq 2.8$. These are shown in table 6.7 and represented in graphical form in figure 6.4, along with the comparable results from WA94 (S-S) [4]

[4]the WA94 ratio in S-S interactions is obtained in a similar centre-of-mass rapidity interval, which corresponds to $2.5 \leq y_{lab} \leq 3.0$.

Table 6.6: Relative hyperon yields in p-W and S-W interactions ($m_T > 1.9$ GeV, $2.3 \leq y_{lab} \leq 2.8$.)

Ratio	p-W Interaction	S-W Interaction
$\overline{\Lambda}/\Lambda$	0.19 ± 0.02	0.20 ± 0.01
$\overline{\Xi^-}/\Xi^-$	0.45 ± 0.07	0.43 ± 0.05
Ξ^-/Λ	0.13 ± 0.01	0.17 ± 0.01
$\overline{\Xi^-}/\overline{\Lambda}$	0.32 ± 0.05	0.38 ± 0.04

Table 6.7: Relative hyperon yields in p-W and S-W interactions ($2.3 \leq y_{lab} \leq 2.8$, $1 \leq p_T \leq 2$ GeV/c).

Ratio	p-W Interaction	S-W Interaction
Ξ^-/Λ	0.072 ± 0.010	0.09 ± 0.01
$\overline{\Xi^-}/\overline{\Lambda}$	0.13 ± 0.02	0.21 ± 0.03

[73] and the AFS (p-p) ratio for $\overline{\Xi^-}/\overline{\Lambda}$ (0.06 ± 0.02) [74]. The ratios in this window for the WA85 results rely on an extrapolation from 1.3 GeV/c to 1.0 GeV/c in p_T for the Ξ^- data. The error on this result is therefore larger than the ratios calculated in the other two kinematic windows. The $\overline{\Xi^-}/\overline{\Lambda}$ ratio in p-W interactions is approximately double that found in p-p interactions, which corresponds to a two standard deviation effect. There is a 40% increase in the S-W ratio when compared with that of the p-W value in this window; this difference is also a two standard deviation effect.

So far little theoretical work has been carried out in the area of multi-strange baryonic production and none in the case of hN interactions. Recently the advent of string event generator models has provided an opportunity to consider this topic. These simulators attempt to reproduce all the parton level processes in a dense ion collision. Whilst the backbone of these

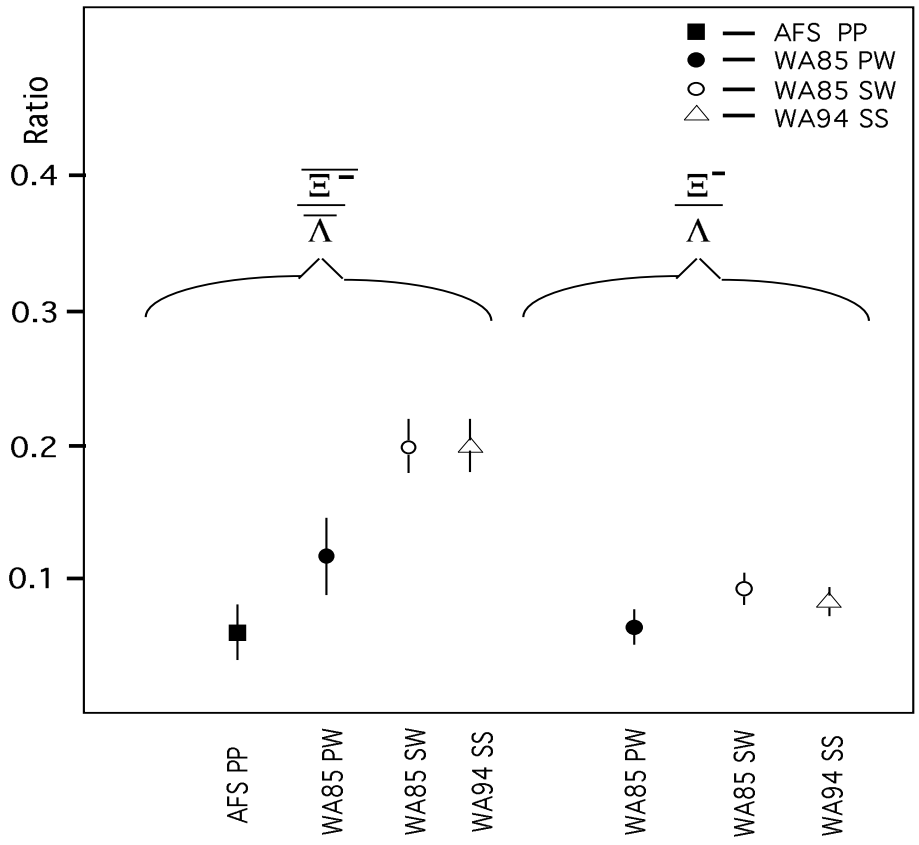

Figure 6.4: Ξ^-/Λ and $\overline{\Xi^-}/\overline{\Lambda}$ ratios for WA85, WA94 and AFS p-p.

simulators is proton-proton collisions, they allow some level of re-interaction of the constituent particles, resonance production and in some cases a coalescence mechanism, such as colour rope formation [75], string fusion [76], or quark droplet formation [77].

At present the RQMD technique [5] [75] has been used to consider the production of baryons and mesons with a strangeness content of one in a variety of reactions. Figure 6.5 illustrates the RQMD fit to the NA35 Λ and $\overline{\Lambda}$ data taken from p-Au collisions at 200 GeV/c [75]. The nice agreement between the real and simulated data has been made possible by the inclusion of essentially two major factors which do not occur in hadron-hadron (hh) interactions. Firstly, re-interaction of the particles produced inside the target nucleus is added to the model. The results of RQMD suggest however, that

[5] RQMD is an abbreviation of 'Relativistic Quantum Molecular Dynamics'.

Figure 6.5: Comparison between RQMD calculations (histograms) and NA35 data for the rapidity distributions of Λ (left) and $\overline{\Lambda}$ (right) produced in minimum bias reactions p-Au at 200 GeV/c.

a second mechanism, namely string fusion in the form of coloured ropes, is an important factor in antibaryon production. This is further illustrated by figure 6.6 where the inclusion of colour ropes produces a good agreement between the NA35 S-S rapidity spectra and RQMD. Baryonic yields are less dominated by colour rope fragmentation, because their production has a large component from rescattering, which is not hindered as greatly by annihilation as in the case of antibaryons. It is noted that the $\overline{\Lambda}$ distribution is peaked at the region of central rapidity for the p-Au and S-S interactions. However, the Λ distributions are biased towards target fragmentation rapidities. Much care must therefore be taken whenever any comparison is made of ratios which exist within different kinematic regions.

Recently, RQMD considered S-W interactions at 200 GeV/c per nucleon for Ξ^- and Λ decays; the findings agreed well with the WA85 S-W results [78]. The RQMD rapidity spectra for the Ξ^-s tended to be more centrally peaked than that of the Λs. The production of a Ξ^- by initial scattering

Figure 6.6: Comparison between RQMD calculations (histograms) and NA35 data for the rapidity distributions of Λ (top) and $\overline{\Lambda}$ (bottom) produced in central S-S collisions at 200 GeV/c per nucleon. The left hand figures include secondary rescattering in the RQMD calculation as well as primary production and in addition, the right hand figures includes rope formation.

of the projectile and target nucleon is less likely when compared with that of Λ production in the same process. These effects could be expected to be reflected in the p-W data. Unfortunately, the study has not yet been extended to include cascade production in hN interactions.

To conclude, the understanding of the underlying mechanisms involved in strange baryonic production, even at the level of hN reactions, is certainly very complex and care must be taken in the interpretation of results. It has been seen that at least three mechanisms are needed to reproduce the experimental results.

6.5.2 V^0 and h^-s Ratio

Ratios have been calculated for Λs to h^-s , where the h^-s are interpreted as π^-s. The π^-s cannot be corrected for contamination from sources such

Table 6.8: Relative Λ to h^- yield in p-W interactions.

Kinematic region	Ratio
$0.8 \leq p_T \leq 3.0$ GeV/c $2.3 \leq y_{lab} \leq 3.0$	0.093 ± 0.004
$1.0 \leq p_T \leq 2.0$ GeV/c $2.3 \leq y_{lab} \leq 2.8$	0.116 ± 0.006
$1.2 \leq p_T \leq 3.0$ GeV/c $2.3 \leq y_{lab} \leq 3.0$	0.15 ± 0.01

as K^-s or anti-protons, however this is estimated to be between 5% and 10%. Other experiments have found this order of contamination [79]. The ratio Λ/h^- has been calculated in three windows of p_T and are given in table 6.8. The first ratio is taken from a region where the 'good' acceptance of the Λ and h^- data overlap; this provides the region of greatest statistics. The second region is obtained from the m_T distributions and the third uses the same kinematic region of acceptance overlap for Λ and xi decays used to determine the hyperon ratios given in table 6.5. The results reflect the bias towards a higher average p_T for the Λ decays compared to the h^-s. In the region of greatest statistics for both sets of data, the m_T inverse slope for the Λ is higher than that for the h^-.

6.6 m_T distributions

The data were plotted in the same region of central rapidity as the S-W results *i.e.* $2.3 \leq y_{lab} \leq 2.8$ for Λ, Ξ^- and h^- particle types and $2.5 \leq y_{lab} \leq 3.0$ for K^0s. Equation (6.1) was used to fit the m_T distributions. The fitted distributions are shown in figure 6.7. The inverse slopes ($1/\beta$) are shown in table 6.9 with the corresponding values published for WA85 S-W data [71].

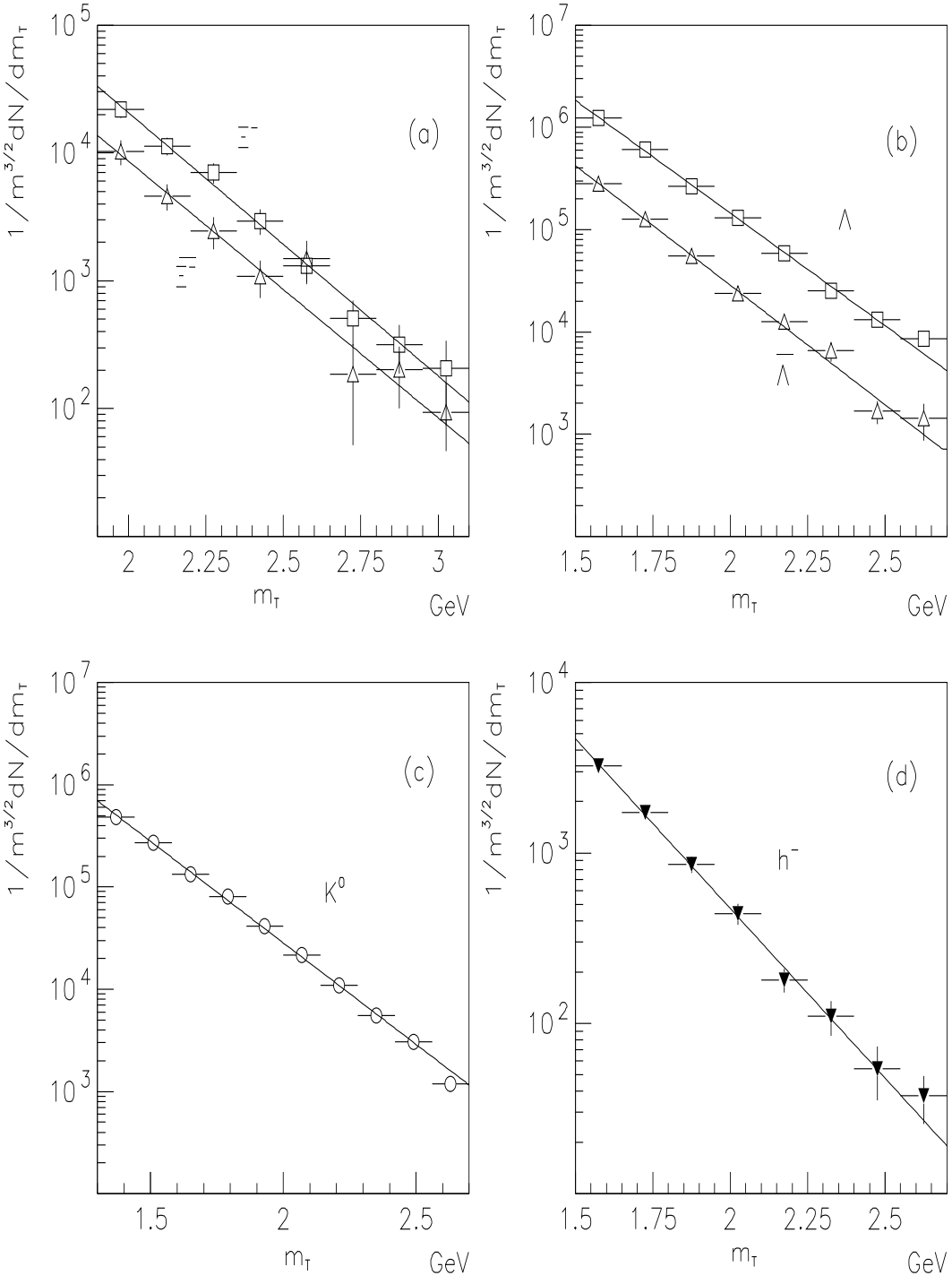

Figure 6.7: Transverse mass distributions for (a) Cascades; (b) Λs ; (c) K^0s ; and (d) h^-s.

Table 6.9: Inverse slopes of hyperons in p-W and S-W interactions.

Particle	p-W Interactions	S-W Interactions
	Inverse slope (MeV)	
Λ	$197 \pm 2 \ +13$	233 ± 3
$\overline{\Lambda}$	$185 \pm 5 \ +13$	232 ± 7
Ξ^-	$211 \pm 14 \ -5$	244 ± 12
$\overline{\Xi^-}$	$216 \pm 21 \ -5$	238 ± 16
h^-	217 ± 7	–
K^0	224 ± 3	219 ± 5

The errors shown for both sets of data are statistical. The fits to the inverse slopes also contain a systematic error estimated to be $\pm$ 10 MeV. For all the p-W inverse slopes, except the K^0 inverse slope, a systematic shift has been calculated, as was discussed in section 6.3. There was no shift in the case of the h^- data.

As can be seen the inverse slopes of the Λ and $\overline{\Lambda}$ decays are similar to the cascade inverse slopes, when corrected for their shifts, and are compatible with being in the range of 200 MeV to 210 MeV. The K^0 inverse slope is slightly higher than those of the hyperons. All the hyperon inverse slopes are lower than those of the S-W data, which are compatible with 230 MeV. The slopes taken from the h^-s are slightly higher than those for the Λs and $\overline{\Lambda}$s, in the same kinematic window [6]. In the region of $p_T \geq 1.5$ GeV/c π^-s are known to suffer an 'anomalous enhancement' which was discovered by Cronin *et al* [80]. At these high transverse momenta an excess of π^-s in hN and NN collisions was found which could be parameterised by a power law in the atomic number of the target and projectile masses. The understanding

[6] the cascade fits are taken in a region of higher m_T due to acceptance limitations. This is believed to make little difference to the overall fit for such particles of greater mass [80].

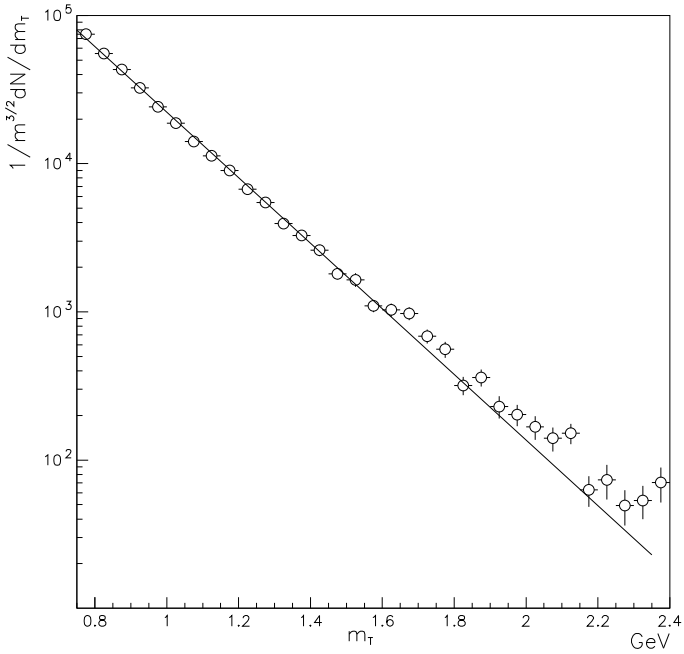

Figure 6.8: Transverse mass distribution for h^-s over the whole range of good acceptance; the fit over this range in m_T illustrates a flattening of the slope at the highest end of the m_T range.

of such an excess is still not completely clear, but explanations vary from secondary scattering of the π^- to multiple initial parton scattering [62, 63]. A study was undertaken to consider how the inverse slope varies in different m_T windows. Figure 6.8 shows the m_T distribution over the whole range of m_T, where fits have been made to the inverse slope over regions of successively higher m_T. These inverse slope fits are given in table 6.10. The data show a significant flattening of the slope as the m_T range is shifted towards higher values. In addition, the data were not found to vary with rapidity over the central region that WA85 is concerned with. WA85 internal studies [81] have shown that a 10% contamination from K^-s or anti-protons will only alter the fit by 1 to 2 MeV. Some inverse slopes found in other hN experiments of comparable energies [79] are given in table 6.11. The NA35 V^0 inverse slopes taken from p-Au are quite similar to those found in p-W WA85 data, however the p-S V^0 inverse slopes are lower. The region of rapidity considered

Table 6.10: Inverse slopes of h^-s in p-W interactions over different ranges in m_T for a rapidity cut of $2.4 \leq y_{lab} \leq 3.0$.

Kinematic Region (GeV)	Inverse slope (MeV)
$0.75 \leq m_T \leq 1.2$	182 ± 2
$0.75 \leq m_T \leq 1.6$	189 ± 1
$0.75 \leq m_T \leq 2.0$	194 ± 1
$0.75 \leq m_T \leq 2.4$	196 ± 1

by NA35 is wider *i.e.* $1 \leq y_{lab} \leq 5$ than WA85's rapidity coverage as they attempt to cover the target and rapidity regions as well and they concentrate on a lower transverse mass window.

6.7 Rapidity Distributions

As discussed in section 6.1 the rapidity spectra can provide useful information on the production mechanisms for different particles. WA85 is not ideally suited to studying this parameter owing to its selective window of coverage. The acceptance falls off quite quickly for Λ and $\overline{\Lambda}$ decays at low p_T and high y_{lab}. This restricts the region of rapidity coverage for the V^0 decays to $2.3 \leq y_{lab} \leq 2.8$. Figures 6.9 (a) and (b) show the rapidity distributions for Λs and $\overline{\Lambda}$s respectively, after a cut of $p_T \geq 1.2$ GeV/c has been applied. Figures 6.9 (c) and (d) show the same plots after a cut of $p_T \geq 1.3$ GeV/c has been applied. The effect of the second more restrictive p_T cut on the shape of the rapidity distributions is small, reflecting that fact the data being considered are well within the region of good acceptance. The rapidity distribution for the h^-s is shown in figure 6.10. Even within this restricted window some general points can be made with respect to the shape of the rapidity

Table 6.11: Inverse slopes for different hN experiments all fitted with 6.1.

Experiment	Particle Type	Kinematic Region	Inverse slope (MeV)
NA35 p-S 200 GeV/c	Λ	$1.1 \leq m_T \leq 2.3$ GeV $0 \leq y_{lab} \leq 5$	182 ± 17 MeV
	$\overline{\Lambda}$	$1.1 \leq m_T \leq 2.3$ GeV $0 \leq y_{lab} \leq 5$	132 ± 22 MeV
	K^0	$0.50 \leq m_T \leq 2.06$ GeV $0 \leq y_{lab} \leq 5$	205 ± 16 MeV
NA35 p-Au 200 GeV/c	Λ	$1.1 \leq m_T \leq 2.3$ GeV $1.4 \leq y_{lab} \leq 5$	215 ± 12 MeV
	$\overline{\Lambda}$	$1.1 \leq m_T \leq 2.3$ GeV $1.4 \leq y_{lab} \leq 5$	175 ± 20 MeV
	K^0	$0.50 \leq m_T \leq 2.06$ GeV $2.2 \leq y_{lab} \leq 5$	210 ± 15 MeV

distributions. The Λ and $\overline{\Lambda}$ distributions behave differently from the h^-s distribution; the latter is flat, while the former distributions fall off at higher rapidities. The results seem consistent with what has been observed by other experiments [75, 82].

6.8 Summary and Conclusions

WA85 has successfully reconstructed Ξ^-, $\overline{\Xi^-}$, Λ, $\overline{\Lambda}$, K^0, K^+ and K^- decays in the difficult environment of S-W interactions. Now, Ξ^-, $\overline{\Xi^-}$, Λ, $\overline{\Lambda}$ and K^0 decays have been reconstructed in p-W interactions and form an interesting comparison with the ion data. The success of the trigger in the p-W run has

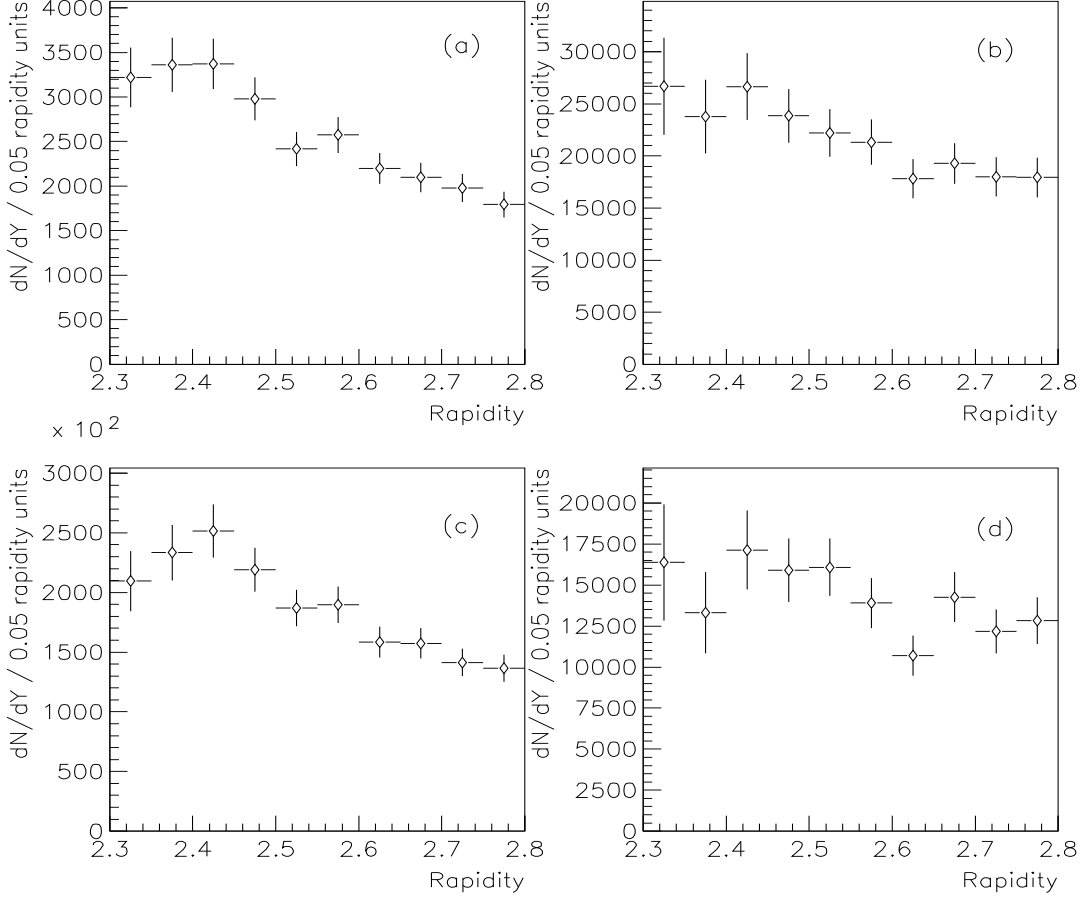

Figure 6.9: The rapidity distributions with $p_T \geq 1.2$ GeV/c for (a) Λs; and (b) $\overline{\Lambda}$s and with $p_T \geq 1.3$ GeV/c for (c) Λs; and (d) $\overline{\Lambda}$s.

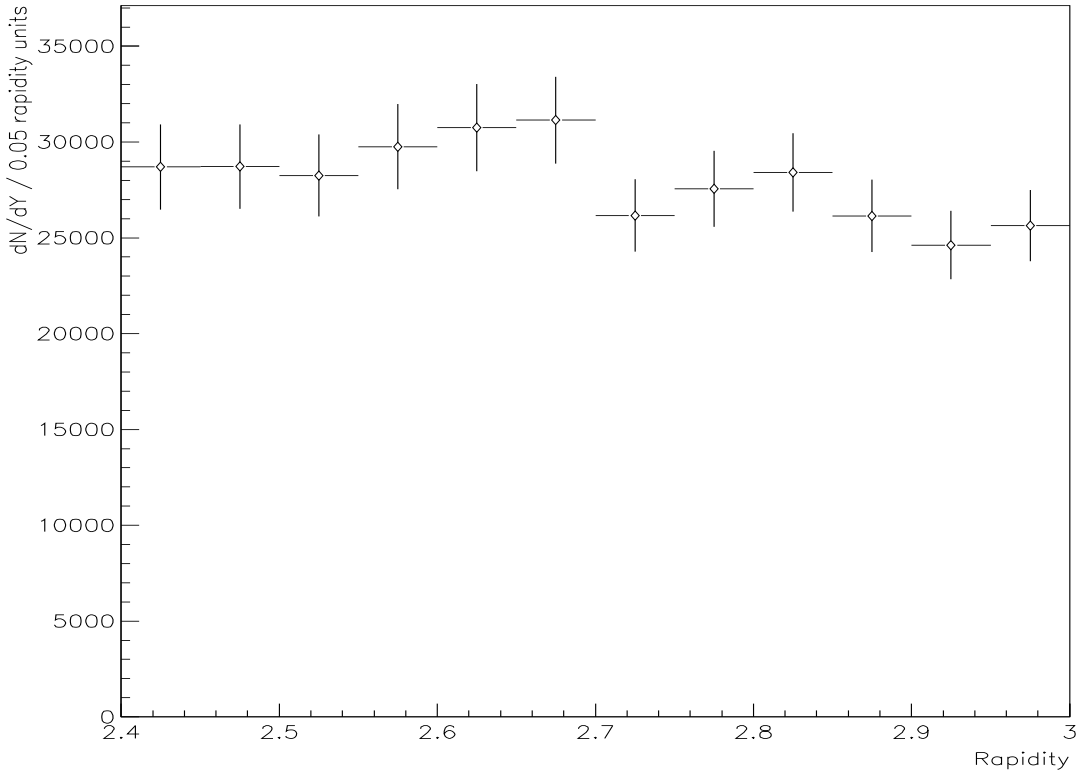

Figure 6.10: The rapidity distribution for h^-s.

allowed sufficient statistics to be obtained so as to report a 30% increase in the ratios of $\overline{\Xi^-}/\overline{\Lambda}$ and Ξ^-/Λ when going from p-W to S-W reactions. The difference in these ratios corresponds to a three standard deviation effect, in some kinematic windows. This gives some credence to the assertion that the hyperons are being produced by different mechanisms in the two reactions.

If we assume that the particles are emitted from a source which is approaching thermal equilibrium then the hyperon m_T spectra show that the proton induced events are being produced from a source at lower 'temperature' than those from the sulphur data. However, this statement is really too simplistic, because it is expected that there will be greater collective effects in the ion interactions, which generally tend to increase the observed inverse slopes [67]. In addition, the h^- inverse slope has illustrated the well known Cronin effect in the proton-tungsten data.

The experiment WA94 has successfully continued the program started by WA85. So far the data taken by the WA94 1991 S-S run have followed a similar trend in terms of ratios (see section 6.5) and m_T spectra to that of the S-W data. The 1993 p-S data is at present under analysis and will prove very interesting in the light of the new p-W results. Following these two experiments is WA97 which collides Pb-Pb and p-Pb at 160 GeV/c per nucleon and is in some ways a pre-cursor to the Pb-Pb experiment at the LHC called ALICE (A Large Ion Collider Experiment) [83]. The WA97 Pb-Pb and p-Pb runs will be even more interesting to compare and should show even greater differences in their strangeness production. The first WA97 run took place during November and December of 1994 and is being followed by a similar run this autumn.

At this time the nature of the discussion has been quite speculative. Hopefully the development of string models will bear further light upon the significance of the ratios of multistrange to strange baryons leading to a greater understanding of the underlying mechanisms involved in hadron-nucleus interactions and heavy ion interactions.

Appendix A

Stopping Power

Numerous methods have been employed to estimate the stopping of the participant nuclear matter in the collision between two ions.

The transfer into transverse energy of the beam energy is considered. The transverse energy distribution is shown for various targets using data from the HELIOS experiment [84] and E802 [85] in figure A.1. It provides information upon the impact parameter of the interaction and the number of nucleons participating in the reaction. Indeed, the area of plateau corresponds to the region where the interaction between the two ions is central, as in figure 2.1.

The quantitative definition of *Stopping Power* is given as

$$S = E_T/E_T^{max},$$

where E_T is the observed transverse energy and

$$\begin{aligned} E_T^{max} &= (\pi/4)E^{max}, \\ E^{max} &= s^{1/2} - m_N(N_p + N_T), \end{aligned}$$

where $s^{1/2}$ is the centre of mass energy, m_N the nucleon mass, N_p and N_T are the number of projectile and target nucleons respectively. The HELIOS experiment, which uses the SPS, suggests a maximum stopping of up to 80% for many different collisions [86].

Figure A.1: Transverse energy distribution for various targets using (a) data taken by the HELIOS experiment, which used a 200 GeV/c per nucleon S beam and (b) data taken by the E802 collaboration, which collided Si-Al, Cu, Ag, Au at 14.6 GeV/c per nucleon.

Another method used to study stopping is by considering the shift in the rapidity distribution of protons. Before the collision all of the nucleons exist exclusively at the target and beam rapidities. After the collision the participants will be shifted towards centre of mass rapidities. The greater this shift the more 'opaque' the collision is.

S_p, the *stopping parameter*, can be calculated by

$$S_p = \frac{< \Delta y_{projectile} >}{y_{beam} - y_{centre\ of\ mass}}$$

where $< \Delta y_{projectile} >$ is the mean rapidity shift for the projectile protons which is extracted from the rapidity distribution. The rapidities are all calculated in the laboratory frame.

Using this formula NA35 [87] has found the stopping parameter to be 57% for S-Au at 200 GeV/c, compared with 61% for the E814 collaboration [88] who collide Si-Pb at 14.6 GeV/c. Further analysis of the E814 data supports the scenario of high stopping, which could indicate that the stopping at the

energies of the SPS is higher than 60% to 70% as was mentioned in section 1.3. However, the importance of the rapidity region considered in the transverse mass calculation is vital to the final result.

The situation concerning the definition of stopping is still unsure, although the results suggest that, as expected, the stopping is greater for the AGS energies than those at the SPS, but for both the stopping is significant.

Appendix B

Crossing distance of V^0 decay tracks

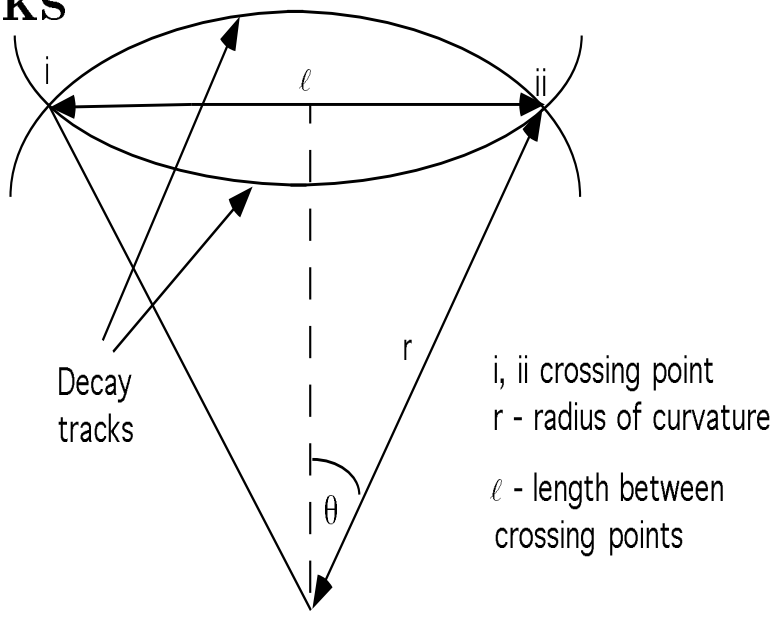

Figure B.1: Crossing paths of two V^0 decay tracks.

Figure B.1 shows the paths of V^0 decay tracks crossing at points i or ii, either of which may be the real vertex. The distance between these crossing points is given by ℓ, where ℓ is defined by

$$\sin\theta \;=\; \frac{\ell}{2\mathrm{r}}, \tag{B.1}$$

where r is the radius of curvature of the particle in a magnetic field, B and is calculated using the following equation

$$\begin{aligned} \mathrm{Bev} &= \frac{\mathrm{Mv}^2}{\mathrm{r}} && \text{(B.2)} \\ \Rightarrow \mathrm{r} &= \frac{\mathrm{p}}{\mathrm{Be}}, && \text{(B.3)} \end{aligned}$$

where p is the momentum of the track. For small θ

$$\begin{aligned} \sin\theta &\simeq \tan\theta && \text{(B.4)} \\ \Rightarrow \sin\theta &\simeq \frac{\mathrm{q_T}}{\mathrm{q_L}}. && \text{(B.5)} \end{aligned}$$

So $\sin\theta$ and therefore ℓ will be at a maximum when $\mathrm{q_T}$ is at its largest and since $\mathrm{q_T} = \mathrm{p}^*\cos\theta, \mathrm{q_{Tmax}} = \mathrm{p}^*$. For $\Lambda \rightarrow \mathrm{p}\pi^-$, $\mathrm{p}^* = 0.1$ GeV/c and for K^0 decays $\rightarrow \pi^-\ \pi^+$, $\mathrm{p}^* = 0.2$ GeV/c and as the decay tracks have momenta, p, of several GeV/c, $\mathrm{p} \gg \mathrm{p}^* \Rightarrow \mathrm{q_L} \simeq \mathrm{p}$.

Therefore using equation B.5

$$\Rightarrow \sin\theta_{\mathrm{max}} \simeq \frac{\mathrm{p}^*}{\mathrm{p}}. \qquad \text{(B.6)}$$

Hence from equations B.1, B.3 and B.6 the maximum crossing distance, ℓ_{max}, is given by,

$$\begin{aligned} \ell_{\mathrm{max}} &\simeq 2\left(\frac{\mathrm{p}}{\mathrm{Be}}\right) \times \left(\frac{\mathrm{p}^*}{p}\right) && \text{(B.7)} \\ \Rightarrow &= \frac{2\mathrm{p}^*}{\mathrm{Be}} && \text{(B.8)} \end{aligned}$$

and in metres

$$\begin{aligned} \ell_{\mathrm{max}} &\simeq \frac{2\mathrm{p}^*(\mathrm{GeV/c})}{\mathrm{B(T)e}} \times \frac{10^9\mathrm{e}}{c} && \text{(B.9)} \\ \Rightarrow &= \frac{2\mathrm{p}^*(\mathrm{GeV/c})}{0.29979\mathrm{B(T)}}. && \text{(B.10)} \end{aligned}$$

As B = 1.8 Tesla for WA85

- $l_{max} \simeq 40$ cm for Λs,
- $l_{max} \simeq 80$ cm for K^0s.

Appendix C

Podolanski Armenteros Plots

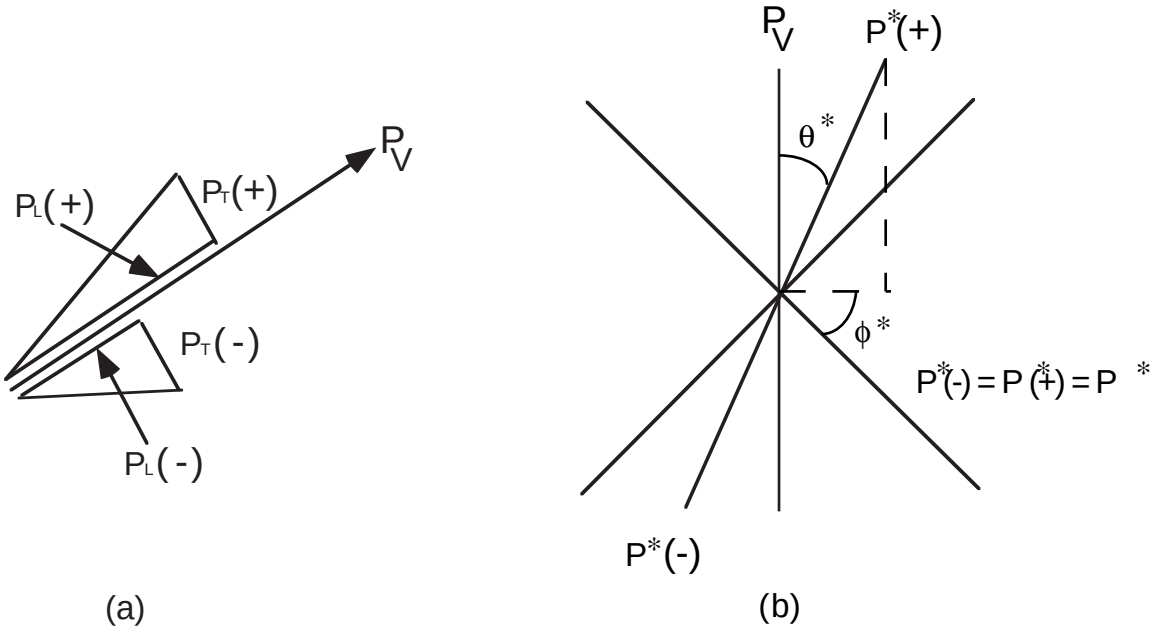

Figure C.1: Schematic representation of a V^0 decay in a) the lab frame and b) the centre of mass frame of the V^0 decay.

Figure C.1 (a) illustrates a V^0 decay into a positive and negative particle. The tracks have momentum components, $p_L(+)$ and $p_L(-)$, in the direction of motion of the V^0 and transverse momentum of p_T. In the centre of mass frame, (figure C.1 (b)) the momentum components are thus,

$$p_L^*(+) = p^* \cos\theta,$$

$$p_T^*(+) = p^* \sin\theta,$$
$$E^*(+) = \sqrt{p^{*2} + m^2(+)}.$$

To transform to the lab frame one uses Lorentz transformations, which in matrix form are given by [7]

$$\begin{pmatrix} E \\ p_L \end{pmatrix} = \begin{pmatrix} \gamma & \gamma\beta \\ \gamma\beta & \gamma \end{pmatrix} \begin{pmatrix} E^* \\ p_L^* \end{pmatrix}, \qquad p_T^* = p_T$$

where $\gamma = 1/\sqrt{1-\beta^2}$ and β is the velocity of the lab in the particles rest frame. This gives

$$E^{Lab}(+) = \gamma E^*(+) + \gamma\beta p_L^*(+)$$
$$p_L^{Lab}(+) = \gamma p_L^*(+) + \gamma\beta E^*(+) = \gamma p^* \cos\theta^* + \gamma\beta E^*(+)$$
$$p_T^{Lab}(+) = p_T^*(+) = p^* \sin\theta^*$$

i.e.

$$p_L^{Lab}(+) = \gamma p^* \cos\theta^* + \gamma\beta E^*(+)$$
$$p_L^{Lab}(-) = -\gamma p^* \cos\theta^* + \gamma\beta E^*(-)$$

therefore

$$p_L^{Lab}(+) - p_L^{Lab}(-) = 2\gamma p^* \cos\theta^* + \beta\gamma(E^*(+) - E^*(-))$$
$$p_L^{Lab}(+) + p_L^{Lab}(-) = p_L^{Lab} = \beta\gamma m_V^0.$$

The Podolanski Armenteros variable, α, is defined by [59]

$$\alpha = \frac{p_L^{Lab}(+) - p_L^{Lab}(-)}{p_L^{Lab}(+) + p_L^{Lab}(-)} = \frac{2p^* \cos\theta^*}{\beta m_V^0} + \frac{E^*(+) - E^*(-)}{m_V^0} = \zeta \cos\theta^* + \varphi$$

therefore

$$\cos\theta^* = \frac{\alpha - \varphi}{\zeta} \qquad \sin\theta^* = \frac{p_T^*}{p^*}$$
$$\cos^2\theta^* + \sin^2\theta^* = 1 = (\frac{\alpha - \varphi}{\zeta})^2 + (\frac{p_T^*}{p^*})^2.$$

This is an equation of an ellipse with centre (φ,0) and semi axis in α of length ζ, and in p_T length p^*. Table C.1 shows the value of these variables for the decays of Λs, $\overline{\Lambda}$s and K^0s, whilst the theoretical plots for Λs, $\overline{\Lambda}$s and K^0s are shown in figure C.2.

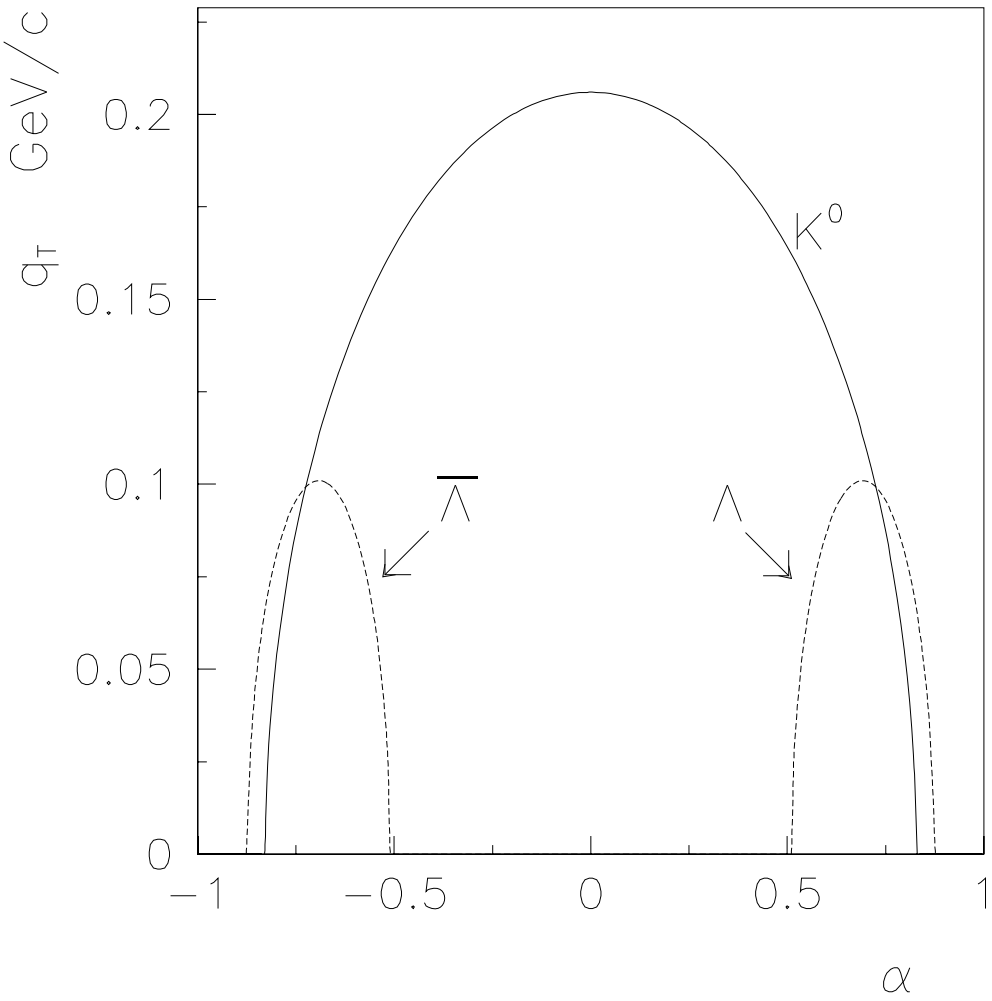

Figure C.2: Podolanski-Armenteros regions for different V^0 candidates.

Decay	ζ	p^* (GeV/c)	$\alpha_{\min}$	$\alpha_{\max}$	φ
$K^0_S \to \pi^+\pi^-$	0.8282	0.206	-0.828	+0.8282	0.
$\Lambda \to p\pi^-$	0.179	0.101	+0.515	0.873	0.694
$\overline{\Lambda} \to \overline{p}\pi^+$	0.179	0.101	-0.873	-0.515	-0.694

Table C.1: Podolanski Armenteros quantities.

Appendix D

MWPC efficiencies for the 1990 proton run

Chamber efficiencies are presented for data sampled over the entire 1990 p-W run.

Table D.1: Mean efficiencies (%) for chamber A1.

Y Plane	Quad 1	93.2 ± 0.7
	Quad 2	93.2 ± 0.9
	Quad 3	93.2 ± 0.7
	Quad 4	93.0 ± 0.9
U Plane	Quad 1	94.0 ± 0.7
	Quad 2	92.5 ± 0.9
	Quad 3	93.0 ± 0.7
	Quad 4	92.1 ± 0.9
V Plane	Quad 1	94.2 ± 0.7
	Quad 2	93.4 ± 0.9
	Quad 3	93.6 ± 0.7
	Quad 4	92.8 ± 0.9

Table D.2: Mean efficiencies (%) for chamber A2.

Y Plane	Quad 1	96.7 ± 0.7
	Quad 2	96.7 ± 0.9
	Quad 3	96.7 ± 0.7
	Quad 4	96.5 ± 0.9
U Plane	Quad 1	95.7 ± 0.7
	Quad 2	95.8 ± 0.9
	Quad 3	95.0 ± 0.7
	Quad 4	95.1 ± 0.9
V Plane	Quad 1	94.5 ± 0.7
	Quad 2	94.2 ± 0.9
	Quad 3	94.6 ± 0.7
	Quad 4	93.9 ± 0.9

Table D.3: Mean efficiencies (%) for chamber A3.

Y Plane	Quad 1	97.1 ± 0.7
	Quad 2	97.0 ± 0.9
	Quad 3	96.1 ± 0.7
	Quad 4	95.9 ± 0.9
U Plane	Quad 1	96.8 ± 0.7
	Quad 2	97.0 ± 0.9
	Quad 3	96.8 ± 0.7
	Quad 4	96.1 ± 0.9
V Plane	Quad 1	95.9 ± 0.7
	Quad 2	94.9 ± 0.9
	Quad 3	96.1 ± 0.7
	Quad 4	95.4 ± 0.9

Table D.4: Mean efficiencies (%) for chamber A4.

Y Plane	Quad 1	96.1 ± 0.7
	Quad 2	95.9 ± 0.9
	Quad 3	96.4 ± 0.7
	Quad 4	96.0 ± 0.9
U Plane	Quad 1	97.3 ± 0.7
	Quad 2	97.1 ± 0.9
	Quad 3	97.1 ± 0.7
	Quad 4	96.7 ± 0.9
V Plane	Quad 1	95.5 ± 0.7
	Quad 2	95.5 ± 0.9
	Quad 3	94.8 ± 0.7
	Quad 4	94.8 ± 0.9

Table D.5: Mean efficiencies (%) for chamber A5.

Y Plane	Quad 1	96.5 ± 0.7
	Quad 2	96.7 ± 0.9
	Quad 3	96.7 ± 0.7
	Quad 4	97.0 ± 0.9
U Plane	Quad 1	95.2 ± 0.7
	Quad 2	95.6 ± 0.9
	Quad 3	93.5 ± 0.7
	Quad 4	94.4 ± 0.9
V Plane	Quad 1	97.7 ± 0.7
	Quad 2	97.6 ± 0.9
	Quad 3	95.4 ± 0.7
	Quad 4	95.3 ± 0.9

Table D.6: Mean efficiencies (%) for chamber A6.

Y Plane	Quad 1	95.1 ± 0.7
	Quad 2	96.2 ± 0.9
	Quad 3	93.7 ± 0.7
	Quad 4	92.6 ± 0.9
U Plane	Quad 1	93.8 ± 0.7
	Quad 2	91.8 ± 0.9
	Quad 3	96.0 ± 0.7
	Quad 4	95.5 ± 0.9
V Plane	Quad 1	94.4 ± 0.7
	Quad 2	94.3 ± 0.9
	Quad 3	93.8 ± 0.7
	Quad 4	93.9 ± 0.9

Table D.7: Mean efficiencies (%) for chamber A7.

Y Plane	Quad 1	94.8 ± 0.7
	Quad 2	94.9 ± 0.9
	Quad 3	94.3 ± 0.7
	Quad 4	94.4 ± 0.9
U Plane	Quad 1	91.7 ± 0.7
	Quad 2	91.5 ± 0.9
	Quad 3	92.2 ± 0.7
	Quad 4	84.9 ± 0.9
V Plane	Quad 1	89.3 ± 0.6
	Quad 2	81.4 ± 0.8
	Quad 3	88.3 ± 0.7
	Quad 4	88.3 ± 0.9

Appendix E

Hodoscope efficiencies for the 1990 proton run

Hodoscope efficiencies are presented for data sampled over the entire 1990 p-W run.

Table E.1: Hodoscope efficiencies using the 1 cm edge cut.

HZ0	RIGHT	Slab 11	89.3 ± 9.4
		Slab 12	88.7 ± 1.2
		Slab 13	89.6 ± 1.1
		Slab 14	76.7 ± 1.1
		Slab 15	93.1 ± 1.0
HZ0	LEFT	Slab 11	81.9 ± 7.6
		Slab 12	88.3 ± 1.1
		Slab 13	89.7 ± 1.0
		Slab 14	81.5 ± 1.0
		Slab 15	80.6 ± 1.0
HZ1	RIGHT	Slab 11	82.5 ± 4.2
		Slab 12	94.5 ± 1.1
		Slab 13	95.1 ± 1.1
		Slab 14	90.8 ± 1.0
		Slab 15	92.6 ± 1.0
	LEFT	Slab 11	88.6 ± 3.4
		Slab 12	89.2 ± 1.0
		Slab 13	95.7 ± 1.0
		Slab 14	96.9 ± 1.0
		Slab 15	96.7 ± 0.9

Appendix F

Acceptance Tables

The acceptances for Λs, Ξ^-s, K^0s and π^-s for the configuration of the 1990 proton-tungsten trigger and appuratus are given in the following tables as a function of rapidity and transverse momentum. The acceptance for the corresponding anti-particles is the same to within 1% of the calculated values due to the symmetry of the magnetic field and apparatus.

Table F.1: Acceptances for Λs produced in WA85 1990 p-W interactions (in percent) - Part I.

y_{lab}	2.225	2.275	2.325	2.375	2.425	2.475	2.525	2.575	2.625	2.675
$p_T = 0.85$GeV/c	0.033	0.047	0.059	0.068	0.084	0.089	0.087	0.078	0.060	0.019
$p_T = 0.95$GeV/c	0.028	0.053	0.080	0.096	0.110	0.127	0.134	0.133	0.122	0.100
$p_T = 1.05$GeV/c	0.028	0.043	0.082	0.121	0.147	0.163	0.177	0.186	0.181	0.168
$p_T = 1.15$GeV/c	0.024	0.044	0.070	0.126	0.176	0.197	0.217	0.231	0.235	0.225
$p_T = 1.25$GeV/c	0.023	0.040	0.067	0.109	0.182	0.239	0.254	0.268	0.276	0.280
$p_T = 1.35$GeV/c	0.023	0.038	0.065	0.104	0.171	0.250	0.289	0.310	0.320	0.323
$p_T = 1.45$GeV/c	0.020	0.037	0.062	0.107	0.156	0.263	0.322	0.345	0.362	0.361
$p_T = 1.55$GeV/c	0.017	0.034	0.060	0.099	0.158	0.243	0.338	0.374	0.398	0.404
$p_T = 1.65$GeV/c	0.017	0.033	0.056	0.093	0.155	0.238	0.369	0.408	0.437	0.444
$p_T = 1.75$GeV/c	0.013	0.030	0.052	0.089	0.148	0.237	0.363	0.432	0.460	0.473
$p_T = 1.85$GeV/c	0.010	0.026	0.052	0.088	0.139	0.229	0.340	0.457	0.482	0.507
$p_T = 1.95$GeV/c	0.008	0.023	0.048	0.079	0.131	0.219	0.324	0.467	0.509	0.523
$p_T = 2.05$GeV/c	0.007	0.022	0.045	0.077	0.128	0.209	0.323	0.480	0.534	0.538
$p_T = 2.15$GeV/c	0.004	0.019	0.042	0.074	0.127	0.206	0.314	0.463	0.548	0.560
$p_T = 2.25$GeV/c	0.004	0.016	0.039	0.074	0.125	0.201	0.310	0.438	0.556	0.579
$p_T = 2.35$GeV/c	0.003	0.013	0.037	0.072	0.123	0.196	0.304	0.423	0.566	0.600
$p_T = 2.45$GeV/c	0.002	0.013	0.037	0.073	0.122	0.192	0.287	0.424	0.576	0.599
$p_T = 2.55$GeV/c	0.002	0.010	0.037	0.070	0.120	0.187	0.284	0.410	0.581	0.612
$p_T = 2.65$GeV/c	0.002	0.009	0.034	0.069	0.116	0.187	0.277	0.402	0.582	0.627
$p_T = 2.75$GeV/c	0.001	0.008	0.034	0.068	0.119	0.189	0.267	0.390	0.555	0.638
$p_T = 2.85$GeV/c	0.001	0.007	0.031	0.068	0.121	0.185	0.265	0.382	0.551	0.639
$p_T = 2.95$GeV/c	0.001	0.007	0.030	0.065	0.117	0.180	0.259	0.378	0.537	0.638

Table F.2: Acceptances for Λs produced in WA85 1990 p-W interactions (in percent) - Part II.

Y_{lab}	2.725	2.775	2.825	2.875	2.925	2.975
$p_T = 0.85$GeV/c	0.000	0.000	0.000	0.000	0.000	0.000
$p_T = 0.95$GeV/c	0.058	0.001	0.001	0.000	0.000	0.000
$p_T = 1.05$GeV/c	0.141	0.084	0.003	0.000	0.000	0.000
$p_T = 1.15$GeV/c	0.208	0.168	0.094	0.002	0.000	0.000
$p_T = 1.25$GeV/c	0.268	0.237	0.181	0.081	0.000	0.000
$p_T = 1.35$GeV/c	0.318	0.285	0.246	0.171	0.034	0.000
$p_T = 1.45$GeV/c	0.364	0.339	0.300	0.232	0.132	0.002
$p_T = 1.55$GeV/c	0.404	0.383	0.351	0.291	0.199	0.045
$p_T = 1.65$GeV/c	0.439	0.422	0.384	0.334	0.257	0.127
$p_T = 1.75$GeV/c	0.476	0.456	0.425	0.373	0.298	0.188
$p_T = 1.85$GeV/c	0.510	0.492	0.456	0.409	0.335	0.228
$p_T = 1.95$GeV/c	0.529	0.526	0.492	0.446	0.374	0.274
$p_T = 2.05$GeV/c	0.556	0.534	0.512	0.472	0.397	0.303
$p_T = 2.15$GeV/c	0.576	0.556	0.540	0.484	0.419	0.336
$p_T = 2.25$GeV/c	0.593	0.577	0.549	0.508	0.444	0.354
$p_T = 2.35$GeV/c	0.606	0.589	0.565	0.513	0.459	0.380
$p_T = 2.45$GeV/c	0.621	0.605	0.578	0.534	0.470	0.390
$p_T = 2.55$GeV/c	0.623	0.618	0.581	0.539	0.488	0.398
$p_T = 2.65$GeV/c	0.637	0.629	0.594	0.551	0.490	0.412
$p_T = 2.75$GeV/c	0.647	0.637	0.604	0.556	0.499	0.416
$p_T = 2.85$GeV/c	0.651	0.647	0.603	0.561	0.499	0.428
$p_T = 2.95$GeV/c	0.644	0.636	0.606	0.566	0.507	0.431

Table F.3: Acceptances for Ξ^-s produced in WA85 1990 p-W interactions (in percent) - Part I.

Y_{lab}	2.225	2.275	2.325	2.375	2.425	2.475	2.525	2.575	2.625	2.675
$p_T = 1.25$GeV/c	0.020	0.040	0.058	0.071	0.078	0.082	0.086	0.083	0.071	0.057
$p_T = 1.35$GeV/c	0.030	0.047	0.069	0.094	0.112	0.122	0.125	0.126	0.114	0.099
$p_T = 1.45$GeV/c	0.039	0.054	0.080	0.108	0.141	0.156	0.168	0.172	0.168	0.155
$p_T = 1.55$GeV/c	0.043	0.061	0.084	0.121	0.163	0.201	0.213	0.218	0.218	0.213
$p_T = 1.65$GeV/c	0.049	0.069	0.096	0.129	0.180	0.237	0.260	0.269	0.269	0.266
$p_T = 1.75$GeV/c	0.054	0.072	0.102	0.141	0.196	0.257	0.303	0.325	0.321	0.318
$p_T = 1.85$GeV/c	0.056	0.081	0.107	0.144	0.198	0.280	0.355	0.373	0.381	0.373
$p_T = 1.95$GeV/c	0.060	0.087	0.114	0.151	0.208	0.296	0.387	0.421	0.432	0.422
$p_T = 2.05$GeV/c	0.062	0.091	0.122	0.156	0.222	0.296	0.404	0.458	0.479	0.465
$p_T = 2.15$GeV/c	0.064	0.090	0.128	0.168	0.222	0.304	0.419	0.511	0.520	0.515
$p_T = 2.25$GeV/c	0.065	0.094	0.133	0.173	0.229	0.314	0.432	0.531	0.559	0.562
$p_T = 2.35$GeV/c	0.066	0.097	0.135	0.177	0.236	0.321	0.434	0.556	0.610	0.590
$p_T = 2.45$GeV/c	0.067	0.098	0.134	0.180	0.239	0.316	0.437	0.579	0.639	0.632
$p_T = 2.55$GeV/c	0.067	0.096	0.137	0.182	0.242	0.323	0.445	0.589	0.669	0.645
$p_T = 2.65$GeV/c	0.065	0.099	0.135	0.181	0.245	0.323	0.443	0.590	0.686	0.686
$p_T = 2.75$GeV/c	0.062	0.097	0.135	0.183	0.242	0.326	0.428	0.587	0.709	0.705
$p_T = 2.85$GeV/c	0.061	0.096	0.134	0.178	0.238	0.325	0.433	0.590	0.711	0.725
$p_T = 2.95$GeV/c	0.063	0.093	0.130	0.179	0.240	0.313	0.432	0.584	0.719	0.739

Table F.4: Acceptances for Ξ^-s produced in WA85 1990 p-W interactions (in percent) - Part II.

Y_{lab}	2.725	2.775	2.825	2.875	2.925	2.975
$p_T = 1.25$GeV/c	0.038	0.014	0.000	0.000	0.000	0.000
$p_T = 1.35$GeV/c	0.081	0.049	0.014	0.000	0.000	0.000
$p_T = 1.45$GeV/c	0.125	0.095	0.049	0.008	0.000	0.000
$p_T = 1.55$GeV/c	0.184	0.146	0.099	0.037	0.000	0.000
$p_T = 1.65$GeV/c	0.244	0.204	0.150	0.084	0.016	0.000
$p_T = 1.75$GeV/c	0.299	0.263	0.202	0.128	0.051	0.000
$p_T = 1.85$GeV/c	0.355	0.314	0.262	0.180	0.096	0.013
$p_T = 1.95$GeV/c	0.403	0.379	0.313	0.237	0.141	0.039
$p_T = 2.05$GeV/c	0.454	0.423	0.364	0.290	0.187	0.080
$p_T = 2.15$GeV/c	0.501	0.467	0.413	0.330	0.228	0.112
$p_T = 2.25$GeV/c	0.542	0.517	0.459	0.369	0.264	0.147
$p_T = 2.35$GeV/c	0.564	0.542	0.488	0.407	0.303	0.181
$p_T = 2.45$GeV/c	0.609	0.576	0.532	0.440	0.328	0.210
$p_T = 2.55$GeV/c	0.626	0.590	0.551	0.466	0.359	0.235
$p_T = 2.65$GeV/c	0.654	0.612	0.574	0.487	0.382	0.265
$p_T = 2.75$GeV/c	0.672	0.633	0.584	0.506	0.405	0.279
$p_T = 2.85$GeV/c	0.689	0.648	0.589	0.521	0.420	0.292
$p_T = 2.95$GeV/c	0.710	0.660	0.610	0.527	0.432	0.313

Table F.5: Acceptances for K^0s produced in WA85 1990 p-W interactions (in percent) - Part I.

Y_{lab}	2.225	2.275	2.325	2.375	2.425	2.475	2.525	2.575	2.625	2.675
$p_T = 0.95$GeV/c	0.000	0.000	0.000	0.000	0.000	0.000	0.016	0.035	0.055	0.086
$p_T = 1.05$GeV/c	0.000	0.000	0.000	0.000	0.004	0.010	0.023	0.050	0.083	0.122
$p_T = 1.15$GeV/c	0.000	0.000	0.000	0.003	0.007	0.015	0.030	0.065	0.116	0.176
$p_T = 1.25$GeV/c	0.000	0.000	0.001	0.004	0.009	0.019	0.042	0.088	0.154	0.223
$p_T = 1.35$GeV/c	0.000	0.000	0.001	0.005	0.012	0.028	0.051	0.108	0.200	0.290
$p_T = 1.45$GeV/c	0.000	0.000	0.002	0.007	0.016	0.034	0.069	0.130	0.243	0.351
$p_T = 1.55$GeV/c	0.000	0.000	0.002	0.008	0.021	0.044	0.088	0.160	0.294	0.418
$p_T = 1.65$GeV/c	0.000	0.000	0.003	0.009	0.028	0.055	0.104	0.193	0.340	0.485
$p_T = 1.75$GeV/c	0.000	0.000	0.003	0.012	0.035	0.072	0.125	0.224	0.383	0.549
$p_T = 1.85$GeV/c	0.000	0.000	0.004	0.016	0.041	0.081	0.148	0.252	0.429	0.605
$p_T = 1.95$GeV/c	0.000	0.001	0.006	0.019	0.049	0.099	0.171	0.280	0.473	0.645
$p_T = 2.05$GeV/c	0.000	0.001	0.008	0.025	0.058	0.116	0.193	0.308	0.504	0.698
$p_T = 2.15$GeV/c	0.000	0.001	0.009	0.030	0.069	0.130	0.210	0.332	0.534	0.740
$p_T = 2.25$GeV/c	0.000	0.001	0.012	0.036	0.078	0.149	0.234	0.358	0.578	0.780
$p_T = 2.35$GeV/c	0.000	0.002	0.013	0.044	0.089	0.157	0.256	0.384	0.608	0.816
$p_T = 2.45$GeV/c	0.000	0.002	0.017	0.049	0.100	0.175	0.271	0.405	0.635	0.831
$p_T = 2.55$GeV/c	0.000	0.002	0.019	0.056	0.111	0.189	0.292	0.436	0.654	0.866
$p_T = 2.65$GeV/c	0.000	0.002	0.020	0.060	0.124	0.208	0.316	0.443	0.670	0.900
$p_T = 2.75$GeV/c	0.000	0.003	0.024	0.068	0.135	0.217	0.325	0.459	0.691	0.925
$p_T = 2.85$GeV/c	0.000	0.003	0.024	0.075	0.145	0.228	0.342	0.475	0.717	0.940
$p_T = 2.95$GeV/c	0.000	0.003	0.028	0.081	0.154	0.243	0.349	0.488	0.736	0.955

Table F.6: Acceptances for K^0s produced in WA85 1990 p-W interactions (in percent) - Part II.

Y_{lab}	2.725	2.775	2.825	2.875	2.925	2.975
$p_T = 0.95$GeV/c	0.115	0.131	0.123	0.096	0.067	0.037
$p_T = 1.05$GeV/c	0.162	0.188	0.185	0.154	0.115	0.068
$p_T = 1.15$GeV/c	0.223	0.253	0.252	0.224	0.170	0.108
$p_T = 1.25$GeV/c	0.282	0.326	0.324	0.294	0.236	0.163
$p_T = 1.35$GeV/c	0.352	0.389	0.397	0.365	0.301	0.217
$p_T = 1.45$GeV/c	0.425	0.457	0.459	0.434	0.366	0.273
$p_T = 1.55$GeV/c	0.487	0.520	0.531	0.490	0.431	0.345
$p_T = 1.65$GeV/c	0.553	0.593	0.580	0.559	0.493	0.399
$p_T = 1.75$GeV/c	0.613	0.648	0.638	0.616	0.552	0.457
$p_T = 1.85$GeV/c	0.665	0.695	0.684	0.662	0.595	0.496
$p_T = 1.95$GeV/c	0.719	0.751	0.743	0.692	0.636	0.550
$p_T = 2.05$GeV/c	0.770	0.799	0.782	0.740	0.686	0.594
$p_T = 2.15$GeV/c	0.811	0.828	0.814	0.781	0.718	0.623
$p_T = 2.25$GeV/c	0.849	0.859	0.857	0.810	0.743	0.645
$p_T = 2.35$GeV/c	0.887	0.892	0.891	0.832	0.763	0.683
$p_T = 2.45$GeV/c	0.909	0.926	0.912	0.873	0.789	0.699
$p_T = 2.55$GeV/c	0.936	0.950	0.939	0.880	0.813	0.719
$p_T = 2.65$GeV/c	0.965	0.987	0.963	0.898	0.824	0.723
$p_T = 2.75$GeV/c	0.995	1.009	0.982	0.926	0.854	0.747
$p_T = 2.85$GeV/c	1.004	1.017	1.002	0.933	0.862	0.758
$p_T = 2.95$GeV/c	1.021	1.041	1.015	0.940	0.883	0.775

Table F.7: Acceptances for π^-s produced in WA85 1990 p-W interactions (in percent) - Part I.

Y_{lab}	2.225	2.275	2.325	2.375	2.425	2.475	2.525	2.575	2.625	2.675
$p_T = 0.65$GeV/c	0.137	0.879	1.077	1.629	2.527	3.137	4.347	5.145	6.774	8.502
$p_T = 0.75$GeV/c	2.929	3.594	3.943	4.238	4.635	4.991	5.630	6.323	7.083	8.556
$p_T = 0.85$GeV/c	3.467	3.613	3.996	4.298	4.633	5.026	5.570	6.200	7.148	8.473
$p_T = 0.95$GeV/c	3.481	3.621	3.967	4.293	4.722	5.016	5.668	6.256	7.147	9.767
$p_T = 1.05$GeV/c	3.485	3.628	4.062	4.292	4.736	5.099	5.647	6.250	7.160	10.132
$p_T = 1.15$GeV/c	2.522	2.976	3.619	4.210	4.620	5.076	5.548	6.245	7.621	10.679
$p_T = 1.25$GeV/c	0.678	1.209	1.757	2.335	3.028	3.875	4.769	5.833	7.960	10.892
$p_T = 1.35$GeV/c	0.000	0.003	0.451	1.104	1.791	2.591	3.415	4.520	7.000	10.654
$p_T = 1.45$GeV/c	0.339	0.282	0.246	0.386	0.989	1.529	2.389	3.666	6.233	9.891
$p_T = 1.55$GeV/c	1.380	1.366	1.465	1.471	1.478	1.974	2.531	3.514	5.670	9.170
$p_T = 1.65$GeV/c	1.903	2.256	2.220	2.277	2.357	2.489	2.933	4.223	6.355	9.266
$p_T = 1.75$GeV/c	1.731	2.243	2.835	2.907	2.901	2.943	3.256	4.806	6.772	9.786
$p_T = 1.85$GeV/c	1.587	2.055	2.640	3.260	3.477	3.435	3.471	5.085	7.164	10.218
$p_T = 1.95$GeV/c	1.447	1.946	2.543	3.110	3.810	3.896	4.055	5.353	7.588	10.581
$p_T = 2.05$GeV/c	1.341	1.747	2.329	3.018	3.713	4.351	4.565	5.622	7.718	10.830
$p_T = 2.15$GeV/c	1.243	1.712	2.163	2.910	3.506	4.379	5.080	6.022	7.931	11.058
$p_T = 2.25$GeV/c	1.135	1.582	2.104	2.655	3.516	4.300	5.517	6.437	8.083	11.229
$p_T = 2.35$GeV/c	1.068	1.527	2.048	2.712	3.298	4.133	5.655	6.869	8.356	11.441
$p_T = 2.45$GeV/c	0.991	1.464	1.979	2.536	3.209	4.024	5.672	7.200	8.314	11.476
$p_T = 2.55$GeV/c	0.896	1.341	1.892	2.492	3.197	3.997	5.577	7.504	8.725	11.694
$p_T = 2.65$GeV/c	0.834	1.313	1.760	2.389	3.095	3.937	5.650	7.694	9.024	11.783
$p_T = 2.75$GeV/c	0.791	1.240	1.772	2.365	3.059	3.842	5.676	7.663	9.197	11.968
$p_T = 2.85$GeV/c	0.703	1.230	1.690	2.311	2.936	3.892	5.636	7.618	9.478	12.180
$p_T = 2.95$GeV/c	0.647	1.177	1.631	2.238	2.850	3.884	5.656	7.654	9.695	12.227

Table F.8: Acceptances for π^-s produced in WA85 1990 p-W interactions (in percent) - Part II.

Y_{lab}	2.725	2.775	2.825	2.875	2.925	2.975
$p_T = 0.65$GeV/c	10.608	11.072	8.788	9.415	6.985	7.355
$p_T = 0.75$GeV/c	13.566	13.141	11.901	12.239	10.401	10.588
$p_T = 0.85$GeV/c	15.204	13.397	13.903	13.294	12.584	12.542
$p_T = 0.95$GeV/c	16.094	15.200	15.130	13.667	14.342	13.020
$p_T = 1.05$GeV/c	15.938	16.159	15.529	15.166	15.095	13.644
$p_T = 1.15$GeV/c	17.155	16.708	15.872	15.878	15.561	14.566
$p_T = 1.25$GeV/c	17.366	17.057	16.610	16.095	16.015	14.729
$p_T = 1.35$GeV/c	17.570	17.144	16.871	16.457	16.286	15.144
$p_T = 1.45$GeV/c	16.692	16.905	17.009	16.590	16.679	15.490
$p_T = 1.55$GeV/c	16.126	16.156	16.578	16.761	16.737	15.717
$p_T = 1.65$GeV/c	15.697	15.835	15.949	16.281	16.631	15.901
$p_T = 1.75$GeV/c	16.157	15.767	15.618	15.875	16.426	15.880
$p_T = 1.85$GeV/c	16.565	16.270	15.897	15.505	15.965	15.764
$p_T = 1.95$GeV/c	16.959	16.605	16.116	15.690	15.718	15.283
$p_T = 2.05$GeV/c	17.309	16.917	16.483	16.089	15.761	15.116
$p_T = 2.15$GeV/c	17.546	17.166	16.760	16.216	16.066	14.984
$p_T = 2.25$GeV/c	17.654	17.443	16.909	16.489	16.146	15.039
$p_T = 2.35$GeV/c	17.857	17.639	16.955	16.663	16.473	15.335
$p_T = 2.45$GeV/c	17.955	17.652	17.408	16.824	16.636	15.437
$p_T = 2.55$GeV/c	18.243	18.021	17.542	16.793	16.635	15.576
$p_T = 2.65$GeV/c	18.428	18.121	17.529	17.143	16.972	15.692
$p_T = 2.75$GeV/c	18.375	18.230	17.741	17.257	17.022	15.725
$p_T = 2.85$GeV/c	18.646	18.310	17.986	17.428	17.086	15.763
$p_T = 2.95$GeV/c	18.627	18.340	17.984	17.309	17.239	15.786

Bibliography

[1] B. Müller, "*The Physics of the Quark-Gluon-Plasma*", Springer-Verlag, 1985.

[2] J. Rafelski, 21st Rencontres de Moriond, Les Arcs, 1983.

[3] J. Rafelski and B. Müller, Phys. Rev. Lett. **48** (1982) 1066; **56** (1986) 2324.

[4] P. Koch, B. Müller and J. Rafelski, Physics Reports **142** (1986) 167.

[5] J. Cleymans *et al.*, Phys. Rep. 130 (1986) 217.

[6] EPS-0363 (D0 Coll.), HEP Brussels Conference '95.
EPS-511 and EPS-0063 (CDF Coll.), HEP Brussels Conference '95.

[7] D.H.Perkins, Introduction to High Energy Physics, Addison-Wesley Publishing Company, Third Edition (1987) 106-110.

[8] F.E.Close, "*Introduction to Quarks and Partons*", Subsidiary of Harcourt Brace Jovanovich Publishers (1979) p9.

[9] F.Halzen and A.D.Martin, "*Quarks and Leptons: An Introductory Course in Modern Particle Physics*", John Wiley and Sons (1984).

[10] T. Matsui, H. Satz, Phys. Lett. **178B** (1986) 416.

[11] F. Karsch *et al.*, Z. Phys. **C37** (1988) 617-622.

[12] K. Kanaya and H. Satz, "*Correlation and screening in finite temperatures SU(2) gauge theory*", Bielefeld preprint BI-IP 86/16 May (1986).

[13] A. Chodos, R. L. Jaffe, K. Johnson, C. B. Thorn, and V. F. Weisskopf, Phys. Rev. **D9** (1974) 4371.

[14] K. Johnson, Acta Phys. Pol. **B6** (1975) 865.

[15] P. Hasenfratz and J. Kuti, Phys. Rep. 40 (1978) 75.

[16] J. Cleymans *et al.*, Phys. Rep. 130 (1986) 217.

[17] R. Hagedorn, Suppl. Nuovo Cimento 3 (1965) 147.
R. Hagedorn and U. Wambach, Nucl. Phys. **B123** (1977) 382.

[18] S. Gottlieb *et al.*, Phys. Rev. **D35** (1987) 3972.

[19] L. Van Hove, "*Quark Gluon Plasma and Multiparticle Production*", CERN-TH.5236/88.

[20] B. Petersson, "*Lattice QCD Predictions for very hot Nuclear Matter*", Fakultät für Physik, Universität Bielefeld.

[21] C. W. Fabjan, 23^{rd} Rencontres de Moriond, Les Arcs, 13-19 March (1988)

[22] J. Barrette, *et al.*, Phys. Rev. **C45** (1992) 819.

[23] H. Hamagaki (E866 Coll.), Nucl. Phys. **A566** (1994) 27c-34c.

[24] R. Stock, Nucl. Phys. **A525** (1991) 221c.

[25] M. Jacob, "*In Search of Quark Matter*", CERN-TH. 7343/94.

[26] T. C. Awes, (WA80 Coll.), Nucl. Phys. **A590** (1995) 81c-92c.

[27] P. Wurm, Nucl. Phys. **A590** (1995) 103c-116c.

[28] S. Ramos, (NA38 Coll.), Nucl. Phys. **A590** (1995) 117c-126c.

[29] M. Masera, (HELIOS Coll.), Nucl. Phys. **A590** (1995) 93c-102c.

[30] F. Karsch and R. Petronzio, Phys. Lett. **B193** (1987) 105.

[31] H. Satz, Phys. Lett. **B242** (1990) 107 and preprint CERN TII.5900/90 (1990).

[32] S. Gupta and H. Satz, Phys. lett. **B283** (1992) 439.

[33] J. Letessier, A. Tounsi, U. Heinz, J. Sollfrank, J. Rafelski, Phys. Rev. Lett. 70 (1993) 3530.

[34] U. Heinz, Nuclear Physics **A566** (1994), 205c.

[35] B. S. Kumar, Nucl. Phys. **A590** (1995) 29c-46c.

[36] C. Greiner, P. Koch and H. Stöcker, Phys. Rev. Lett. **58** (1987) 1825.

[37] F. S. Rotondo, AIP Conference Proc. 340 (1995) 16-23.

[38] T. S. Biro, E. Van Doorn, B. Muller, M. H. Thoma and X. N. Wang, DUKE-TH-93-46, Phys. Rev. C.

[39] J. Rafelski, Phys. Lett. **B262** (1991) 333.

[40] H. Satz, "*Deconfinement: Concept, Theory, Test*", Invited talk at the ERC Physics of High Energy heavy Ions, CERN-TH.7410/94 BI-TP 94/45 (1994) 1-13.

[41] H. C. Eggers and J. Rafelski, Int. J. of Mod. Phys. A, Vol. 6, No. 7 (1991) 1067.

[42] H. C. Eggers and J. Rafelski, 23^{rd} Rencontres de Moriond, March (1989).

[43] J. Bartke *et al.*, (NA35 Coll.), Z. f. Phys. **C48** (1990) 191.
J. Bartke *et al.*, (NA35 Coll.), Nucl. Phys. **A525** 221c.

[44] A. Bamberger *et al.*, (NA35 Coll.), Z. f. Phys. **C43** (1989) 25.

[45] I. Derado *et al.*, (NA5 Coll.), Z. f. Phys. **C50** (1991) 31.

[46] D. H. Brick *et al.*, (E565/570 Coll.), Phys. Rev. **D45** (1992) 734.

[47] D. N. Schramm, 'Proc. 2^{nd} Int. Conf. on Physics and Astrophysics of the Quark Gluon Plasma', Calcutta, India (1993). World Scientific (editor - B. Sinha) (1994) 170-182.

[48] R. Scherrer, J. Applegate and C. Hogan, Phys. Rev. **D35** (1987) 1151.

[49] WA85 Proposal, CERN/SPSC/84-76 P206 (1984) CERN/SPSC/87-18 P206 Add. (1987), CERN/SPSC/88-20 P206 Add. (1988).

[50] WA94 Proposal, CERN/SPSLC/91-5 (1991).

[51] WA97 Proposal, CERN/SPSLC/91-29 (1991).

[52] J. Rafelski and M. Danos, Phys. Lett. **B192** (1987) 432.

[53] W. Beusch, Omega Prime, CERN/SPSC/84-62/P204 (1984)

[54] W. Beusch *et al.*, Nucl. Inst. Meth. **A249** (1986) 391.

[55] K. Knudson and O. Villalobos Baillie, Internal Report, '*On Enhancing Strangeness in the 1989 WA85 Proton Run*', (1993).
S. Abatzis *et al.*, (WA85 Coll.), 'Proc. Int. Symp. on Strangeness and Quark Matter', Crete (September 1994).

[56] H. Grote and I. McLaren, DD/EE/81-2 (EPIO manual).

[57] J-C Lassalle *et al.*DD/EE/79-2 (TRIDENT Manual).

[58] Particle Data Group, Phys. Rev. **D50** (1994) 1172-1825.

[59] J. Podolanski and R. Armenteros, Phil. Mag 45 (1954) 13.

[60] Thesis of R. P. Barnes, "*Production of Strange and Multistrange Baryons in Ultrarelativistic Heavy Ion Collisions*", The University of Birmingham (1994).

[61] Thesis of D. Evans, "*Strange and Multistrange Baryon and Antibaryon production in Sulphur-Tungsten Interactions at 200 GeV/c Per Nucleon*", The University of Birmingham (1992).

[62] J. Schukraft, CERN-PPE/91-04 (1991).

[63] B. V. Jacak, Nucl. Phys. **A525** (1991) 77c-90c.
B. V. Jacak, in: "*Particle Production in Highly Excited Matter*", NATO-ASI Series B, Vol. 303. Ed. H.H. Gutbrod and J. Rafelski, Plenum Press, New York (1993) 471-498.

[64] B. Andersson, G. Gustafson, C. Peterson, Phys. Lett. **B69** (1977) 221 and **B71** (1977) 337.

[65] J. Cugnon, Phys. Rev. **C23**, 2094 (1981).

[66] E. Schnedermann, J. Sollfrank and U. Heinz; "*Fireball Spectra*" in "*Particle Production in Highly Excited Matter*", NATO-ASI Series B, Vol. 303. Ed. H.H. Gutbrod and J. Rafelski, Plenum Press, New York (1993) p. 175-206.

[67] K.S.Lee, U.Heinz, and E. Schnedermann, Z. Phys. C48 (1990) 525.
E. Schnedermann and U. Heinz, Phys. Rev. Lett. 69 (1992) 2908.

[68] E. Andersen *et al.*, Nucl. Phys. **A566** (1994) 217c-224c.

[69] F. James and M. Roos, MINUIT manual, CERN Program Library D506.

[70] R. Lietava, Internal Report, "*Strange Baryon Production in S-S Interactions at 200 GeV/c per Nucleon*", (1994).

[71] The WA85 Coll., S. Abatzis *et al.*, Phys. Lett. **B395** (1995) 382-386.

[72] J. Letessier *et al.*, "*Strangeness conservation in hot fireballs*", PAR/LPTHE/92-27.

[73] The WA94 Coll., J.B. Kinson *et al*, **A590** (1995) 317c.
The WA94 Coll., S. Abatzis *et al*, Phys. Lett. **B354** (1995) 178-182.

[74] AFS Coll., T. Åkesson *et al.*, Nucl. Phys. **B246** (1984) 1-11.

[75] H. Sorge *et al.*, in: "*Particle Production in Highly Excited Matter*", NATO-ASI Series B, Vol. 303. ED. H.H. Gutbrod and J. Rafelski, Plenum Press, New York (1993) 335-376..

[76] N.S. Amelin *et al.*, Phys. Rev. **C47** (1993) 2299.

[77] K. Werner, Nucl. Phys. **A566** (1994) 477c.

[78] H. Sorge, SUNY-NTG-94-50, October 1994.

[79] T. Alber (NA35 Coll.) IKF-HENPG/1-94 (1994).

[80] J.W. Cronin *et al.*, Phys. Rev. **D11**, 3105 (1975).
D. Antreasyan *et al.*, Phys. Rev. **D19**, 764 (1979).

[81] G. Lovhoiden, H. Helstrup and E. Andersen, Internal Report,"*Distortion of m_T of Negatives due to Kaon Contamination*", CERN 6/7/94.

[82] E. Andersen *et al.*, **A566** (1994) 487c-490c.

[83] N. Antoniou *et al.*, Letter of Intent for A Large Ion Collider Experiment CERN/LHCC/93-16, LHCC/I4 (1993).
J. Schukraft, Nucl. Phys. **A566** (1994) 311c.

[84] T. Akesson *et al.*, Nucl. Phys. **B353** (1991) 1-19.

[85] F. Videbaek, 'Proc. Workshop on Heavy Ion Physics at the AGS (HIPAG)', Brookhaven, NY, USA (1990) [report BNL-44911].

[86] HELIOS Coll., "*Comprehensive results on nucleus-nucleus interactions at 200 Gev per nucleon*" in: 'Proc. Int. Europhysics Conf. on H.E.P', Madrid (1989). Ed. G. Barreiro, Nucl. Phys. B.

[87] J. T. Mitchell, (NA35 Coll.), Nucl. Phys. **A566** (1994) 415c-418c.

[88] R. Vogt, Nucl. Phys. **A553** (1993) 785c-790c.